Discovering SUSY with $\tau^+\tau^-$ over $t\bar{t}$ Background – Evaluation of ATLAS Potential with 2010 Data

Ørjan Dale

Department of Physics and Technology

University of Bergen

Master's Degree in Experimental Particle Physics

June 2011

Acknowledgements

First and foremost I would like to thank my two supervisors, Thomas Burgess and Anna Lipniacka, for their excellent mentorship throughout my work on this thesis.

Regarding specific contributions to the thesis I am very grateful to Alex Kastanas for help running on the grid, Peter Rosendahl for producing Ntuples along wiht Thomas Burgess and Therese Sjursen for finding mSUGRA points and providing code for the Fisher analysis. I also want to thank Trygve Buanes and Hanne for proofreading the thesis. I would like to thank everyone at the particle physics group in Bergen for making it a pleasant place to study.

I would especially like to thank Anders Haarr, Anders Kvellestad and Siri Fløgstad Svensson for making the last two years really enjoyable.

Finally I would like to thank family, friends and most of all Kathrine for all her support.

Ørjan Dale

June 2011

Contents

List of Figures

LIST OF FIGURES

LIST OF FIGURES

List of Tables

LIST OF TABLES

1

Introduction

The top quark is the heaviest quark in the Standard Model of particle physics (SM). It was discovered relatively recently, at the Tevatron in 1995 [1], and hence it is the least studied of all quarks. The Large Hadron Collider (LHC) is designed to collide protons at a centre of mass energy of up to 14 TeVand thus constitutes a top factory. Even in data recorded during the first year of running (2010) top events should be abundant. Events with tops will be characterised by high transverse momentum (p_{T}), jets with b-quarks (b-jets) and large missing transverse energy ($E_{\mathrm{T}}^{\mathrm{miss}}$), all of which are also important characteristics of beyond SM physics processes. Thus top quarks studies provide an important early measurement with implications for new physics beyond the SM.

One of the most studied extensions to the SM is SUper SYmmetry (SUSY). SUSY promises to solve many of the problems of the SM – among others the Hierarchy problem, moreover the Lightest SUSY Particle (LSP) can provide a Dark Matter candidate. In SUSY models where the mass difference between the Neutralino (LSP) and stau (next to LSP) is low, co-annihilations balance the production of Dark Matter in the early universe. These models often contain final states with taus, making SUSY searches in tau channels important for both discovery and determination of the properties of the SUSY model. Due to the large centre of mass energy in collisions at the LHC new, heavy particles may be produced, expanding the experimental reach to include SUSY particles heavier than previously available to physics experiments. If such a SUSY model is realised in nature we would expect to see events with large p_{T}, $E_{\mathrm{T}}^{\mathrm{miss}}$, b-jets and to two tau leptons in the ATLAS experiment. One of the largest background to

such a signal would be SM top-anti-top quark events, where tau leptons arise from W-bosons created in the top decays. This thesis will focus on $t\bar{t}$ events with taus, by itself and as a background to SUSY.

The first chapters introduces the theoretical arguments the Standard Model (Chapter 2) and Supersymmetry (Chapter 3) are built upon. Chapter 4 presents the ATLAS experiment, with an emphasis on the ATLAS detector. This is followed by an investigation of the tau lepton at the ATLAS experiment in Chapter 5, before $t\bar{t}$ events are dealt with and the top mass attempted reconstructed in Chapter 6. Chapter 7 regards $t\bar{t}$ as a background to be entangled from a SUSY signal. In Chapter 8 the results from Chapter 7 will be compared with data from the ATLAS experiment.

2

The Standard Model

The Standard Model (SM) [2, 3, 4] is a hugely successful theory that was developed in the 1960s to describe the smallest components of matter at small scales and high energies. It has been probed to a very high accuracy, and is still the main model of particle physics. However successful the theory has proved to be, it still leaves some important questions unanswered. Necessitating new models that go beyond the current explanations of the Standard Model. This chapter first deals with the basic constituents of particle physics, before briefly describing the theoretical arguments providing the fundament of the SM. This section follows closely the one in [5]. For details and a more rigorous theoretical treatment of the SM [5] and [6] should be consulted respectively.

2.1 The Building Blocks of Particle Physics

Nature is governed by four fundamental forces - strong, electromagnetic, weak and gravitational. Strong forces, as the name suggests, are the strongest of the four. This is the force responsible for binding quarks together in nucleons (e.g. protons and neutrons), as well as binding nucleons together to make nuclei. The second strongest force is the electromagnetic. This force provides the attraction or repulsion of charged particles, and constitutes the basics of chemistry and the physics of materials. This is the force, along with gravity, dominating our macroscopic everyday lives. Next in line is the weak force. This force is responsible for beta-decay, allowing protons to change into neutrons and vice versa (really a change of quark flavour by emitting a W boson). It also plays a crucial role in the formation of the heavy elements, both

in the Big Bang nucleosynthesis and in stellar cores. Fusion processes in general and the fusion power cycles in stars are also dependent on the weak force. The last, and by far the weakest, of the forces is the gravitational. Its effect is negligible for nuclear and sub-nuclear particles, but is of prime importance for large scales and bodies as is the case in classical physics. Consequently the gravitational force is not described by the SM. One of the remaining problems of particle physics is the incorporation of a quantum theory of gravity.

These forces are propagated by fields or particles, where the particles are quantum states of the fields. Electromagnetic interactions for example can be described in terms of photons which are considered as quantum states of the electromagnetic field. Despite the apparent differences between the four forces, there still remain an eye catching similarity - the gauge bosons. The strong force is mediated by massless spin-1 gluons, the weak force is transmitted by massive spin-1 W and Z bosons, which is analogous to the electromagnetic force carrier - the spin-1 photon. The main properties of these force carriers are summarised in 2.1

Force	**Boson Name**	**Symbol**	**Charge**	**Spin**	**Mass**
Strong	gluon	g	0	1	0
Electromagnetic	photon	γ	0	1	0
Weak	W-boson	$W^{\pm}$	± 1	1	80.4
	Z-boson	Z^0	0	1	91.2

Table 2.1: The fundamental forces and their force carrying gauge bosons - Electric charge is in units of e, and mass in units of GeV.

Not only does the strength of the forces vary drastically, their range also differs significantly. The forces with massless gauge bosons, except for the special case of the gluon, all have a potential energy falling as $\frac{1}{r}$. Weak interactions have a exponential damping factor due to the massive force carriers which yields a potential energy falling as $\frac{e^{-mr}}{r}$, where m is the mass of the W or Z. This means that the force cuts off sharply beyond $r = 2 \cdot 10^{-16}$ cm. The potential energy of the strong force deviates from the expected $\frac{1}{r}$ behaviour due to the effect of colour, which will be discussed in the following section.

In addition to the gauge bosons there exist fermions which constitutes the building blocks of matter. Fermions contain two sub-categories of particles - one of these are the

leptons. These particles are characterised by having spin-$\frac{1}{2}$, no strong interactions and an associated neutrino. Of these particles the electrons was the first to be discovered, followed by its heavier siblings the μ and τ.

Apart from the above mentioned classes of particles all other observed particles have strong interactions and are called hadrons. In this category the proton and neutron is found. This class of particles is more diverse with regards to its main characteristics like spin, electric charge. All hadrons are made up of smaller constituents – quarks. Quarks, which are also spin-$\frac{1}{2}$, and leptons are know collectively as fermions. The quarks are bound together by the strong force to form hadrons. The different types of quarks are coined flavours. All hadrons can be built from combinations of six quarks. Quarks are commonly separated into up (u, c, t) and down (d, s, b) type quarks, with charge $\frac{2}{3}$ and $-\frac{1}{3}$ respectively. There is a large variation in the quark masses, where the top quark is the heaviest and most recently discovered. The six quarks and six leptons (including neutrinos) are commonly grouped into three generations or families, as shown in 2.2. All the quarks, leptons and gauge bosons have an associated antiparticle, with the same

Generation	Name	Symbol	Charge (e)	Mass (GeV)	Type
1.	up	u	$\frac{2}{3}$	$(1.7 \text{ - } 3.3)\cdot10^{-3}$	quark
	down	d	$-\frac{1}{3}$	$(4.1 \text{ - } 5.8)\cdot10^{-3}$	
	e-neutrino	ν_e	0	$< 2\cdot10^{-9}$	lepton
	electron	e	-1	$0.511\cdot10^{-3}$	
2.	charm	c	$\frac{2}{3}$	$1.27^{+0.07}_{-0.09}$	quark
	strange	s	$-\frac{1}{3}$	$(101^{+29}_{-21})\cdot10^{-3}$	
	μ-neutrino	ν_μ	0	$< 2\cdot10^{-9}$	lepton
	muon	μ	-1	$105.66\cdot10^{-3}$	
3.	top	t	$\frac{2}{3}$	$172.0 \pm 0.9 \pm 1.3$	quark
	bottom	b	$-\frac{1}{3}$	$4.19^{+0.18}_{-0.06}$	
	τ-neutrino	ν_τ	0	$< 2\cdot10^{-9}$	lepton
	tau	τ	-1	1.777	

Table 2.2: Particles of the Standard Model - The masses are taken from [7]

mass and spin but opposite charge. The antiparticle of the electron (e^-) is the positron (e^+), and likewise for muons and taus. Antiquarks are denoted by bars - $\overline{u}$, $\overline{d}$, $\overline{s}$, etc. The antiparticle of W^+ is the W^-. The electrically neutral gauge bosons, the γ, Z^0

and gluon, are their own antiparticles.

Quarks and gluons are the only particles acted upon by the strong force. To describe this force it is necessary to introduce a new theoretical concept - colour. Each quark has one of the three colours: red, green or blue, while antiquarks carry the corresponding anti-colours. Gluons on the other hand carry two colours - one colour and one anti-colour. Quarks and gluons interact such that colour is conserved in interactions. Only these coloured objects can interact via gluons, resulting in the strong forces and the theory describing them Quantum Chromodynamics (QCD). Due to colour both gluon-gluon couplings and colour confinement are present in this theory. Colour confinement states that only colourless states are allowed as physical hadrons. Colourless combinations of quarks can either be three quarks with colour red, green and blue - which forms the known baryons; or a quark-anti-quark pair with a colour and its anti-colour - which yields the mesons. The potential energy required to separate two quarks increase linearly with the distance between them r, due to vacuum polarisation. This is what makes it deviate from the familiar inverse square law of other theories with massless gauge bosons. The linear growth of potential energy with r makes the colour ionisation potential infinite. Consequently coloured objects like quarks or gluons can never appear in isolation, but only within colourless hadrons. This means that if one injects energy into a hadron the constituent quarks are not separated, but instead new quark-anti-quark pairs are formed and hence new hadrons. This process is called hadronisation.

There are 19 free parameters in SM, these are not determined by theory but rather must be found experimentally. This includes the masses of the leptons, excluding neutrinos, and quarks, three CKM mixing angles and one CP-violating phase, one gauge coupling for each of the three groups of SM, the QCD vacuum angle and two parameters relating to the Higgs. The neutrinos are assumed to be massless in SM. This proved to be incorrect through the discovery of neutrino oscillations, meaning neutrinos changing flavour, which require a non-zero mass [8]. Neutrino masses can however be incorporated into SM [6].

2.2 Quantum Field Theory Approach

The Standard Model is a quantum field theory, with symmetry group SU(3)×SU(2)×U(1), describing the interaction of spin-$\frac{1}{2}$ point-like fermions, whose interactions are mediated by spin-1 gauge bosons as described above. Quantum field theories combine quantum mechanics with special relativity, allowing for the creation and annihilation of particles. The standard model is made out of local gauge theories, which ensures that calculated observables are finite (renormalisable). A local gauge theory is characterised by the Lagrangian of the theory remaining unchanged by local gauge transformations of the fields of the theory at all space-time points. The bosons and their couplings arise due to this local gauge invariance applied to the fields of the theory. An exact gauge invariance however require massless gauge bosons. The symmetry group of the theory is determined by the symmetry group of these local gauge transformations. A short quantum field theoretical description of the U(1) symmetry of Quantum Electrodynamics (QED) describing the electromagnetic interaction, as well as the unified SU(2)×U(1) theory of electroweak interaction will be made in the following sections. The aim is to shed some light on the key concepts constituting the basics of these theories, rather than a thorough description of the entire theory. The strong interaction is described by the symmetry group SU(3) in the theory of Quantum Chromo Dynamics (QCD). In which quarks, which are triplets under SU(3), interact via gluons carrying colour charge. A quantum field theoretical description of this theory is mathematically intricate, while the fundamental concepts remain the same as in the two theories introduced below. QCD will therefore not be treated further in this thesis.

2.2.1 Quantum Electrodynamics (QED)

The first gauge theory, and by far the simples, was QED. QED is as the name implies the quantum field theory of electrodynamics. The Lagrangian $\mathcal{L}$ for the massless electromagnetic field $A_\mu = (V, A_x, A_y, A_z)$ interacting with a spin-$\frac{1}{2}$ field Ψ of bare mass m is given by

$$\mathcal{L} = -\frac{1}{4}F_{\mu\nu}F^{\mu\nu} + \overline{\Psi}(i\gamma^\mu D_\mu - m)\Psi \tag{2.1}$$

The electromagnetic field tensor, $F_{\mu\nu}$, is given by Eqn. 2.2, while the covariant derivative, $D_{\mu\nu}$ is given by Eqn. 2.3.

$$F_{\mu\nu} = \partial_\mu A_\nu - \partial_\nu A_\mu \tag{2.2}$$

$$D_\mu = \partial_\mu - ieA_\mu Q \tag{2.3}$$

e is the unit of electric charge and Q is the charge operator. The QED Lagrangian is invariant under the local gauge transformations:

$$\Psi(x) \rightarrow U(x)\Psi(x) \tag{2.4}$$

$$A_\mu(x) \rightarrow A_\mu(x) + \partial_\mu \alpha(x) \tag{2.5}$$

That is to say that the physical electromagnetic fields, **E** and **B**, remain unchanged under these transformations. This is analogous to the gauge invariance in classical electrodynamics, where the observable fields remain unchanged for a choice of gauge on the scalar and vector potentials, V and **A**.This requires the addition of an interaction term, between the electromagnetic field A_μ and the spin-$\frac{1}{2}$ field Ψ, to the Lagrangian:

$$\mathcal{L}_{int} = -eJ^\mu_{em}A_\mu \tag{2.6}$$

$$= -e\overline{\Psi}\gamma^\mu Q\Psi A_{mu} \tag{2.7}$$

Where J^μ_{em} is the electromagnetic current.

The Euler-Lagrange equation

$$\partial_\mu \left[\frac{\partial \mathcal{L}}{\partial(\partial_\mu \phi_r)}\right] = \frac{\partial \mathcal{L}}{\partial \phi_r} \tag{2.8}$$

can be obtained from the requirement of stationary action for any field ϕ_r. It yields the equations of motion for electromagnetism:

$$\partial_\nu F^{\mu\nu} = J^\mu_{em} \tag{2.9}$$

$$(i\gamma^\mu D_\mu - m)\Psi = 0 \tag{2.10}$$

From the continuity equation it is clear that the electromagnetic current is conserved, $\partial_\mu J^\mu_{em} = 0$, which in turn implies that electric charge, q, is conserved

$$q = \int J^0_{em} d^3x \tag{2.11}$$

This exemplifies Noethers Theorem which states that for each continuous symmetry there is a corresponding conserved quantity. The above gauge transformation belongs to unitary group U(1), and the Lagrangian thus has a $U(1)_Q$ symmetry, with the charge operator Q as the generator. The procedure is similar, but more mathematically elaborate for the two remaining symmetry groups, SU(2) and SU(3). The weak interaction described by the internal symmetry group, SU(2), can be unified with electromagnetic interaction described above, this procedure will be described in the next section.

2.2.2 The Electroweak Model

Experimentally the weak interaction is found to act upon left-handed fermion states only, thus violating parity, P. The weak interaction is in other words not invariant under spatial reflection. The handedness, chirality, of a particle is introduced to explain this asymmetry, with the left- and right-handed fields defined as

$$\psi_L = \frac{1}{2}(1-\gamma_5)\psi, \qquad \psi_R = \frac{1}{2}(1+\gamma_5)\psi \tag{2.12}$$

A concept closely related to chirality is the helicity of a particle, the two concepts are equal for massless particles. Right handed helicity means that a particle has spin along its direction of motion, while left handed helicity means that the spin is pointing opposite to the direction of motion. In the Standard Model neutrinos are massless with left-handed chirality, while anti-neutrinos are right-handed. Particles are often classified in weak isospin left-handed doublets, and right handed singlets

$$\begin{pmatrix} l \\ \nu_l \end{pmatrix}_L \qquad l_R, \tag{2.13}$$

where l and ν indicate leptons and neutrinos of the SM, and L and R indicate handedness. The conserved quantity of this $SU(2)_L$ group is weak isospin $\mathbf{T}_L$.

In addition to the above symmetry group a $U(1)_Y$ group with conserved quantum number Y, called weak hypercharge is also introduced. This allows for unification of the weak and electromagnetic force. The relation between these two conserved quantum numbers and the electric charge Q is

$$Q = T_3 + \frac{1}{2}Y. \tag{2.14}$$

Right handed fermions transform only under $\mathrm{U}(1)_Y$, while left-handed fermions transform under both $\mathrm{SU}(2)_L$ and $\mathrm{U}(1)$. This leads to the following Lagrangian

$$\mathcal{L} = -\frac{1}{4}\mathbf{W}^{\mu\nu}\cdot\mathbf{W}_{\mu\nu} - \frac{1}{4}B^{\mu\nu}B_{\mu\nu} + \bar{\psi}i\gamma^{\mu}D_{\mu}\psi, \tag{2.15}$$

where $\mathbf{W}_\mu$ is an $\mathrm{SU}(2)_L$ isotriplet, and B_μ is an $\mathrm{U}(1)_Y$ singlet. $\mathbf{W}_{\mu\nu}$, $\mathrm{B}_{\mu\nu}$ and the covariant derivate, D_μ, is defined as

$$\begin{aligned}
\mathbf{W}_{\mu\nu} &= \partial_\mu\mathbf{W}_\nu - \partial_\nu\mathbf{W}_\nu - g\mathbf{W}_\mu\times\mathbf{W}_\nu & (2.16)\\
B_{\mu\nu} &= \partial B_\nu - \partial_\nu B_\mu & (2.17)\\
D_\mu &= \partial_\mu + ig\mathbf{W}_\mu\cdot\mathbf{T} + ig^{'}\frac{1}{2}B_\mu Y. & (2.18)
\end{aligned}$$

The Lagrangian is invariant under infinitesimal local gauge transformation for $\mathrm{SU}(2)_L$ and $\mathrm{U}(1)_Y$. In order to unify the weak and electromagnetic interaction the neutral term of the covariant derivate, $i(gW_{3\mu}T_3 + g^{'}\frac{1}{2}B_\mu Y)$ must include the electromagnetic term, $ieQA$. This allows us to express W_3 and B as linear combination A and another neutral field Z

$$\begin{pmatrix} W_3 \\ B \end{pmatrix} = \begin{pmatrix} \cos\theta_W & \sin\theta_W \\ -\sin\theta_W & \cos\theta_W \end{pmatrix}\begin{pmatrix} Z \\ A \end{pmatrix} \tag{2.19}$$

By expressing W_3 and B in the neutral term in the covariant derivate in terms of Z and A, and using that $ieQA = ie(T_3 + \frac{1}{2}Y)$, it is found that

$$g = \frac{e}{\sin\theta_W}, \qquad g^{'} = \frac{e}{\cos\theta_W}. \tag{2.20}$$

In other words the weak and electromagnetic interactions are unified as for a given θ_W all the gauge couplings, g and $g^{'}$ are determined by the electric charge, e. The theory describes four fields, two neutral the electromagnetic field A and Z, and two charged $W^{\pm} = \frac{1}{\sqrt{2}}(W_1 \mp iW_2)$. These fields correspond to the gauge bosons, γ, Z and $\mathrm{W}^{\pm}$. The interaction of the gauge bosons with the fermion fields, ψ, appear from the term in the Lagrangian containing the covariant derivate, as was the case also in QED. A problem with the models as given above is that both the gauge bosons and fermions are massless. Massive particles are introduced by introducing another field, the Higgs field, which spontaneously breaks the gauge symmetry while the observables of the theory remain finite (renormalisable).

In the standard model where also quarks and gluons are incorporated, also quarks can be separated into left-handed SU(2) doublets, and right-handed singlets as shown for the first generation below

$$\begin{pmatrix} u \\ d \end{pmatrix}_L, \qquad \begin{pmatrix} e \\ \nu_e \end{pmatrix}_L \qquad u_R, d_R, e_R \tag{2.21}$$

The $W^{\pm}$ gauge bosons are responsible for charged current weak interactions, where a unit of electric charge is exchanged as one constituent of the doublets is transformed into the other. Due to quark generation mixing each doublet is not limited to one generation, and W-interactions thus allow all transitions between up- and down-type quarks with a unit charge difference. This mixing between the three generations of quarks is described by the Cabibbo-Kobayashi-Maskawa (CKM) matrix [9, 10]. Z^0 on the other hand is responsible for neutral current weak interactions, where no change of charge or flavor is involved.

2.2.3 The Higgs Mechanism

In the Standard Model the fermion and gauge fields are given masses by introducing a SU(2) doublet of scalar fields Φ which spontaneously breaks the SU(2)×U(1) symmetry. This also introduces another neutral particle, the Higgs boson, and two new terms in the Lagrangian, $\mathcal{L}_\Phi$ and $\mathcal{L}_\Phi^F$. $\mathcal{L}_\Phi^F$ is the Yukawa coupling of Φ to the fermions, which gives rise to the fermion masses. The other term is described as

$$\mathcal{L}_\Phi = |D_\mu|^2 - V\left(|\Phi|^2\right), \tag{2.22}$$

where the scalar potential V is

$$V = \mu^2|\Phi|^2 + \lambda|\Phi|^4. \tag{2.23}$$

And the isodoublet

$$\Phi = \begin{pmatrix} \phi^+ \\ \phi^0 \end{pmatrix}, \tag{2.24}$$

where ϕ^+ and ϕ^0 are complex fields. This mexican hat potential classically has a degenerate non-zero ground state for $|\Phi|^2$ when $\mu < 0$. This is analogous to a non-zero expectation value for $|\Phi|^2$ in the vacuum state in quantum field theory. This non-vanishing vacuum expectation value selects a preferred direction in weak isospin and hypercharge space, and thus breaks the SU(2)×U(1) symmetry. This is commonly

referred to as spontaneous symmetry breaking. By selecting the unitary gauge, $\Phi(x)$ can be written as

$$\Phi(x) = \frac{1}{\sqrt{2}} \begin{pmatrix} 0 \\ v + H(x) \end{pmatrix}. \tag{2.25}$$

By introducing the covariant derivate of the physical fields, A, $W^{\pm}$ and Z, into the Lagrangian in 2.22 the W and the Z fields acquire mass through their coupling to the Higgs field, as

$$M_W = \frac{1}{2} g v, \qquad M_Z = \frac{M_W}{\cos\theta_W}, \tag{2.26}$$

while the photon field remain massless as it does not couple to the Higgs field. The Higgs field itself can be shown to acquire a mass described by

$$m_H = \sqrt{-2\mu^2}. \tag{2.27}$$

2.3 Shortcomings of the Standard Model

Although highly successful, the Standard Model, is widely believed not to be the final theory of particle physics - it has many free parameters and the gauge group is not a simple group, but rather a combination of many. The theory is therefor expected to be valid up to a certain energy scale, where it is replaced by a more fundamental theory. In this respect the Standard Model is regarded as a low energy effective theory. The cutoff is M_{GUT} if the more fundamental theory is a Grand Unified Theory (GUT), where M_{GUT} 10^{15}-10^{19} GeV depending on the GUT.

The GUT mass scale is much higher than the weak scale M_W, which is the typical mass scale of the standard model. The hierarchy problem is the problem of maintaining this mass hierarchy, $M_W << M_{GUT}$. This problem is especially pressing for scalar particles such as the Higgs particle. The Higgs mass-squared gets a quantum correction proportional to M^2_{GUT} which leads to a 'quadratic divergence' in the Standard Model. This correction is from the standard model fermions, f_L and f_R, where the subscripts indicate the handedness of the fermions. This yields the physical Higgs boson mass

$$m_h^2 = (m_h^2)_0 - \frac{1}{16\pi^2}\lambda^2\Lambda^2 + \cdots, \tag{2.28}$$

where the last term is the leading order correction, λ is the Higgs-fermion coupling and Λ is the ultraviolet cutoff if the loop integral, which is at the GUT mass scale. It is possible to adjust the bare mass of the Higgs such that the renormalised Higgs mass

remain at the weak scale. This would however require a fine tuning of the bare mass parameter to the order of $\frac{M_W}{M_{GUT}}^2 \sim 10^{-26}$ which is regarded as unnatural. [11]

There is also large amounts of evidence for the existence of a non-relativistic, weakly interacting type of matter - dark matter (DM) [12]. None of the particles in SM fits the bill for this kind of particle. The weakly interacting particles are either too light (γ, ν), and thus relativistic, or too unstable (Higgs, Z) to be a dark matter candidate. Dark matter thus constitutes a direct hint to the existence of beyond the SM physics and particles. Most evidence for dark matter stems from astrophysics and cosmology, from galactic to cosmological scale. This includes measurement of rotational curves of galaxies [13], measuring the velocities of stars and gas as a function of distance to the galactic centre. This is, if our theory of gravity is correct, solely dependent on the mass contained within this distance. These measurements points towards the existence of a large amount of unseen matter with gravitational interactions in the galaxies. Other evidence for dark matter includes gravitational lensing [14], galaxy cluster composition [15, 16] at the galactic, and galaxy cluster scale. Measurement of the Cosmic Microwave Background (CMB) by WMAP and others [17] and N-body simulations of the large scale structure of the Universe [18] also point towards the existens of DM.

The baryon asymmetry observed in nature is also only partly explained by the Standard Model. The core of this problem is in explaining why there exist such large amounts of matter, while the amount of antimatter is so scarce. The asymmetry stems from a process called Baryogenesis, which creates an excess of baryons over anti-baryons in the early universe, from initially equal amounts [19]. In SM the asymmetry between matter and antimatter is introduced in the CKM matrix through a CP-violating phase. Still, this is not large enough to account for current observations [20]. In some of the models beyond the Standard Model however the necessary baryon asymmetry arise naturally.

Another problem is the unification of the gauge couplings. Each of the three gauge groups in the SM has an associated coupling strength. These are called running coupling as they change with the energy scale of the interaction. Unification of the forces require these to be identical at some large energy scale, whereas they differ at lower energy scales due to spontaneous symmetry breaking. Current extrapolations towards higher energies however shows that these couplings does not intersect at a common point, and hence are not unified.

Other problems for SM is the lack of a quantum description of gravity, explaining the cosmological constant, and an understanding of the sources of flavour mixing and the neutrino masses. Out of all these, the four discussed in more length above are the ones most likely to be solved by new physics near the electro weak scale [19].

There exist many models proposing different ways of solving some or all of these problems. This includes extra dimensions, technicolor and supersymmetry. Perhaps the most studied and theoretically attractive of these is supersymmetry. This is the theory that is the main focus of this thesis. The next sections focus on the basic concepts of this theory, and how it aims to solve some of the problems mentioned above.

3

Supersymmetry

Supersymmetry (SUSY) is a symmetry connecting particles of spin-0 and spin-$\frac{1}{2}$ - bosons and fermions, by the supersymmetry generator Q. It is very theoretically attractive as it solves a host of the problems of the SM. It states that all the known particles have a corresponding 'superpartner'. The superpartner of the fermions are spin-0 bosons, while for the bosons are spin-$\frac{1}{2}$ fermions

$$Q \mid \text{boson}\rangle = \mid \text{fermion}\rangle, \quad Q \mid \text{fermion}\rangle = \mid \text{boson}\rangle$$

While the spins of the superpartners differ from the corresponding standard mode particle, the other quantum numbers (electric charge, weak isospin, color etc.) remain unchanged [21].

3.1 Solutions to Standard Model Problems

Due to the generator of supersymmetry transformation commutating with the generator of space-time translation (4-momentum), the superpartners should have the same mass as their standard model partner. It is nevertheless clear that this symmetry is spontaneously broken as no spin-0 scalar particles with the same charges and masses as those of the quarks and leptons has been observed [11]. The symmetry breaking terms in the SUSY Lagrangian can introduce additional CP-violating phases to those already in the SM [22], and thus potentially explain the observed baryon asymmetry in the Universe.

Breaking supersymmetry means that the masses of the superpartners is unconstrained. However, in order for SUSY to solve the Hierarchy problem these masses are

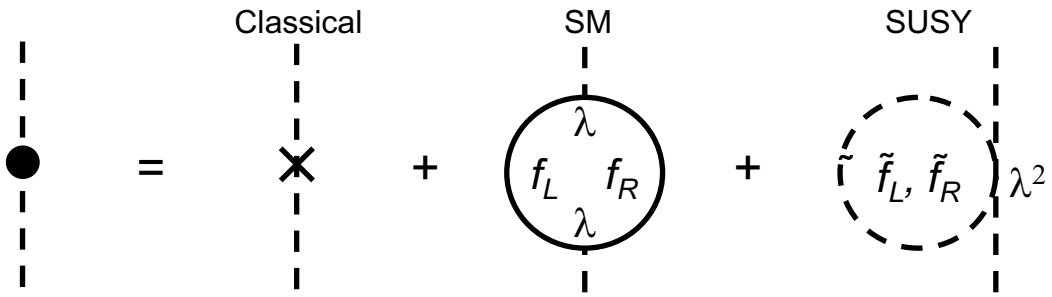

Figure 3.1: Physical mass of the Higgs boson - Quantum corrections from SM and SUSY. Figure taken from [23]

required to be at the weak scale. The coupling constants of a particle and its superpartner are identical, and the Feynman rule provides an additional negative sign for the diagram with a fermion loop (Figure 3.1). In other words, for each quantum correction for a standard model fermion, f_L and f_R, there is a correction for the superpartners, $\tilde{f}_L$ and $\tilde{f}_R$, which means that the physical Higgs mass becomes

$$\begin{aligned} m_h^2 &= (m_h^2)_0 - \frac{1}{16\pi^2}\lambda^2\Lambda^2 + \frac{1}{16\pi^2}\lambda^2\Lambda^2 + \cdots \\ &\approx (m_h^2)_0 + \frac{1}{16\pi^2}(m_{\tilde{f}}^2 - m_{\tilde{f}}^2)\ln\left(\frac{\Lambda}{m_{\tilde{f}}}\right) \end{aligned} \tag{3.1}$$

The quadratic divergences are cancelled by this extra loop, leaving only a logarithmic divergence, thus solving the hierarchy problem [23]. Still the remaining logarithmic divergence, restrain the SUSY breaking mass scale to below 1 TeV (weak scale), in ordet to prevent the Hierarchy problem from arising again.

Although weak scale superpartners solve the Hierarchy problem they also introduce lepton and baryon number violation at unacceptable rates, which for example would lead to proton decay ($p \to \pi^0 e^+$). This problem can be solved by introducing conservation of a quantity called R-parity. R-parity is defined as

$$R \equiv (-1)^{3(B-L)+2S}, \tag{3.2}$$

where B, L and S are baryon number, lepton number and spin respectively. Standard model particles all have R = 1, and supersymmetrv particles has R = -1, which means that superpartner particles can only be created or destroyed in pairs. This in turn

means that the lightest superpartner, the LSP, is stable. If the LSP is also neutral under colour and electromagnetism, i.e. it does not interact through either the strong or the electromagnetic force, it constitutes a dark matter candidate [11].

Name	**Spin 0**	**Spin $\frac{1}{2}$**	**Spin 1**
squarks, quarks	$\tilde{Q} = (\tilde{u}_L, \tilde{d}_L)$	$Q = (u_L, d_L)$	
	$\tilde{u}_R^*$	$\bar{u}_R$	
	$\tilde{d}_R^*$	$\bar{d}_R$	
sleptons, leptons	$\tilde{L} = (\tilde{\nu}, \tilde{e}_L)$	$L = (\nu, e_L)$	
	$\tilde{e}_R^*$	$\bar{e}_R$	
Higgs, Higgsinos	$H_u = (H_u^+, H_u^0)$	$\tilde{H}_u = (\tilde{H}_u^+, \tilde{H}_u^0)$	
	$H_d = (H_d^0, H_d^-)$	$\tilde{H}_d = (\tilde{H}_d^0, \tilde{H}_d^0, \tilde{H}_d^-)$	
gluino, gluon		$\tilde{g}$	g
winos, W's		$\tilde{W}^{\pm}$, $\tilde{W}^0$	$W^{\pm}$, W^0
bino, B		$\tilde{B}$	B

Table 3.1: Particles in MSSM. After symmetry breaking: five physical Higgs bosons (h, H, A and $H^{\pm}$). Winos, binos and Higgsinos mix to give four neutralinos ($\tilde{\chi}_i{}^0$) and two charginos ($\tilde{\chi}_i^{\pm}$). W^0 and B mix as in the SM [24].

3.2 MSSM, mSUGRA and Main Parameters

In the Minimal Supersymmetric extension of the Standard Model (MSSM) R-parity is conserved and each fermion $f_{L,R}$ has a scalar sfermion partner $\tilde{f}_{L,R}$, and each massless gauge boson A_μ has a massless spin-$\frac{1}{2}$ gaugino partner, both with two helicity states [25]. There is also two complex Higgs doublets with associated Higgsinos. The squarks and sleptrons come in three generations. The physical Higgs bosons after symmetry breaking are h, H, A and $H^{\pm}$. After symmetry breaking the winos and bino mix with the Higgsinos to give four neutralinos $\tilde{\chi}_i{}^0$ and two charginos $\tilde{\chi}_i^{\pm}$, and the W^0 and B mix as in the Standard Model [24]. All the MSSM particles are listed in Table 3.1. Although MSSM solves the problems of the SM mentioned above it introduces 105 new parameters in addition to those already in SM [24].

In order to reduce the number of parameters some theoretical assumptions are made, particularly relating to the manner in which the SUSY symmetry is broken. It is however not possible to spontaneously break SUSY using only MSSM fields. This

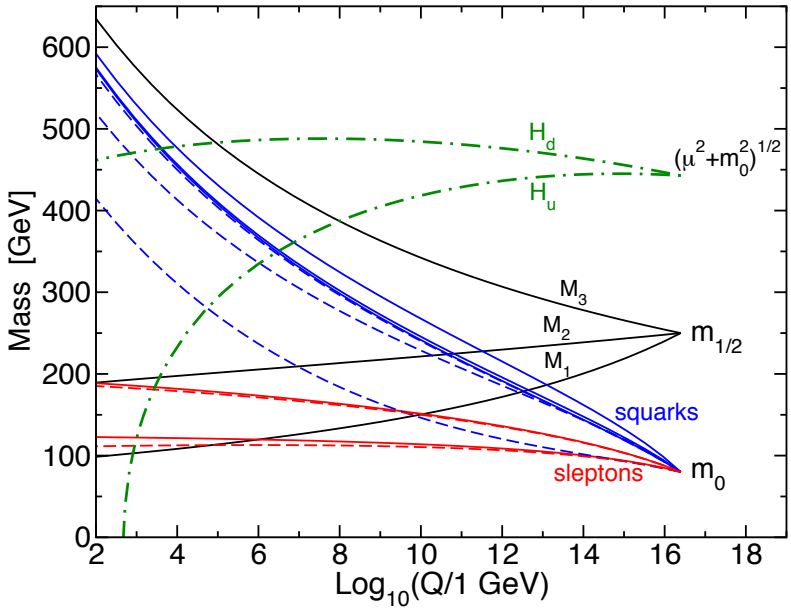

Figure 3.2: Evolution of mass parameters in MSSM - Evolution of scalar and gaugino masses in MSSM, $Q_0 = 2.5 \cdot 10^{16}$ GeV. Figure taken from [21]

is solved by introducing something called a hidden sector which breaks SUSY and communicates the breaking to the MSSM sector via a messenger interaction. In supergravity (SUGRA) models this messenger is gravity [24] In the minimal SUGRA model (mSUGRA) squarks, sleptons and Higgs bosons have a common mass m_0, while the gauginos have a common mass $m_{\frac{1}{2}}$ at the GUT scale. These common masses split into the various sparticle masses at the weak scale through renormalisation group equations (RGEs) (an example mass splitting is shown in Figure 3.2) [24]. RG evolution of the couplings shows that MSSM has the right particle content for the couplings to unify at a common scale, while the SM couplings does not show this unification (Figure 3.3).

The main parameters of mSUGRA can be reduced to five:

$$\mathrm{m}_0,\ \mathrm{m}_{\frac{1}{2}},\ \mathrm{A}_0,\ \tan\beta,\ \mathrm{sign}(\mu)$$

m_0 is the universal scalar mass and $m_{\frac{1}{2}}$ is the universal gaugino mass, both defined at the GUT scale. $\tan\beta$ is defined as

$$\tan\beta \equiv \frac{\langle H_u \rangle}{\langle H_d \rangle}, \tag{3.3}$$

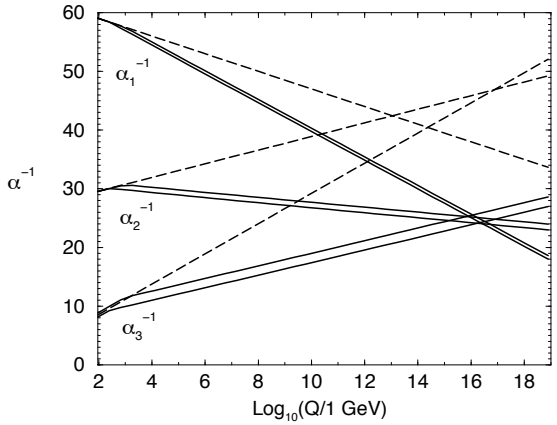

Figure 3.3: Evolution of couplings in the SM and MSSM - dashed lines are SM, solid lines are MSSM. Figure taken from [21].

where H_u and H_d are the vacuum expectation value of the SUSY Higgs particles that gives masses to up- and down-type fermions respectively [23] A_0 is the common value of the trilinear Higgs-sfermion-sfermion couplings at the GUT scale. sign(μ) is the sign of the SUSY conserving Higgs mass [24]. These parameters determine the phenomenology of the SUSY model, with different values corresponding to different sparticle masses, mixing, decays, branching rations and production cross sections. Which in turn determine whether one gets a suitable dark matter candidate (e.g. neutralino LSP), an observable signal (large enough production cross section and branching fraction to observable particles) and a theoretically acceptable predictions (electro weak symmetry breaking) among other things from a set of parameters.

3.3 The Co-annihilation Region

One of the most important experimental constraints on SUSY models is the amount of dark matter in the Universe. This measurement alone rules out large portions of the SUSY parameter space as most of it predict a too high relic dark matter density. Processes to limit the production of DM is thus necessary. One such process is co-annihilation between the LSP and sparticles. The region of the mSUGRA parameter space where this process yields acceptable rates of DM is called the co-annihilation region.

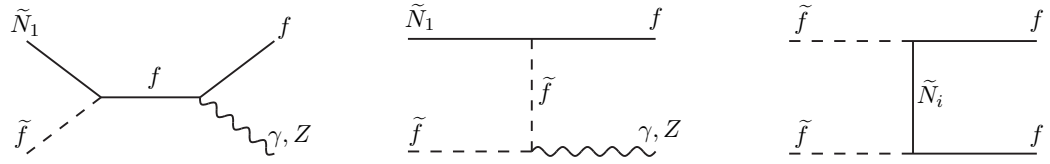

Figure 3.4: Co-annihilation diagrams - Contributions to the co-annilation of dark matter neutralino, $\tilde{N}_1$, LSP. The sfermion, $\tilde{f}$, is here a stau, $\tilde{\tau}$. Figure taken from [21].

In SUSY the early universe contains both supersymmetric and SM particles in thermal equilibrium. As the Universe expands and cools the energy density consequently drops, until it reaches the point where SUSY particles can no longer be produced. The heavier SUSY particles then decay and annihilate into lighter particles, leaving the neutralino LSP as the only remaining SUSY particle. Some of the LSPs will in turn annihilate and decay into SM particles. The amount of LSP annihilation decrease as the Universe expands and the density of LSPs drop. The point at which the annihilation rate becomes negligible the LSP is said to 'freeze out', and the LSP density remain the same from this point onwards. In other words the dark matter density today is determined by the annihilation rate of the LSP and the expansion of the Universe [21]. This annihilation rate is however not only determined by the pair-annihilation among LSPs. If there are other sparticles which are close to the LSP in mass co-annihilation between these particles and the LSP is made possible as these particles will exist in significant numbers along with the LSP at the freeze out time. The Feynman diagrams of some of the co-annihilation processes further limiting the dark matter density can be seen in Figure 3.4. Co-annihilation between the LSP and the stau, where the mass difference between the two is small, is the process of interest to the analysis presented in this thesis. In a collider experiment such a signal of SUSY model would be identifiable by a tau created with the stau, followed by another tau when it decays. In addition energetic jets from earlier steps in the decay chain as well as missing energy from the escaping LSP are expected

4

The ATLAS experiment

This chapter builds heavily on information from [26], which should be consulted for further details. Unless explicitly stated otherwise facts and figures are all from this source. The Large Hadron Collider (LHC) at CERN is a circular particle collider with a circumference of 27 km operating 100 m under ground at the French-Swiss border. It is designed to collide protons at a record centre of mass energy of 14 TeV with a luminosity of $10^{34}\text{cm}^{-2}\text{s}^{-1}$.

In these collisions, commonly referred to as events, a large number of particles are created due to the high energy of the collisions. This is from the relation between mass and energy famously described by Einstein

$$E^2 = m^2c^4 + p^2c^2, \tag{4.1}$$

where c is the speed of light, E is energy, p is momentum and m is the rest mass. This means that the higher the available energy, the heavier particles may be created. This opens for the possible discovery of new physics processes and particles heavier than those currently within our experimental reach.

Instantaneous Luminosity is a measure of the number of events per unit time defined as

$$\mathcal{L} = \frac{\dot{N}}{\sigma}, \tag{4.2}$$

where $\dot{N}$ is the number of interactions per unit time, and σ is the cross section. The cross section is a measure of probability for an interaction to occur, measured in unit area, often in units barn (b) $1\text{b} = 10^{-28}\text{cm}^2$. A common measure of the amount of data collected is integrated luminosity, $\int Ldt$, measured in inverse barns. The design

luminosity is obtained by colliding bunches of protons, with 23 interactions per crossing at intervals of 25 ns. As new physics processes and the production of new and heavy particles are extremely rare, and the discovery of these are determined by statistical significance, it is vital to accumulate large amounts of events within a reasonable amount of time. This makes the luminosity of the LHC one of the most important parameters of the experiment. Currently LHC are operating at a centre of mass energy 7 TeV and luminosity of $4.67{\cdot}10^{32}\mathrm{cm}^{-2}\mathrm{s}^{-1}$.

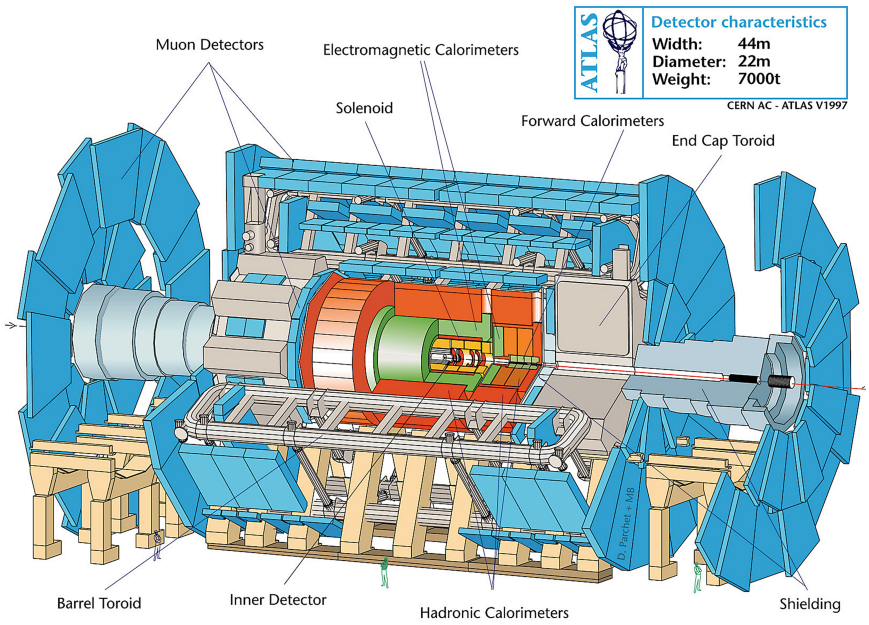

Figure 4.1: Overview of the ATLAS detector - The figure shows the different components of the ATLAS detector, taken from [27].

The particles created in the collisions and the secondary particles they decay into, are observed by large detectors placed at each of the four interaction points of the LHC, where the particle beams are crossed and collided. The four detectors are designed to investigate different physics processes, and therefor differ in composition and constituent components. ALICE is a detector for studying heavy ion processes and collisions, in the period when the LCH collide lead ions. LHCb studies primarily b-physics, which is processes containing bottom quarks. CMS and ATLAS are both multipurpose detectors, constructed in order to study a broad range of physics processes, both known and as of yet undiscovered. As this thesis is deals with physics at the ATLAS experiment,

the following sections will describe the main aspects of the ATLAS detector in more detail.

4.1 Geometry

The geometry of the ATLAS detector is defined such that the beam axis coincides with the z-axis. The x-y plane is the plane transverse to the beam direction, called the transverse plane. The positive x-axis is defined to point towards the centre of the LHC ring, while positive y direction is upwards. There are two main angles used in ATLAS; the azimuthal angle, ϕ, and the pseudorapidity, η. The azimuthal angle represents the angle around the beam axis, while the pseudorapidity is the angle from the beam axis. However, the pseudorapidity is not the standard polar angle, θ, but can be expressed in terms of it:

$$\eta = \ln \tan \frac{\theta}{2} \tag{4.3}$$

Variables denoted by the subscript T are variables measured in the transverse plane. A frequently used measure is the distance ΔR in the pseudorapidity-azimuthal angle space defined as:

$$\Delta R = \sqrt{\Delta\phi^2 + \Delta\phi^2} \tag{4.4}$$

4.2 The ATLAS Detector

The ATLAS detector (Figure 4.1) has a cylindrical geometry and is placed at one of the interaction points of the LHC ring. It is made of four main parts. Closest to the interaction point is the inner detector, which is used for precision measurement of tracks and vertices. The next detector layer is the calorimeters, which are responsible for measuring energies of particles. The outermost layer is the muon spectrometer. As the name implies this part is responsible for detecting muons, as these often traverse all the other layers of the detector. In addition to these three detector parts, there is a last main component - the magnet system. The magnets are not used for detecting particles as the other parts are, but rather to bend charged particles which allows measurement of the particles momenta. The main components of the ATLAS detector is in order from closest to further from the beam line described below.

4.3 Inner Detector

The Inner Detector (ID) in turn consists of three sub detectors. As the track density at the LHC is very large high-resolution detectors are required for precision momentum and vertex measurement. It provides full tracking coverage over $|\eta| \leq 2.5$, impact parameter measurement and vertexing for heavy-flavour and τ-tagging [26]. The intrinsic resolutions of the ID for the barrel and end-cap region is shown in Table 4.1.

Detector	**Intrinsic resolution (μm)**	
	Barrel	End-cap
Pixel	10 ($R-\phi$), 115 (z)	10 ($R-\phi$), 115 (R)
SCT	17 ($R-\phi$), 580 (z)	17 ($R-\phi$), 580 (R)
TRT	130	-

Table 4.1: Intrinsic ID resolutions - for the ID sub-detectors in the barrel and end-cap. Table taken from [28]

4.3.1 Pixel Detector

Closest to the interaction point, at a radius of 4 cm, there is a pixel detector consisting of three layers and covering the pseudorapidity region $|\eta| < 2.5$ [28]. Due to its proximity to the interaction point this part of the ID is important for detecting short lived particles such as B hadrons and taus.

4.3.2 Semiconductor Tracker

Just outside the pixel detector there are eight layers of a semiconductor tracker, made of silicon mictrostrips (SCT). It measures momentum, impact parameter, vertex position in addition to providing good pattern recognition.

4.3.3 Transition Radiation Tracker

The Transition Radiation Tracker (TRT) is a xenon-based straw tube detector running parallel to the beam axis, covering the pseudorapidity region $|\eta| < 2.0$ [28]. This detector has lower precision but also less material per measured point than the two other parts of the inner detector. It is important for momentum measurement, where the lower precision is compensated for by the large number of measured points (about

36) and higher average radius. It also allows for electron identification by detecting transition-radiation photons created between the straws.

4.4 Calorimeters

There is two calorimeters in the ATLAS detector - an electromagnetic (EM) calorimeter and a hadronic calorimeter shown in Figure 4.2. Calorimeters are used mainly to determine particle energies, but also provide particle identification and position information. As the name implies the EM calorimeter measures the energies of particles which interact electromagnetically, e.g. photons and electrons/positrons, while the hadronic calorimeter measures the energies of hadrons.

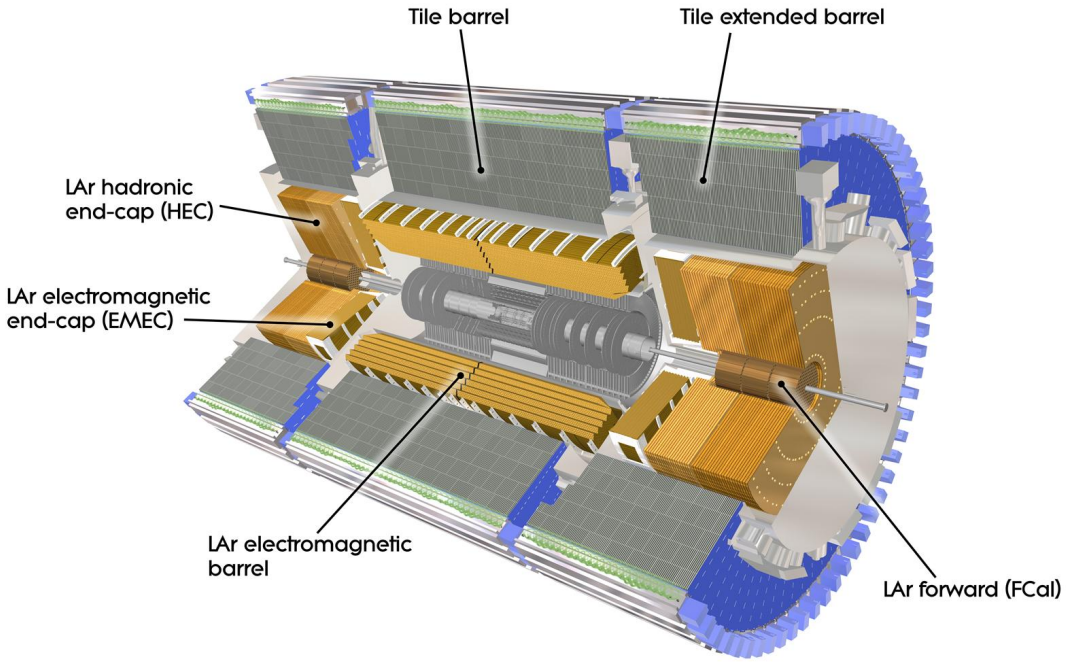

Figure 4.2: The ATLAS calorimeters - The figure shows an overview of the ATLAS calorimeters, taken from [28].

The EM calorimeter covers the pseudorapidity region $|\eta| \leq 3.2$, this includes both a barrel and an end-cap part. It is a lead/liquid-argon (LAr) sampling calorimeter, which is to say that it has a sandwich structure of LAr and lead plates. The lead plates

are passive absorbers inserted to slow down the particles more effectively than LAr, allowing for measurement over shorter distances than would be required with a pure LAr calorimeter due to higher density of Pb. The deposited energy in the active LAr plates are measured, and from this the total energy of the particle is deduced.

The hadronic calorimeter covers a region $|\eta| \leq 4.9$. It is separated into three calorimeters - the barrel calorimeter, the hadronic end-cap calorimeter (HEC), and the high density forward calorimeter (FCAL). Different types calorimeters are used for different angular regions. In the barrel an iron-scintillating-tile calorimeter is used. This is a sampling calorimeter that has an active plastic scintillator part, and passive iron tiles. The HEC and FCAL are LAr calorimeters.

An important parameter for the hadronic calorimeter is its thickness. It has to provide good containment of hadronic showers to reduce punch-through, that is that the particle is stopped completely in the calorimeter and does not escape into to muon system that lies just outside the hadronic calorimeter. The thickness in addition to the good η-coverage is important for an accurate missing energy measurement, which is an important parameter for many physics signatures. This is important since the SM neutrinos in addition to some beyond the standard model particles escape detection, and therefore show up in the experiment as missing energy. The ATLAS performance goals for resolution and $|\eta|$ coverage for each detector part is shown in Table 4.2.

Detector	**Resolution**	$\|\eta\|$ coverage
Tracking	$\frac{\sigma_{p_\mathrm{T}}}{p_\mathrm{T}} = 0.05\% \cdot p_\mathrm{T} \oplus 1\%$	± 2.5
ECAL	$\frac{\sigma_E}{E} = \frac{10\%}{\sqrt{E}} \oplus 0.7\%$	± 3.2
HCAL barrel/end-cap	$\frac{\sigma_E}{E} = \frac{50\%}{\sqrt{E}} \oplus 3\%$	± 3.2
HCAL forward	$\frac{\sigma_E}{E} = \frac{100\%}{\sqrt{E}} \oplus 10\%$	$3.1 < \|\eta\| < 4.9$
Muon spectrometer	$\frac{\sigma_{p_\mathrm{T}}}{p_\mathrm{T}} = 10\%$ at p_T= 1TeV	± 2.7

Table 4.2: Performance goals ATLAS - Units for energy and transverse momentum is GeV. The values are taken from [28]

4.5 Muon and Magnet System

The inner parts of the ATLAS detector are surrounded by superconducting magnets producing an intense magnetic field, which allows for momentum measurement of par-

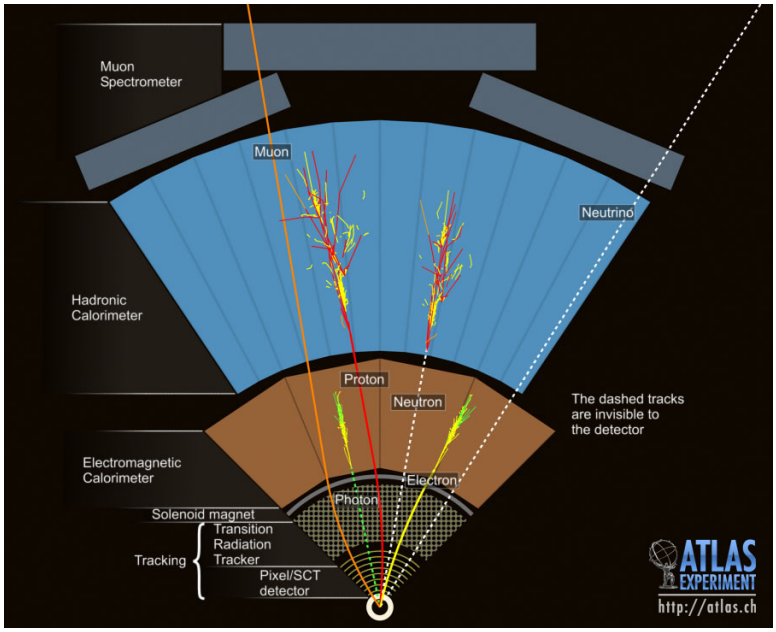

Figure 4.3: Detection of particles in ATLAS - The figure shows the signatures different particles leave in the ATLAS detector, taken from [29].

ticles. The central solenoid (CS) produces the magnetic field for the inner detector, and is placed inside the EM calorimeter. Three air-core toroids generate the magnetic field for the muon spectrometer (MS), which is responsible for detecting muons as these particles traverse all the other detectors. These magnets are also instrumented with a trigger and high-precision tracking chambers. The magnets measure the momenta of muons from the deflection of the muon tracks. There are also two end-cap toroids (ECT) inserted in the barrel toroid (BT) at each end of the detector. The bending of the tracks is performed by the large barrel toroid, the smaller end-cap magnets or a combination of both these for different pseudorapidity regions. The CS provides a central field of 2 T. Figure 4.3 shows schematically the detection of particles in ATLAS, and the signatures of different particles in the detector.

4.6 Trigger and Data Acquisition System

The ATLAS trigger and data-acquisition (DAQ) consists of three levels of online event selection. A trigger is the first and most basic event selection tool. It looks for characteristics in an event that signals that a collision of physical interest has taken place.

From an initial collision/event rate of 40 MHz, the rate of selected events has to be reduced to the order of 100 Hz for permanent storage. As storing and processing a larger rate of events than this would not be feasible considering available storage capacity. This means that about 100 Hz of events should fire the triggers. In other words one require a large rejection rate that should not ideally be acquired at the expense of a good efficiency. An excellent efficiency is needed since the physics processes searched for are very rare.

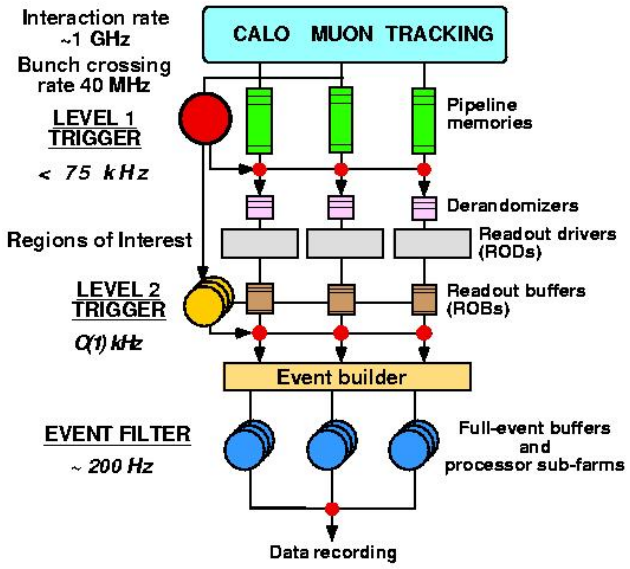

Figure 4.4: Trigger overview - The figure shows an overview of the ATLAS trigger system with trigger rates.

The first trigger, the level-1 (LVL1) trigger makes an initial selection on high transverse-momentum electrons, muons, taus, photons or jets, in addition to large missing and total transverse energies. As these are all basic properties of collisions containing physics of interest. The LVL1 trigger can require combinations of these objects or veto events containing certain objects. The maximum rate for the LVL1 trigger is 75 kHz. Another important task of the trigger is to identify the bunch crossing of interest. This is made difficult by the short time interval between bunch crossings (25 ns), which means that parts of the detected signal remain in the detector over many bunch crossings. Naturally it is also desirable to keep the trigger latency, the time in which the trigger is in-operational , at a minimum.

If an event passes the LVL1 trigger the data is temporarily stored, before it is passed on to the level-2 (LVL2) trigger. This trigger makes use of the 'region-of-interest' determined by the LVL1 trigger, which includes information on position and p_{T} of candidate objects and energy sums. This way the LVL2 trigger only needs a fraction of the full event data to make the LVL2 trigger decision, thus saving time on data transfer between the two triggers. The LVL2 trigger should reduce the rate to about 1 kHz. Among the refinements made to the LVL1 trigger selection, is using finer granulation p_{T}-information, ID and isolation requirements.

After the LVL2 trigger, the last stage of the online selection is performed by the event filter (EF). This filter applies offline algorithms and makes use of alignment and magnetic field information to make refinements to the previous selection. The events selected by the EF are written to permanent mass storage, which is subsequently made available for offline analysis. The rate of events passing the EF should be about 100 Hz, corresponding to about 100 MB/s of data. Figure 4.4 shows the different parts of the ATLAS triggers, and the corresponding trigger rates.

4.7 Computing Tools

The ATLAS data comes in many different forms, shapes and sizes, each serving different purposes in different stages of an analysis. Starting from the large raw output of the detector or simulation to the more manageable format used by the individual physicist to the final distilled result in form of a histogram or table, and many more in between. The main data formats can be seen in Figure 4.5.

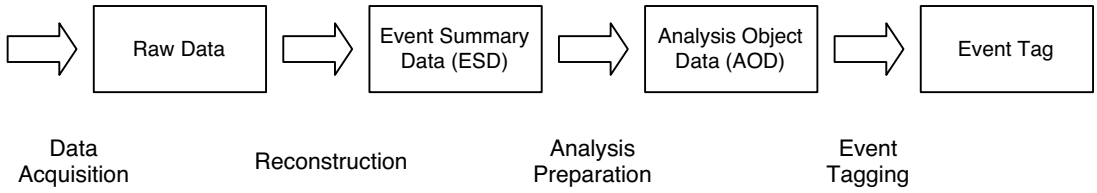

Figure 4.5: Data formats - Order of creation of the different data formats at ATLAS. Figure taken from [25]

The Event Filter outputs information on events as RAW data. As the name implies this is large and unprocessed information as delivered from the detector. This RAW

data is output at about 200 Hz from the EF, with an event size of about 1.6 MB. The RAW data is then transferred from EF to Tier-0 for reconstruction and Event Summary Data (ESD) is produced. The event size is now reduced to 500 kB, and events consist of physics objects rather than the bit representation of the events as in RAW data. ESDs are made such that they can be used instead of RAW data for most physics scenarios except for some calibration and re-reconstruction [25]. From ESDs the data are further reduced to Analysis Object Data (AOD) at a size of about 100 kB per event. At this stage the data contains physics objects of analysis interest. TAG data is also often created. This keeps only basic event-level data which enables efficient and quick selection of events of interest to an analysis. These files are kept in a relational database, each event only claiming about 1 kB of space. The main data format used in this analysis is however Derived Physics Data (DPD). DPD is an n-tuple representation of event data made for end user analysis, and allows for direct analysis by common analysis tools, e.g. ROOT.

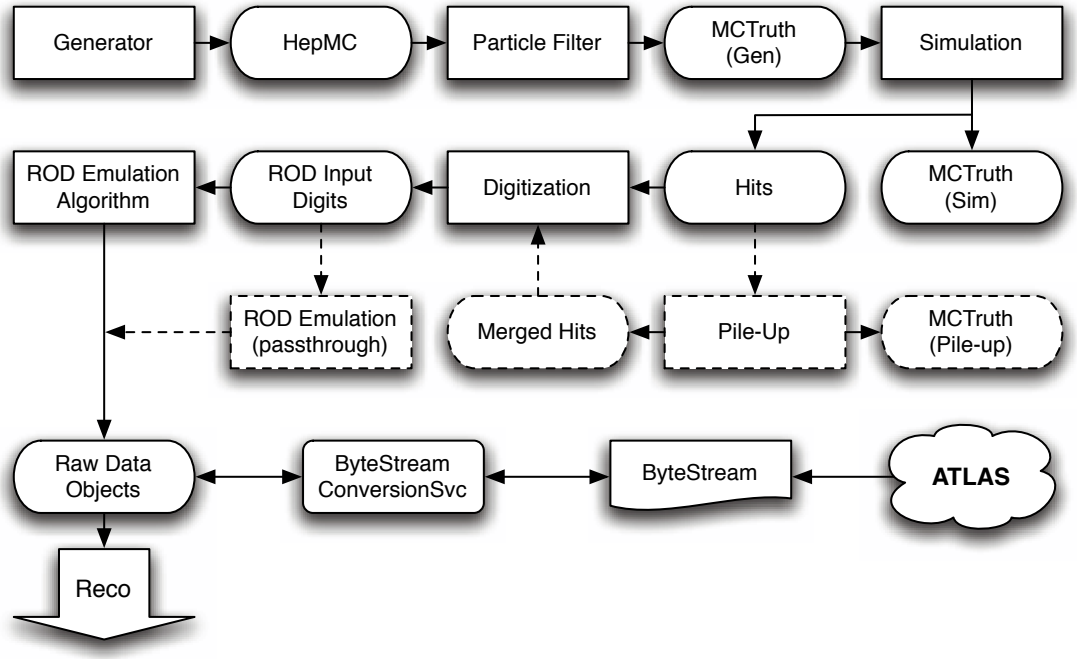

Figure 4.6: Simulation flow chart - Shows a simplified overview of the stages involved in creating simulations (and collecting ATLAS data) up until the RAW data format. Figure taken from [25]

The main components of an ATLAS simulation is shown in Figure 4.6. The first step

is generating the initial particles and their properties in an experiment, events, which at LHC energies means the creation of hundreds of particles. This includes among other things hadronisation, decays and beam remnants. Generators are run inside Athena. Common generators include Herwig, Pythia and Isajet. Monte Carlo truth information from the generator is then further processed by simulating the detector response and effects of digitisation, optionally including pile-up effects. This can be done using GEANT4 (G4ATLAS), which simulates the passage of particles through matter and a given detector's response. As with most simulations there is a trade-off between the simulation accuracy and CPU time required to perform the simulation. For this reason a fast simulation has been created, Atlfast. Atlfast simulates ATLAS physics events, including the detector response and effects due to the software reconstruction chain [25]. The final output of the simulation is RAW data files. Whereupon the same steps as described for data are made to create the other data formats.

The analysis in this thesis makes use of MC and data from release 15 reprocessing. The main software used for the analysis on D3PDs is ROOT. ROOT is a C++ (with CINT interpreter) based and object oriented framework developed at CERN. This is used for analysing data by using ROOTs many built in tools. This includes both statistical, mathematical tools, as well as tools for producing and manipulating graphical output like histograms and graphs.

5

The Tau Lepton at ATLAS

The tau lepton is the heaviest of all the leptons, with a mass of 1.77 GeV. Unlike the electron, the tau is not stable, but decays rapidly with a lifetime of 290.6 fs. The tau therefore differs from the two other leptons in that it is not detected directly, but rather through its decay products. There are two main decay modes for taus – hadronic and leptonic. The latter means that it decays into another lepton and two corresponding neutrinos, while the former is decay into hadrons and a tau neutrino.

Decay mode	**Branching fraction (%)**
$\tau \to \mu^- \bar{\nu}_\mu \nu_\tau$	17.36 ± 0.05
$\tau \to e^- \bar{\nu}_e \nu_\tau$	17.85 ± 0.05
$\tau \to h^-(nh^0)\nu_\tau$	49.51 ± 0.10
$\tau \to h^- h^- h^+(nh^0)\nu_\tau$	14.56 ± 0.08
$\tau \to h^- h^- h^- h^+ h^+(nh^0)\nu_\tau$	0.102 ± 0.004

Table 5.1: Tau decays - $h^\pm$ stands for $\pi^\pm$ or $K^\pm$ and h^0 is π^0. The first three are one prong, while the others are three and five prong decays. Numbers taken from [7]

The hadronically decaying tau channel is often referred to as a tau jet. Due to charge conservation the hadronically decaying tau result in an odd number of charged hadrons, commonly 1 or 3, but also into 5 in a small number of cases. These different scenarios are often referred to as one-, three- or five prong taus. The mort important tau decays can be seen in Table 5.1.

In MC simulated data one has complete knowledge of the actually particles and their properties contained in a simulated event, called truth information. In the case

Process	ID	Sample
$t\bar{t}$	105200	e510, s624, s633, r1064, r1051
QCD J0	115849	J0_pythia_Perugia2010, e568, s766, s767, r1303
QCD J1	115850	J1_pythia_Perugia2010, e568, s766, s767, r1303
QCD J2	115851	J2_pythia_Perugia2010, e568, s766, s767, r1303
QCD J3	115852	J3_pythia_Perugia2010, e568, s766, s767, r1303
QCD J4	115853	J4_pythia_Perugia2010, e568, s766, s767, r1303

Table 5.2: MC samples used - in chapters 5 and 6. All the MC is mc09 at 7 TeV. $t\bar{t}$ sample is produced locally at UIB. Full filenames can be found in AMI from the tags.

for the measured data, on the other hand, raw measurements of variables such as energy depositions, positions and momenta are processed and reconstructed by different algorithms to represent a given particle with certain properties. Combining this knowledge with using the same set of tools and algorithms as for the data to account for the response of the detector and reconstruction of these truth particles; one knows what a true particle should look like after undergoing detection and reconstruction, a so called reconstructed particle. Another way of looking at is to think of the truth particle as what would be detected by a perfect detector, while the reconstructed particle is what we actually observe. Comparing the true particles with what is detected and reconstructed provides invaluable information that may be used to identify particles and distinguish events from different physics processes.

5.1 Tau Reconstruction

Reconstructed taus in ATLAS refers to hadronically decaying taus only, as leptonic decay products from taus often are impossible to distinguish from primary leptons. As the neutrinos always escape detection, we do not have the complete information of the initial tau lepton. Only the hadronic part of the tau lepton decay is known, often referred to as a tau jet. From this visible part the properties of the initial visible tau can be reconstructed using various algorithms. The ATLAS tau reconstruction [30] (taurec) constructs tau candidates from seeds in the tracker, calorimeter or both of these.

A track seeded candidate is built if there exists a track with $p_{\mathrm{T}} > 6$ GeV which also

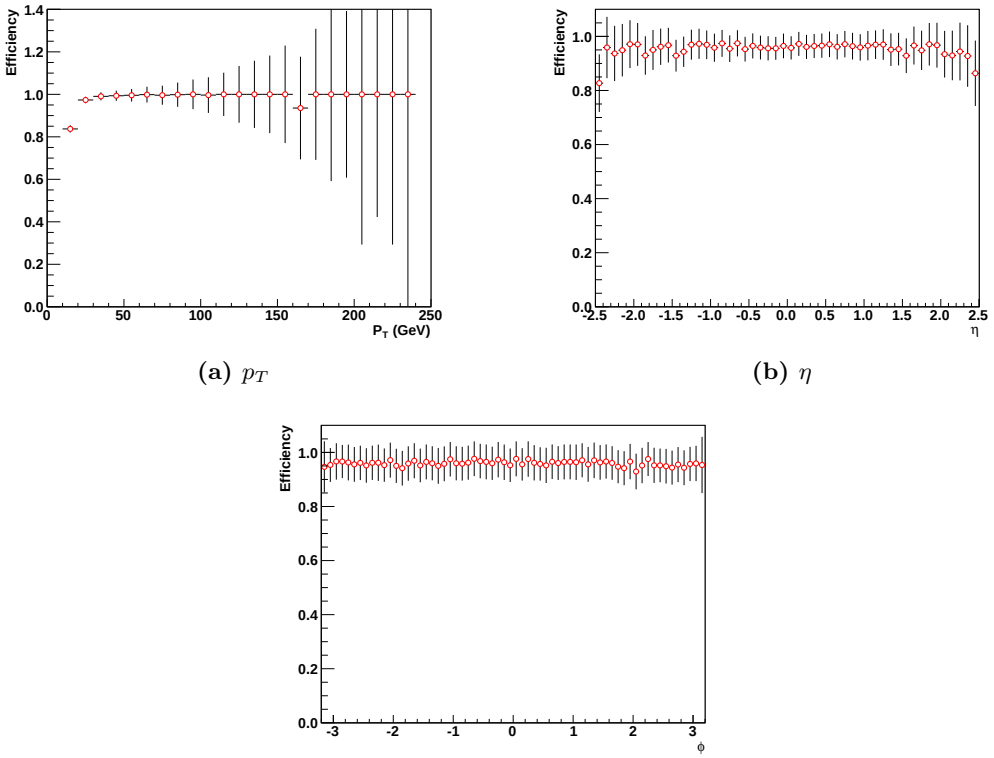

(a) p_T **(b)** η

(c) ϕ

Figure 5.1: Tau reconstruction efficiency - for hadronically decaying taus with $p_T > 15$ GeV and $|\eta| < 2.5$ in $t\bar{t}$ events.

passes quality criteria based on a minimum number of hits in the silicon tracker (≥ 7) and the track impact parameter with respect to the primary vertex. If this track matches a calorimeter jet within $\Delta R < 0.2$, the tau candidate is double-seeded [30]. Calorimeter seeds are made by any jet (AntiKt4TopoJet) above 10 GeV, tracks are then matched to this calorimeter seed, but with less stringent criteria than for the track-seeded case.

The efficiency of tau reconstruction with respect to p_T, η and ϕ can be seen in Figure 5.1, for hadronically decaying taus with $p_T > 15$ GeV and $|\eta| < 2.5$. The efficiency is seen to fall for lower p_T taus and larger $|\eta|$, while it remain stable for all ϕ. The average efficiency is about 95% for the reconstruction of hadronic taus in the $t\bar{t}$ sample.

The author number indicates whether the tau was constructed by information from the tracker, calorimeter or both. If the tau is seeded from information from the tracker,

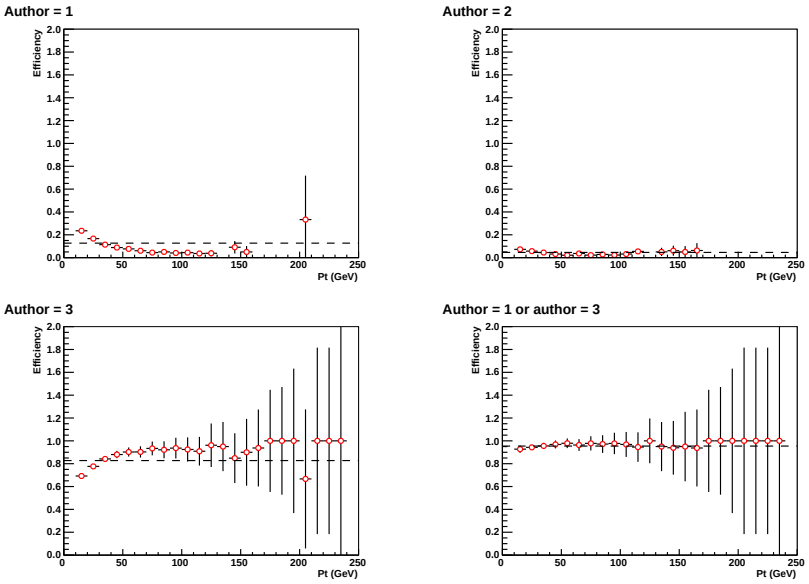

Figure 5.2: Fraction of taus with tau reconstruction seed at tau p_{T} - Fraction of taus with calorimeter (author=1), track (author=2) or both seeds (author=3) at tau p_{T}. Dashed line is average fraction.

the reconstructed tau has author number two, and is called track seeded. On the other hand if the tau is seeded from calorimeter information, the tau has author number one, and is called calorimeter seeded. If the tau reconstruction is seeded from both the tracker and the calorimeter the author number is three. The fraction of reconstructed tau candidates with a given author as a function of p_{T} can be seen in Figure 5.2. The dashed line is the average efficiency. Reconstruction with both seeds has the largest average efficiency, i.e. most selected taus, about 80%, but drops off at low p_{T}. Calorimeter seeded taus has an average efficiency of about 10% that increases for lower transverse momenta of the tau. The track only seeded taus have the largest efficiency at low p_{T} with an average of about 5%, before dropping off to about 3-5% at higher p_{T}. Selecting taus with one of the calorimeter seeds, 1 or 3, yields a quite stable at an efficiency of about 95%.

Figure 5.3 shows the fraction of reconstructed tau candidates reconstructed with one or three tracks. One track is most common with an average at about 65%, while three track taus average is just above 15%. That most tau candidates are reconstructed with one track is not surprising, taking into account the decays given in 5.1. The remaining

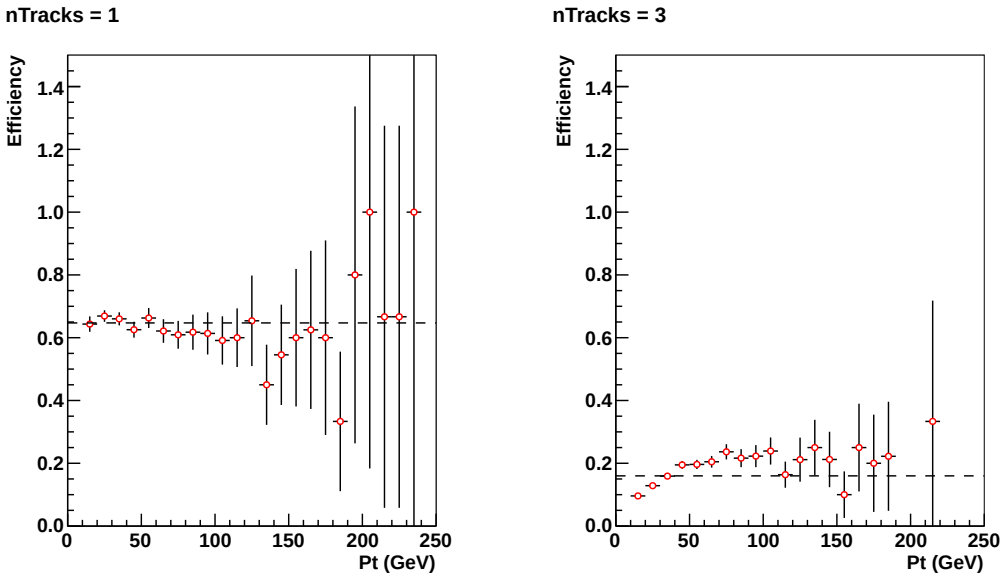

Figure 5.3: Fraction of taus with number of tracks at tau p_{T}. - Reconstruction with one or three tracks. Dashed line is average.

tau candidates are reconstructed with two or more than three tracks, and are more likely to be QCD jets as will be seen in section 5.2.3.

The performance and different qualities of these algorithms can be investigated using Monte Carlo truth information. If one uses truth matching, it is also possible to look at differences in between true reconstructed taus and QCD jets that have been mistakenly reconstructed as tau jets. This information can in turn be used to reject a larger amount of the QCD jets that have been reconstructed as tau jets, and thus avoid using these in our analysis. The MC samples used to study the tau reconstruction and identification is listed in Table 5.2.

Truth matching enables us to find the reconstructed particle corresponding to a given truth particle. This is done by looking for a reconstructed particle that lies within a cone of $\Delta\mathrm{R} < 0.1$, in η - ϕ space of the truth particle. This matching allows for direct comparison of truth and reconstructed particles. The ΔR angle between truth and reconstructed taus and b-quarks respectively, is shown in Figure 5.4. Whereas a comparison between Δp_{T}, $\Delta\eta$ and $\Delta\phi$ of truth and truth matched reconstructed particles are shown in Figure 5.5. The plots show reasonable agreement, but there is a noticeable overestimation of the reconstructed tau transverse momentum compared

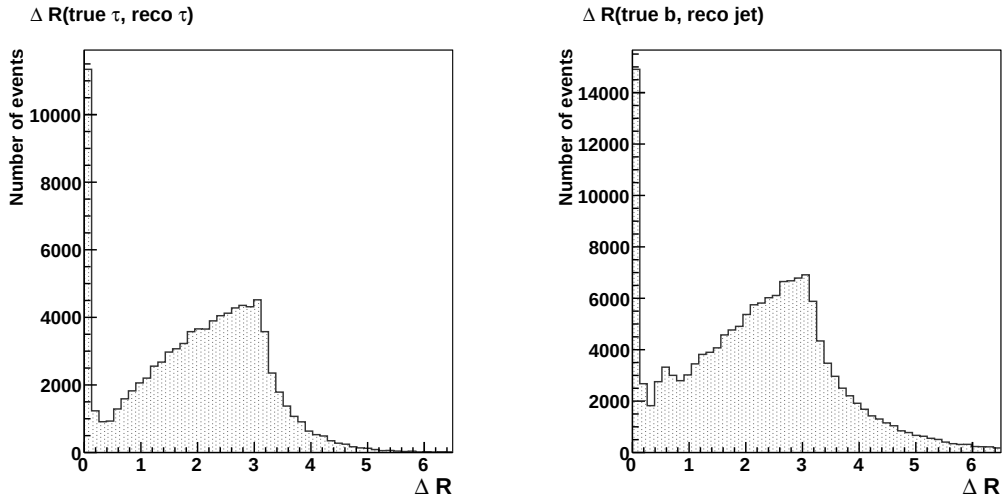

Figure 5.4: ΔR between truth and reconstructed particles - To the left is the ΔR angle between true visible taus and reconstructed taus. To the right is the same plot for true b-quarks and reconstructed jets. Both distributions have "sharkfin" shapes - correct combination of true and reconstructed particle at small angles, and wrong combinations at larger angles.

to the truth information, seen from the tail towards low Δp_{T}-values. This is a know effect of the tau reconstruction algorithms [28].

The tau reconstruction however, provides little rejection against QCD jet background. Rejection comes from a separate identification step, based on simple cuts, boosted decision trees (BDT) or projective likelihood methods. The cut based and BDT methods are further investigated in the following sections.

5.2 Tau Identification

The tau jet has some characteristic features that distinguishes it from a QCD jet:

- A small number of constituent particles
- Narrow jet shape
- Composition of the jet

These properties of the tau jet can be used to separate taus from QCD jets. Seven variables are used to quantify the above characteristics. These are selected to be robust,

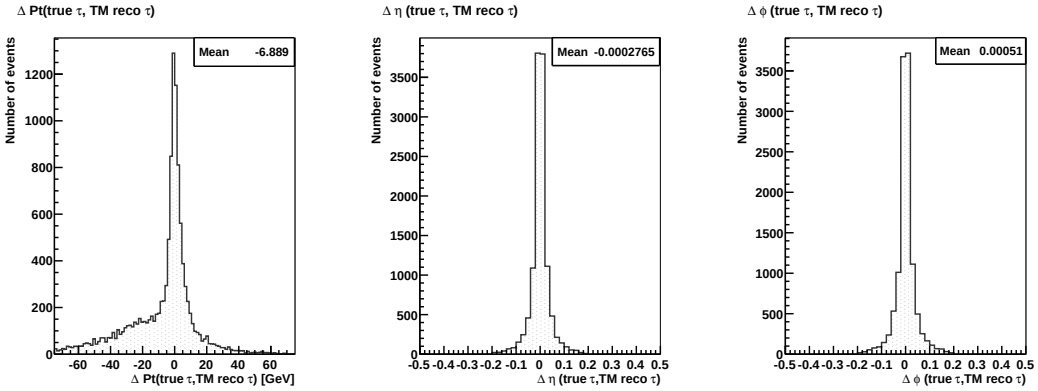

Figure 5.5: Comparison visible truth and truth matched reconstructed taus - Truth - reconstructed variables. Δp_T (left), $\Delta\eta$ (middle), $\Delta\phi$ (right) Notice the asymmetric tail of P_T plot.

i.e. well modelled and understood, in MC and early data. The variables include information from both calorimeter, tracking and the combination of these, and are defined as [31]:

- *Electromagnetic radius:* Transverse energy weighted shower width in the EM calorimeter that takes advantage of tau-jets being narrower than QCD jets:

$$R_{\mathrm{EM}} = \frac{\sum_i^{\Delta R_i<0.4} E_{T,i}^{\mathrm{EM}} \Delta R_i}{\sum_i^{\Delta R_i<0.4} E_{T,i}^{\mathrm{EM}}}, \tag{5.1}$$

  where i runs over cells in the first three layers of the EM calorimeter associated to the tau candidate, ΔR_i is defined relative to the tau jet seed axis and $E_{T,i}^{EM}$ is the cell transverse energy.

- *Track radius:* p_T-weighted track width is the track variable corresponding to EM radius:

$$R_{\mathrm{track}} = \frac{\sum_i^{\Delta R_i<0.2} p_{T,i} \Delta R_i}{\sum_i^{\Delta R_i<0.2} p_{T,i}^{\mathrm{EM}}}, \tag{5.2}$$

  where i runs over all tracks associated to the tau candidate. ΔR_i is defined relative to the tau jet seed axis and $p_{T,i}$ is the track transverse momentum.

- *Leading track momentum fraction:*

$$f_2 trk, 1 = \frac{p_{T,1}^{\mathrm{track}}}{p_T^{\tau}}, \tag{5.3}$$

where $p_{T,1}^{\text{track}}$ is the transverse momentum of the leading track of the tau candidate and p_T^τ is the transverse momentum of the tau candidate. Uses the fact that energy of the leading charged pion is usually higher for taus than it is for QCD jets.

- *Centrality fraction:* Measures the concentration of the energy deposited in the calorimeter relative to the jet axis. Again, tau-jets are more collimated and consequently has higher centrality fraction.

$$F_{\text{core}} = \frac{\sum_i^{\Delta R<0.1} E_{\text{T}i}}{\sum_i^{\Delta R<0.4} E_{\text{T}i}}, \tag{5.4}$$

- *Electromagnetic fraction* Ratio of E_{T} in the EM calorimeter and E_{T} in both the EM and hadronic calorimeter. This variable uses the fact that tau-jets contain neutral pions which decays to photons and are thus detected purely electromagnetically.

$$F_{EM} = \frac{E_{T,EM}}{E_{T,EM} + E_{T,Had}} \tag{5.5}$$

- *Invariant mass of tracks:* Limited by the tau mass for tau-jets but varies with the energy of a QCD jet. Only applicable for taus with more than one track.

$$M_{\text{trk}} = \sqrt{\left(\sum_{tracks} E\right)^2 - \left(\sum_{tracks} \boldsymbol{p}\right)^2} \tag{5.6}$$

- *Invariant mass of the topological clusters of EM calorimeter cells:* As above limited by the tau mass for taus, but varies with energy for QCD jets. Valid for tau candidates with two or more calorimeters clusters.

$$M_{\text{topo}} = \sqrt{\left(\sum_{clusters} E\right)^2 - \left(\sum_{clusters} \boldsymbol{p}\right)^2} \tag{5.7}$$

The distributions for these variables can be seen in Figure 5.6. At higher luminosities however, pile-up will affect distributions for both real and fake tau candidates, thus reducing their separation power. The manner in which these variables are used to perform the identification varies from simple cuts to multivariate techniques like Boosted Decision Trees (BDTs). The performance of these two will be investigated in the following sections.

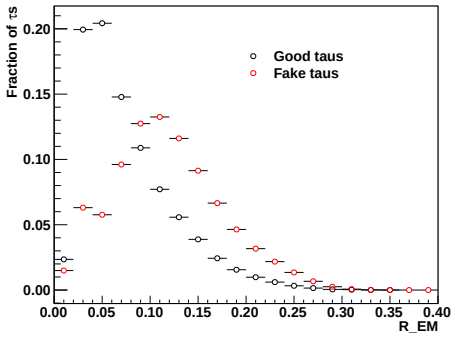

(a) Electromagnetic radius

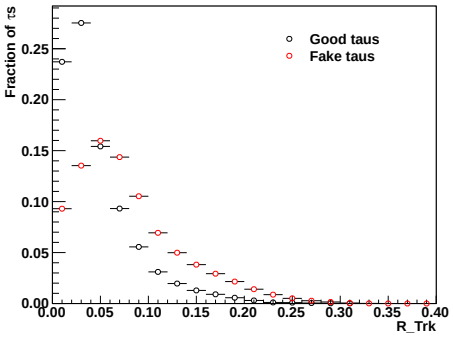

(b) Track radius

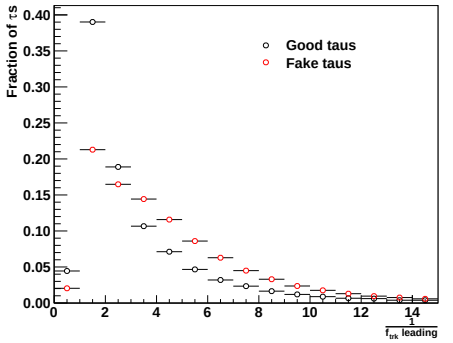

(c) Leading track momentum fraction

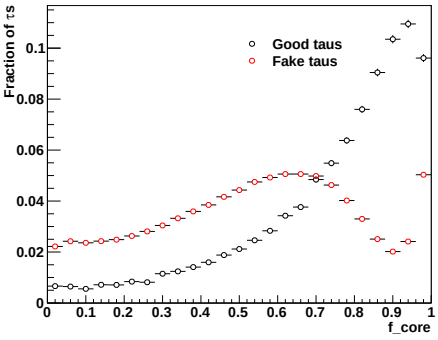

(d) Centrality fraction

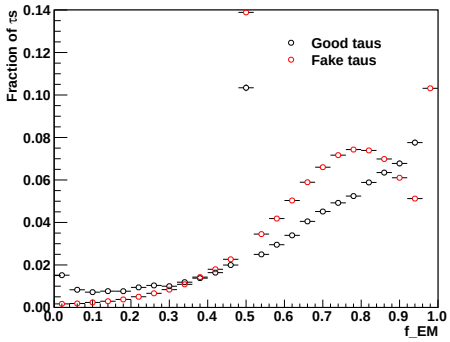

(e) Electromagnetic fraction

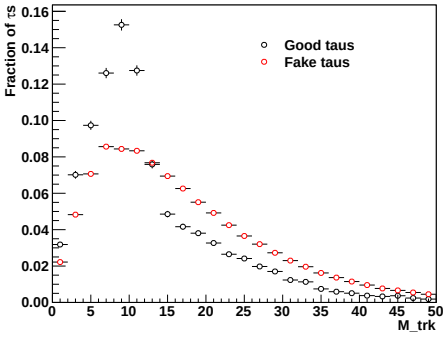

(f) Invariant mass of tracks

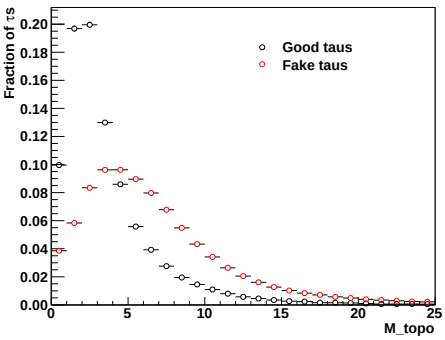

(g) Invariant mass of topo clusters

Figure 5.6: Variables used for tau ID - Black markers (good taus) are truth matched reconstructed tau candidates, red markers (fake taus) are taus without a truth match. Tau candidates from $t\bar{t}$ sample with p_{T}> 15 GeV used.

5.2.1 Cut Based Tau Identification

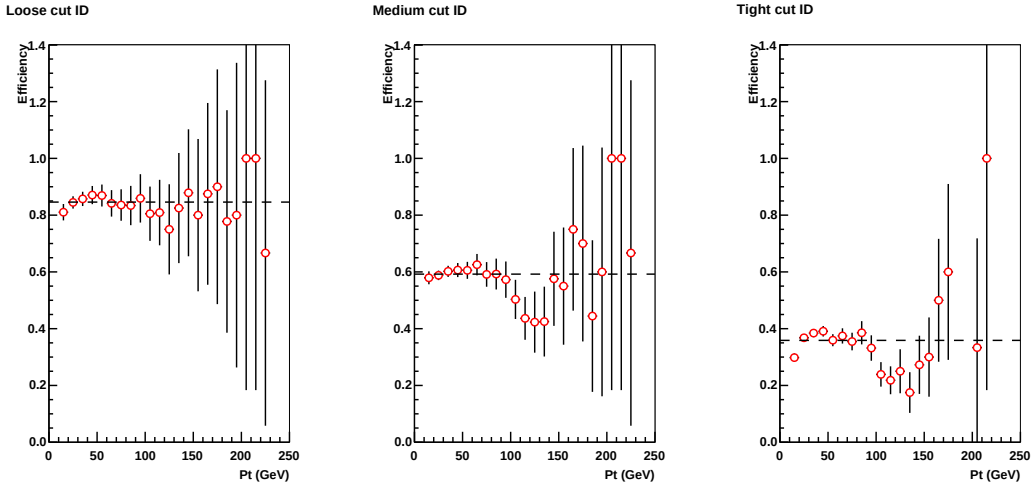

Figure 5.7: Efficiency of tight, medium and loose cut based tau ID against p_t - in a $t\bar{t}$ sample. Note the drop in efficiency for low p_t for all three ID algorithms. The dashed line is the average efficiency.

The cut based ID takes advantage of the characteristics of hadronic tau decays by performing cuts on three of the above variables – jet shape (equations 5.1 and 5.2) and number of constituent particles (Equation 5.3), in order to separate tau jets from QCD jets. The cut based tau ID comes at different levels of accuracy and efficiency of the tau identification depending on how tight cuts are applied to the distinguishing variables. Three categories referred to as tight, medium and loose tau identification are defined. The efficiency of the identification is estimated by:

$$\epsilon_{\text{sig}} = \frac{N^{\tau}_{\text{pass,match}}}{N^{\tau}_{\text{match}}}, \tag{5.8}$$

where N^{τ}_{match} is the number of reconstructed tau candidates that are matched within $\Delta R < 0.2$ of a true, hadronically decaying tau lepton with visible transverse momentum $p_T^{vis} > 15$ GeV and visible pseudorapidity $|\eta^{vis}| < 2.5$. $N^{\tau}_{\text{pass,match}}$ is the number of the above reconstructed candidates that pass the identification criteria. The tight tau identification is shown to have an average efficiency of about 35% of the taus (Figure 5.7) in our $t\bar{t}$ sample. The corresponding numbers for medium and loose tau ID is 60% and 85% in the same sample. These numbers deviate from the targeted signal efficiencies which are 30%, 50% and 70% respectively. This is, however, for $Z \rightarrow \tau\tau$ samples with

$p_{\mathrm{T}}(\tau) > 10$ GeV, which justify the slightly higher values in our $t\bar{t}$ sample and higher p_{T} selection. This is due to the fact that $t\bar{t}$ events contain more final state particles, and the tau ID efficiency is lower for lower p_{T} regions. All the three ID algorithms are found to have decreasing efficiency towards lower p_{T}-values.

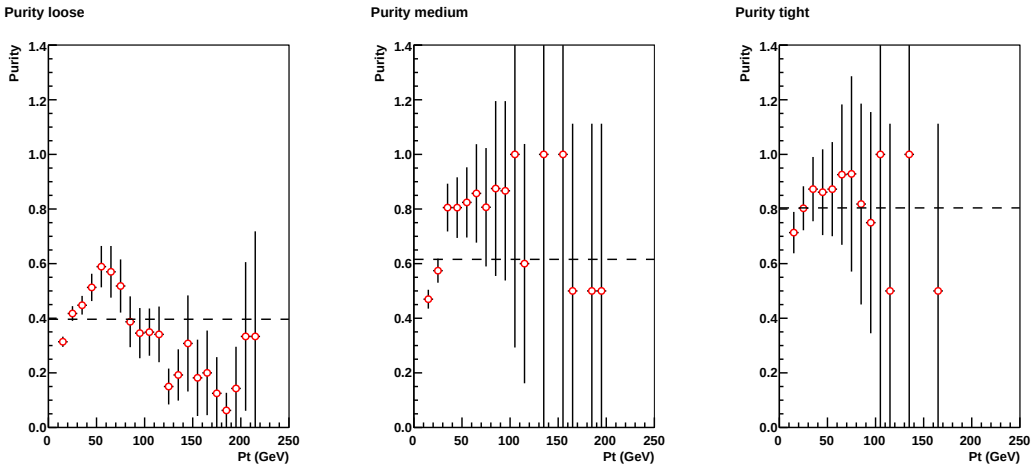

Figure 5.8: Purity of tau reconstruction in $t\bar{t}$ sample - Purity of tight, medium and loose taus for the $t\bar{t}$ events. Dashed line is average purity.

The efficiency however says nothing about the ID purity or its ability to reject background processes. To this end the background efficiency and signal purity is used. The signal purity is defined as

$$p = \frac{N^{\tau}_{\mathrm{pass,matched}}}{N^{\tau}_{\mathrm{pass}}}, \tag{5.9}$$

where N^{τ}_{pass} is the number of reconstructed tau candidates passing the ID criteria. Whereas background efficiency is defined as

$$\epsilon_{\mathrm{bkgd}} = \frac{N^{\mathrm{bkgd}}_{\mathrm{pass}}}{N^{\mathrm{bkgd}}_{\mathrm{total}}}, \tag{5.10}$$

where $N^{\mathrm{bkgd}}_{\mathrm{pass}}$ is the number of the tau candidates that pass the identification criteria, and $N^{\mathrm{bkgd}}_{\mathrm{total}}$ is the number of tau candidates. Another commonly used variable is the background rejection, defined as the inverse of the background efficiency

$$r = \frac{1}{\epsilon_{\mathrm{bkgd}}}. \tag{5.11}$$

The purity of the tight, medium and loose ID in the $t\bar{t}$ sample is found to be on average 80%, 60% and 40% respectively, see Figure 5.8. The background efficiency which indicates the level at which QCD jets are misidentified as tau jets are 1.0%, 2.5% and 6.5% for tight, medium and loose ID in a QCD (J0-J4) sample respectively, see Figure 5.9. In other words, while the tight cut ID is found to have a lower signal efficiency, its purity in the signal sample in addition to the rejection of QCD jets is higher than the two looser IDs.

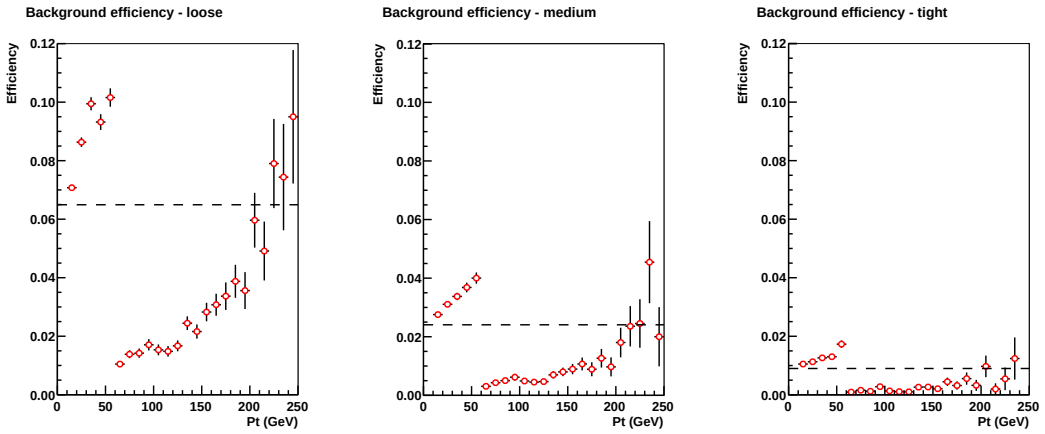

Figure 5.9: Background efficiency - Efficiency of tight, medium and loose taus for QCD events (J0-J4). The dashed line is the average efficiency.

5.2.2 Boosted Decision Trees Tau Identification

The analysis in Chapter 7 makes use of Boosted Decision Tree (BDT) tau identification. This is a multivariate technique (MV) which has a powerful background rejection of QCD jets compared to the cut based tau identifications. Whereas the cut based ID uses simple cuts on three variables, the BDT ID applies more variables and a more sophisticated and elaborate method. The tau candidate is reconstructed in the same way as for cut based ID, whereupon MV techniques are used to determine how tau-like the reconstructed tau candidate is. The BDT ID is applied to calorimeter-seeded and double-seeded candidates, but not to track-seeded candidates. However, variables from both calorimeter and track information as given above are used to produce a single, more powerful, discriminating variable.

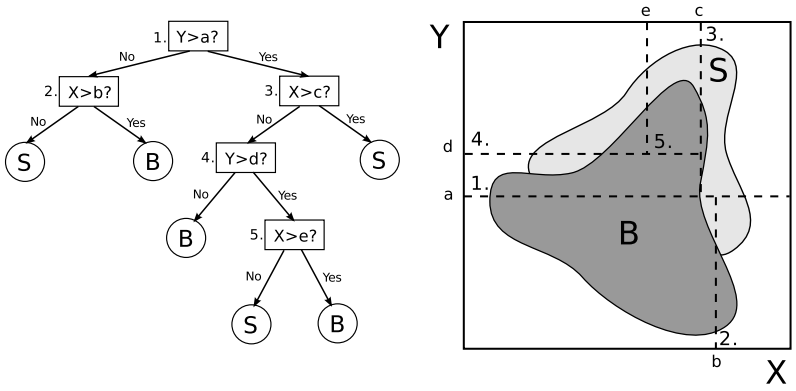

Figure 5.10: Example decision tree training process - Two distributions - signal (S) and background (B) over variables X and Y. Process begins at (1.) by determining the variable and value providing the best possible separation between S and B. Here this is Y at a. Objects with Y $>$ a are passed to the right node and objects with Y $\leq$ a are passed to the left. This process continues recursively until a stopping condition is satisfied, for example a minimum number of objects in a node. Figure taken from [30]

A decision tree defines a recursive sequence of cuts on multiple variables made to separate signal and background. The main advantage of a decision tree over cut-based method is that candidates which fail a single cut are kept and subjected to further investigation of all remaining variables by the algorithm. Whereas for the cut-based ID a candidate failing to pass a cut is immediately discarded, potentially disregarding useful information. The decision tree is trained on signal and background to recognise and separate the two by finding the best cuts on each node as shown in Figure 5.10. This allows one to make a piecewise-continuous cut of an arbitrary shape in the multi-dimensional space defined by the discriminating variables [30]. Averaging is performed over several decision trees in order to make the decision tree stable, against statistical fluctuations in the sample used to create the tree and thus undesirable variations in the output. One such averaging technique is 'boosting'. This yields a single variable expressing tau-likeness of a jet, separating taus from QCD jets. The distribution of this variable, BDT_Jet_Score, clearly shows the separation between real taus and taus from QCD jets as shown in Figure 5.11.

The BDT identification uses seven variables to distinguish taus from jets and electrons, compared to the three used in the cut-based ID. Separate decision trees are made for 1- and 3-prong tau candidates. The most significant improvement in ID performance

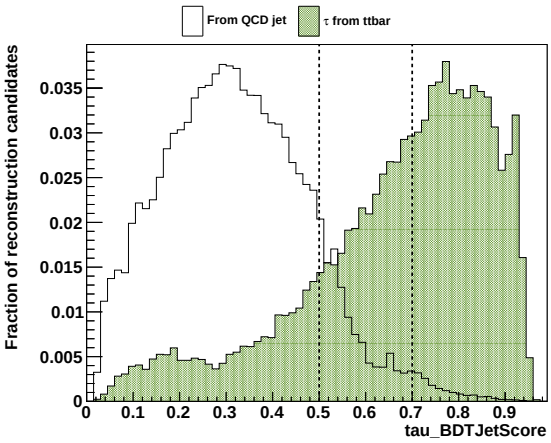

Figure 5.11: Tau BDT jet score - Shows the BDT jet score for taus from $t\bar{t}$ events, filled, and tau reconstruction candidates from a QCD sample, no fill.

for BDT compared to cut-based ID is for the 3-prong candidates, due to the more limited sets of variables used by the cut-based ID. In Figure 5.12 a comparison between BDT and cut based tau identification is shown for BDT > 0.7 and tight cut identification. A clear improvement is observed for both identification efficiency and purity of true taus in $t\bar{t}$ events as well as misidentification of taus from QCD jets. Using the same definitions as above. The efficiency of true tau identification increases on average from about 35% to above 50%, while the rejection factor increased from about 100 to just above 150. Misidentification efficiency of QCD jets decreased almost by a factor of two, from $\sim 1\%$ to $\sim 0.6\%$ (Figure 5.12). This improvement is of prime importance for the discovery and rejection powers of a tau based SUSY analysis. Which to a large extent is limited to the efficiency and purity of tau ID. For taus with BD > 0.5, the signal efficiency is twice as high as for the tight cut ID with an almost equal signal purity. But a decrease of background rejection of almost an order of magnitude is observed.

5.2.3 Additional ID Variables

A comparison between good and fake taus in MC can also be made using truth matching. Good taus are defined as reconstructed taus that have a matching true tau particle, while fake taus are reconstructed particle that do not correspond to a true tau particle. This is usually a QCD jet that has been wrongly reconstructed as a tau. In figures 5.13a and 5.13b the electric charge of good and fake taus are shown for tight and loose

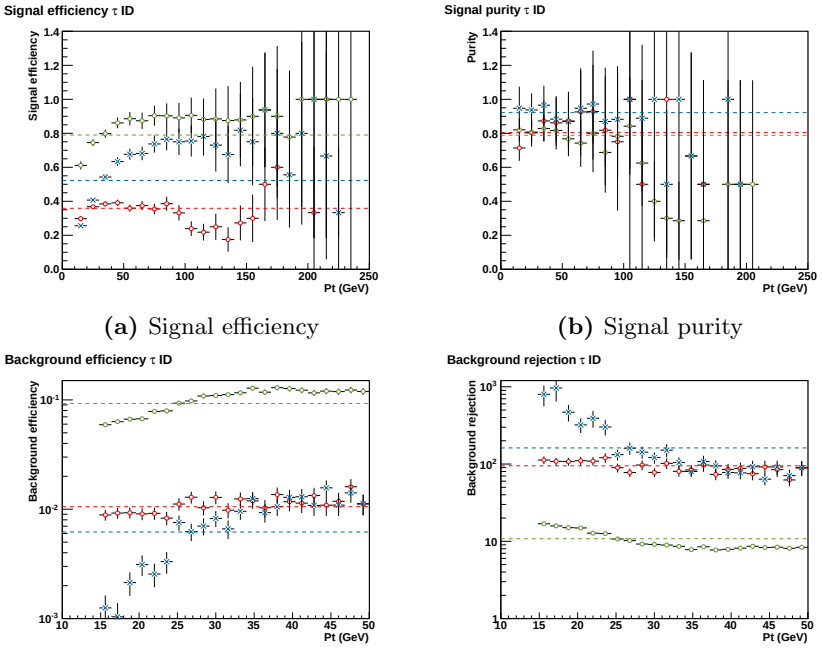

(a) Signal efficiency **(b)** Signal purity

(c) Background efficiency **(d)** Background rejection

Figure 5.12: BDT vs cut ID - Compares BDT and cut based identification of taus in a $t\bar{t}$ sample in a QCD sample versus p_T. Blue crosses are BDT ID > 0.7, green circles are BDT > 0.5, and red crosses are tight cut based ID.

cut-based ID respectively. It is evident that most good taus have charge $\pm$ 1, which means that reconstructed taus with charge zero are more likely not to be real taus. These can consequently be disregarded in the further analysis. From the plot one can also tell that there are smaller deviations between the tight good and fake taus than for loose taus. This is expected since these reject a larger number of QCD jets by applying stricter ID conditions on the reconstructed taus. As true taus decay to one, three or five charged particles it is expected that the good taus should consist of mainly these numbers of prongs. However there is no such preference for an odd number of prongs for QCD jets, and mis-reconstructed QCD jets should have a more even distribution of prongs. These assumptions are all supported by figures 5.13f and 5.13e.

Figures 5.13d and 5.13c shows the author number of good and fake taus for loose and tight tau ID respectively. It is clear that author number 3, which means both calorimeter and track seeded taus, yields a smaller fraction of fake taus. Tau candidates with only a track seed, author = 2, do not pass the cut ID, and are consequently not shown in the figure.

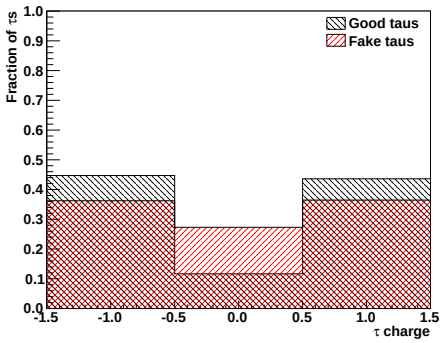

(a) Tight ID - charge

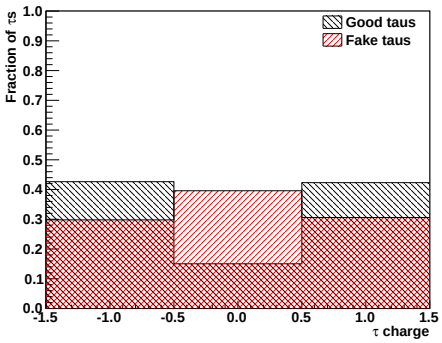

(b) Loose ID - charge

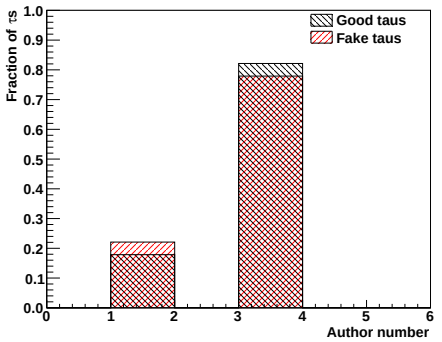

(c) Tight ID - author

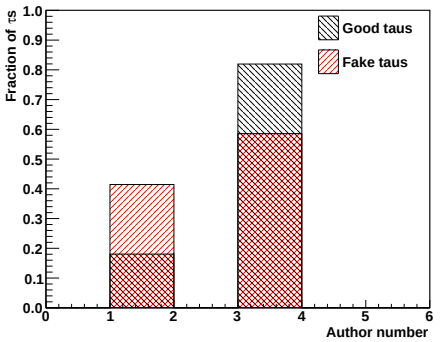

(d) Loose ID - author

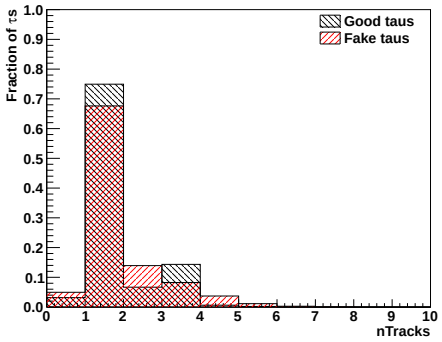

(e) Tight ID - nTracks

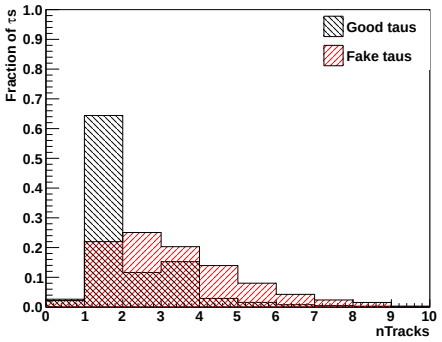

(f) Loose ID - nTracks

Figure 5.13: Additional tau ID variables for tight and loose tau identification. Good taus are truth matched reconstructed taus, while fake are without truth matches.

6

First Look at Top-pair Events

This chapter will examine top quark pair events produced by MC simulations. This is done to obtain a thorough understanding of such events, i.e. the kinematics as well as the relationship between truth and reconstructed information of the measured variables. This understanding is vital to reject $t\bar{t}$ background while keeping a potential SUSY signal both in simulations and in the final analysis using data. To properly understand the kinematics of the event, the top mass was reconstructed using the collinear approximation (CA) as well as the reduced top mass.

6.1 The Top Quark

The top quark was predicted already a few decades before first discovered at Tevatron in 1995. Despite being discovered over 15 years ago, the top still plays an important role both theoretically and experimentally in high energy physics. Still many characteristics of the top remain little studied. This includes production mechanisms, production cross section, existence of resonance structure or anomalous couplings, as well as properties of the top mass, width, spin, charge and couplings.

With its large luminosity and center-of-mass (CoM) energy the LHC is a top factory. Due to this large center-of-mass energy it is expected to yield a $t\bar{t}$ production cross section of 833 pb, which is about a factor 100 larger than at Tevatron. The design luminosity at the LHC is also larger than that at Tevatron by the same factor. This corresponds to production of a top pair every second, compared to Tevatron's 10 pairs per day. The production mechanism of top pairs also differ between Tevatron and the

LHC due to the different CoM energies. At the LHC gluon-gluon fusion dominates, in contrast to Tevatrons quark-antiquark annihilation dominated production [24].

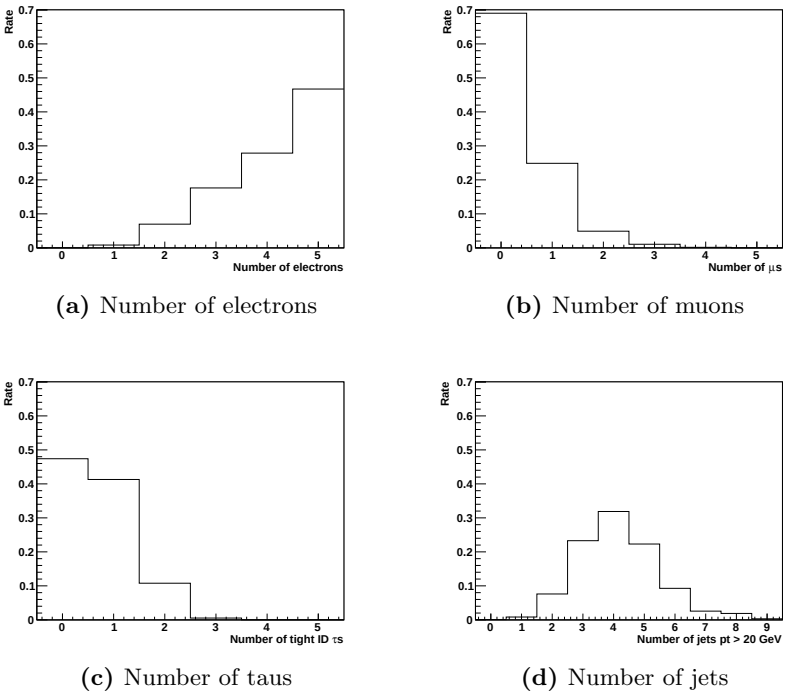

(a) Number of electrons

(b) Number of muons

(c) Number of taus

(d) Number of jets

Figure 6.1: Number of reconstructed particles - electrons, muons, taus with tight cut ID, and jets with $p_{\mathrm{T}}>$ 20 GeV in $t\bar{t}$ events with both taus decaying hadronically.

The top quark almost always decays to a W boson and a b-quark. Where in turn the b-quark will hadronise and produce a jet, called a b-jet since it originates from a b-quark. The W on the other hand has several possible decay channels. It can either decay into two lighter quarks each hadronising and forming jets, or into a lepton and a neutrino of the same flavour as the lepton. The decay of W to a tau neutrino and tau lepton is of particular interest to this study. This study will focus on hadronic tau decays. This is due to the fact that leptons originating from a tau decay are often impossible to distinguish from primary electrons or muons in a collision. Therefore the decay chain of interest is:

$$t\bar{t} \rightarrow WWb\bar{b} \rightarrow (\tau^{+}_{\mathrm{had}}\nu_{\tau})(\tau^{-}_{\mathrm{had}}\bar{\nu}_{\tau})b\bar{b} \tag{6.1}$$

6.2 MC Simulated $t\bar{t}$ Events

Some general properties of these events are immediately clear from the above decay chain . In total we should observe four high energy jets, two of them being narrow tau-jets and the other two b-jets. Also, a large amount of missing energy ($E_{\mathrm{T}}^{\mathrm{miss}}$) is expected as the neutrinos from both the W and tau decays escape detection. Missing energy information is only available in the transverse plane, as momentum conservation in the longitudinal direction is inapplicable since the initial longitudinal momentum of the colliding partons is not known. Additionally, particles may also escape undetected down the beam pipe. $E_{\mathrm{T}}^{\mathrm{miss}}$ is reconstructed from the transverse energy imbalance in the calorimeters assuming momentum conservation in the transverse plane. However as shown in Figure 6.1, the reconstructed particles in an event described by the decay chain in Equation 6.1 is not only limited to the particles in this decay chain. There are often additional jets and light leptons. Also, both taus are not always reconstructed, while in some cases three taus, where at least one is a fake tau, are reconstructed and pass the tight cut based ID.

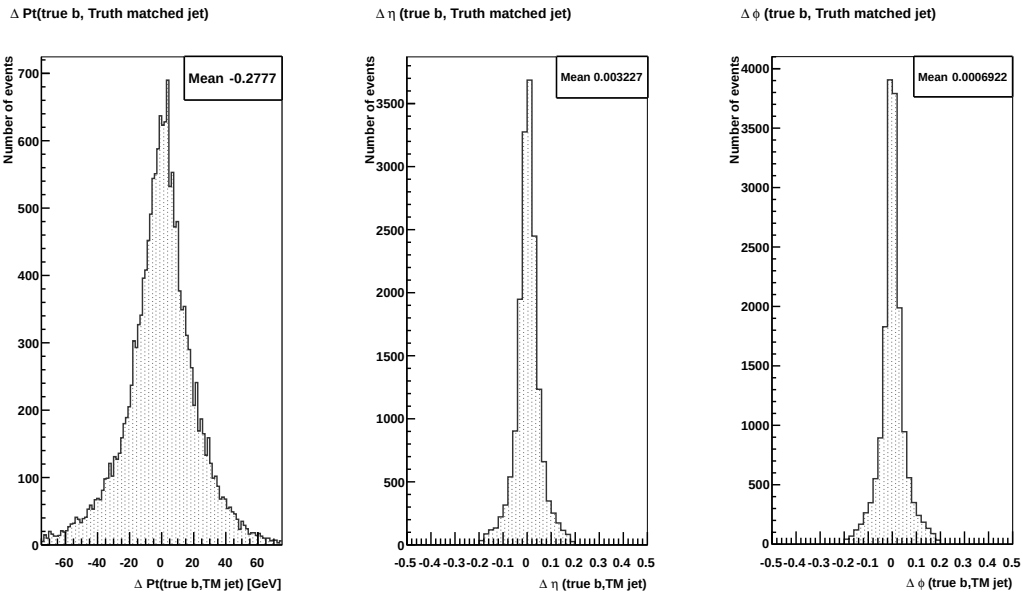

Figure 6.2: Comparison between true b-quark and reconstructed jet - Δp_{T}, $\Delta\eta$ and $\Delta\phi$ between true b-quark and the corresponding truth matched reconstructed jet.

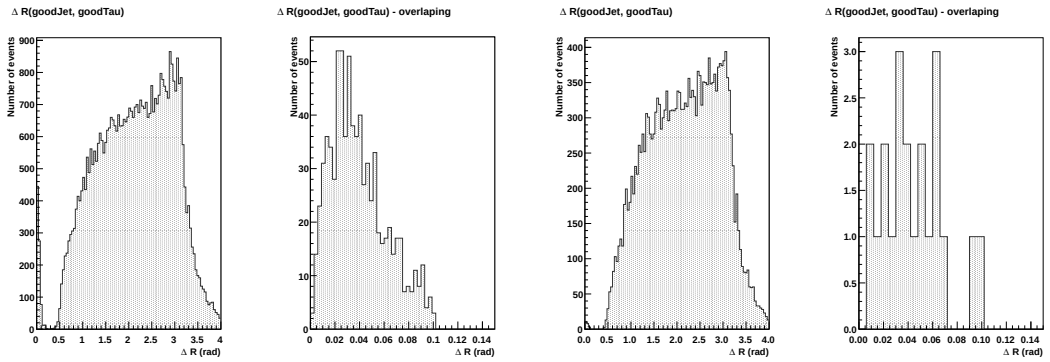

(a) Loose tau reconstruction **(b)** Tight tau reconstruction

Figure 6.3: Overlap in ΔR - between reconstructed jets and taus in $t\bar{t}$ events. Left plots show ΔR, right shows the same distribution for $0 < \Delta R < 0.15$.

To identify taus and jets actually coming from a $t\bar{t}$ event truth-matching is again applied. Truth matching true b-quarks with reconstructed jets allows a comparison between the true quark and reconstructed jet characteristics, see Figure 6.2, where Δp_{T}, $\Delta\eta$ and $\Delta\phi$ are shown. The discrepancies are seen to be reasonably small, with no significant asymmetry in the reconstructed values. Misidentification of jets as tau jets could lead a single object, a jet or a tau, to be reconstructed as two different objects, a jet and a tau jet. To make sure that one does not select taus and jets that are reconstructed from the same object one can look for overlap between reconstructed taus and jets in an event by investigating ΔR(jet, tau). From Figur 6.3 it is clear that the amount of overlap between taus and jets is small in $t\bar{t}$ events, although it is as expected more significant with a loose tau identification.

Following the arguments for how some key parameters of real taus should look like from Chapter 5, quality criteria on the tau selected for use in the analysis may be applied. The number of events satisfying these requirements for the $t\bar{t}$ and QCD (J0-J4) sample can be seen in Table 6.1. The quality criteria applied are the following:

- Taus reconstructed from both calorimeter and track seed – author = 3.
- Charge of tau is ± 1.
- Number of tracks is 1 or 3.
- Avoid taus in crack region between barrel and end-cap – $|\eta| < 1.3$ and $1.7 < |\eta| < 2.4$.

The tau ID efficiency following from these quality criteria is shown in Figure 6.4. A average efficiency of 30% is obtained for taus from the $t\bar{t}$ sample. This efficiency is almost independent of transverse momentum, but has a decrease towards low transverse tau momenta. The η dependence is also very small, although there is a slight decrease for increasing $|\eta|$ values.

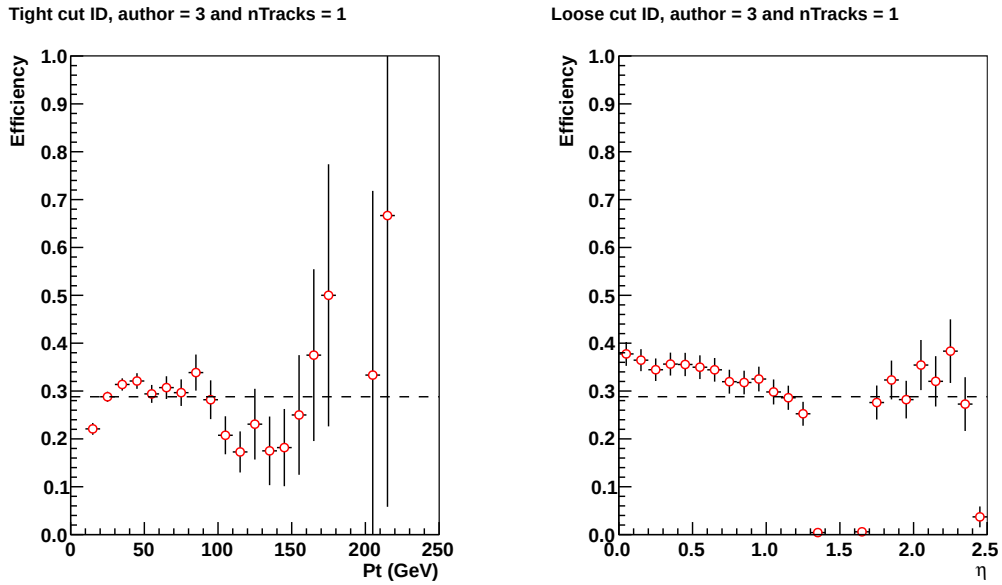

Figure 6.4: Tau quality criteria efficiency - Tau identification efficiency against p_{T} and η for taus with |charge| = $\pm$1, nTracks = 1 or 3, author = 3, tight cut identification and not in the crack region.

Figure 6.5 shows p_{T}, p_Z, ΔR and $\Delta\phi$ of true top quark pairs calculated from truth particles including truth neutrinos. The same distributions using truth matched reconstructed variables without neutrino or missing energy information is shown in Figure 6.6. A significant smearing compared to the true distribution, due to the lack of information about the neutrinos is observed. By finding a way to retrieve some of the information that is lost through the escaping neutrinos the distributions in Figure 6.6 can hopefully be improved up on to closer resemble those seen in Figure 6.5. This, along with a measurement of the top quark mass is the aim of the following section.

Number of events	$t\bar{t}$	%	**QCD**	%
Total	1327	-	78 959	-
Both seeds	1313	98.9	39790	50.4
Charge ± 1	1201	91.5	25907	65.1
$\eta < 1.3$ or $1.7 < \eta < 2.5$	1137	94.7	22149	85.5
2 reconstructed taus	889	78.2	8780	39.6
2 medium cut ID taus	196	22.0	17	0.2
2 tight cut ID taus	58	29.6	2	11.8

Table 6.1: Tau selection criteria - $t\bar{t}$ and QCD (J0-J4) - Number of events after cumulative selections on reconstructed taus. % is the percent of events left with respect to the previous selection criteria.

6.3 The Top Quark Mass

The top mass has been measured to 172 ± 0.9 ± 1.3 GeV [7]. Measuring the top mass is valuable in its own right, but it may also be an important tool to separate top signals from backgrounds from different initial particles or processes that share a similar or identical final state topology. If the final state particles originate from particles of different masses, the invariant mass of these final state products should also be different. This should result in a rather narrow invariant mass distribution around the top mass for signal events, clearly distinguishable from a broader and less peaked background distribution. The narrower the signal distribution is, the easier it is to separate from the background, as the signal significance increases. However, measuring the mass of top quarks decaying into tau leptons is not a straight forward task, due to the energy carried away by neutrinos that are not registered in the detector.

In principle the mass of the top quark may be measured if one knows the energy and momentum of all the decay products of the top

$$M = \sqrt{\sum_i^n p_i^2} = \sqrt{\sum_i {E_i}^2 - \sum_i {\boldsymbol{p}_i}^2}, \tag{6.2}$$

where p_i is the energy-momentum four vector, E_i is the energy and $\boldsymbol{p}_i$ is the three-momenta of particle i in the top decay. However, this decay contains four neutrinos, and as mentioned above, the only measured information on neutrinos is missing transverse energy, as all neutrinos escape detection. For certain final state topologies the missing

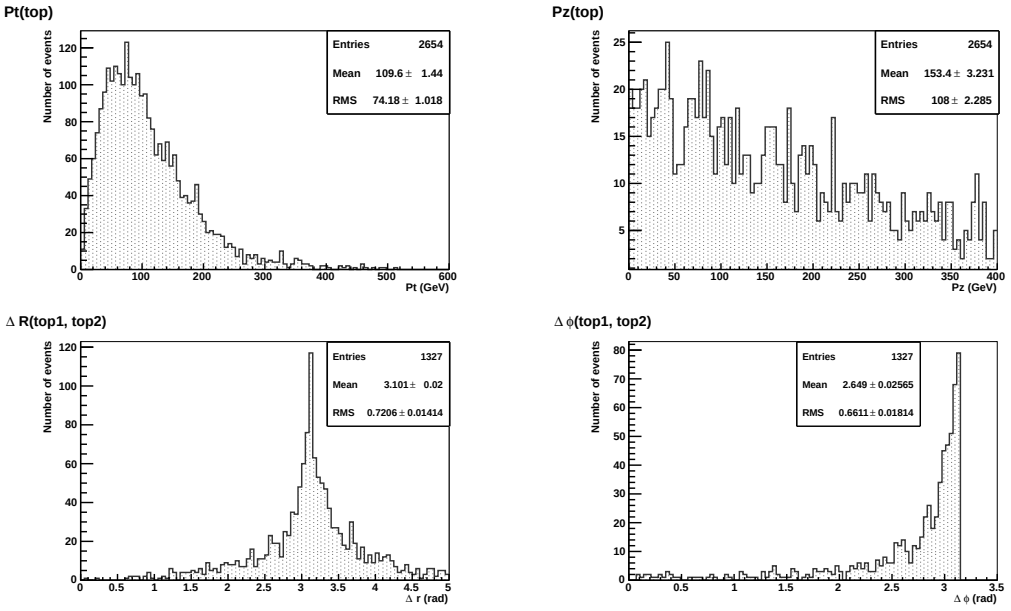

Figure 6.5: True top quark kinematics - p_{T}, p_Z, ΔR and $\Delta\phi$ of true top quarks.

energy associated with the neutrinos partially cancel out. This effect is less pronounced for four rather than two neutrinos, where two back to back neutrinos would more or less cancel out depending on their momenta. In other words there is no available information on the longitudinal components of neutrinos, or individual neutrinos in the transverse plane, only the transverse vector sum off all the neutrinos in an event. These factors make it impossible to reconstruct the invariant top mass directly from missing energy and the visible final state decay products. There exist several methods to partially reconstruct the top invariant mass from missing energy and visible decay products. One of these is the Collinear Approximation (CA), which aims to partially reconstruct the momentum of the neutrinos from the missing energy. Another and simpler method is the reduced mass, which uses the missing energy information directly. These two methods will be investigated further in the following sections.

6.3.1 The Collinear Approximation

The collinear approximation, first proposed in [32], is a frequently used method to reconstruct invariant masses without neglecting the missing information caused by the neutrinos. It is based on two main assumptions [33]:

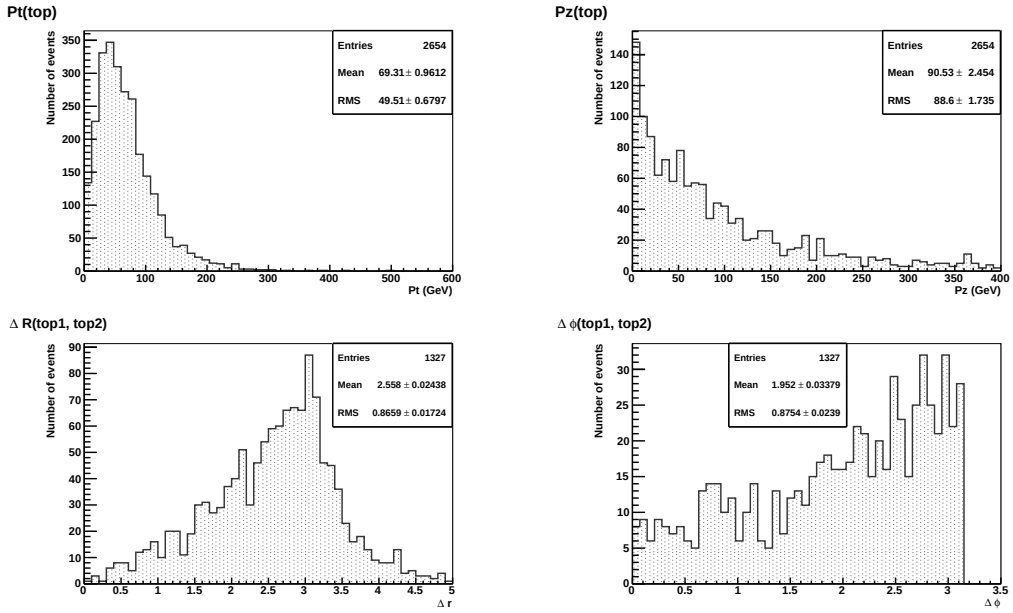

Figure 6.6: Truth matched reconstructed top quark kinematics - p_{T}, p_Z, ΔR and $\Delta\phi$ of truth matched reconstructed top quarks. Not including neutrino or missing energy information.

1. Tau neutrinos in the event are nearly collinear with the visible tau in the same decay chain — i.e. $\phi_\nu \approx \phi_\tau$ & $\eta_\nu \approx \eta_\tau$

2. $E_{\mathrm{T}}^{\mathrm{miss}}$ in the event is only due to neutrinos.

When these assumptions hold this method allows the momentum carried away by the neutrinos in an event to be calculated by solving [33]:

$$\begin{aligned} E_x^{\mathrm{miss}} &= p_{\mathrm{mis}_1} \sin\theta_{\mathrm{vis}_1} \cos\phi_{\mathrm{vis}_1} + p_{\mathrm{mis}_2} \sin\theta_{\mathrm{vis}_2} \cos\phi_{\mathrm{vis}_2} \\ E_y^{\mathrm{miss}} &= p_{\mathrm{mis}_1} \sin\theta_{\mathrm{vis}_1} \sin\phi_{\mathrm{vis}_1} + p_{\mathrm{mis}_2} \sin\theta_{\mathrm{vis}_2} \sin\phi_{\mathrm{vis}_2} \end{aligned} \tag{6.3}$$

where ${E_{\mathrm{T}}^{\mathrm{miss}}}_x$ and ${E_{\mathrm{T}}^{\mathrm{miss}}}_y$ are the x- and y-components of the $E_{\mathrm{T}}^{\mathrm{miss}}$ vector, p_{mis_1} and p_{mis_2} are the combined invisible momenta from neutrinos, for each top quark decay chain. While $\theta_{\mathrm{vis}_1,2}$ and $\phi_{\mathrm{vis}_1,2}$ are the polar and azimuthal angles of the visible taus in each top decay chain.

Using CA on top quark pairs decaying into two taus differs from the situations in which CA is most commonly used. Which is for $\tau\tau$ systems where there are only neutrinos from tau decays. In this case the main problem is dealing with back-to-back

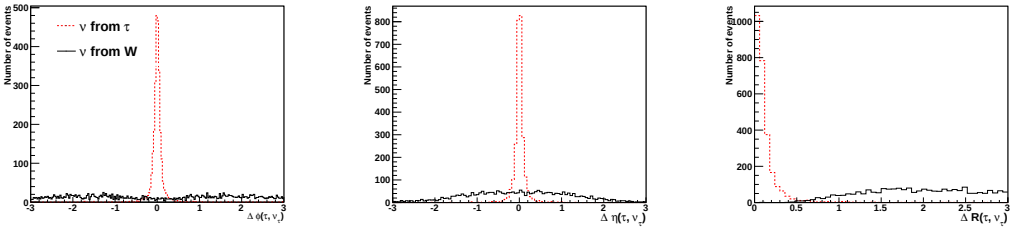

(a) $\Delta\phi$ **(b)** $\Delta\eta$ **(c)** ΔR

Figure 6.7: First assumption of CA - Black line is for ν from W decay, red dotted line is for ν from τ decay.

taus in the transverse plane, where $\phi_{\text{vis}_1} = \phi_{\text{vis}_2} + \pi$. This leads the above equations to become degenerate, and solutions $p_{\text{mis}_{1,2}}$ diverge as $|\phi_{\text{vis}_1} - \phi_{\text{vis}_2}| \to \pi$. This means that the mass is only properly reconstructed for the cases where the $\tau\tau$ system is boosted. While near back-to-back topologies yield a high mass tail, due to the above mentioned divergence [33]. The above equations are also impossible to solve when the missing energy direction does not lie in the plane spanned by the two visible taus in the transverse plane. Again, this results in a loss of some of the statistical power of the method.

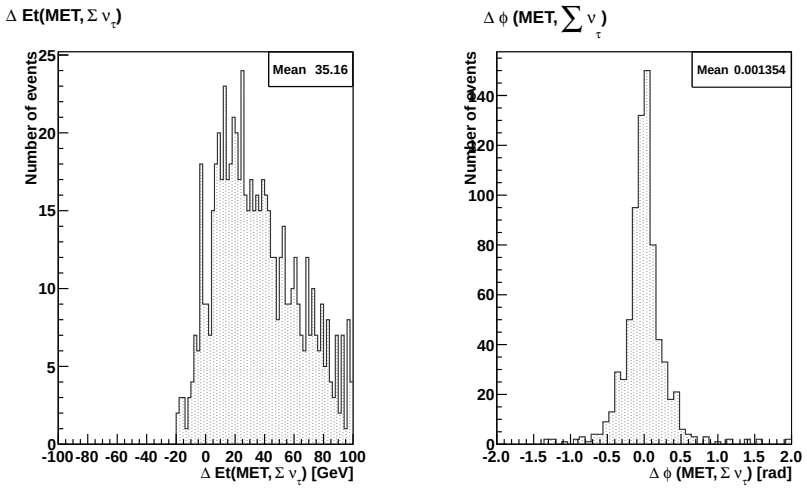

Figure 6.8: Δ ($E_{\text{T}}^{\text{miss}}$, Σ ν) - Comparison between $E_{\text{T}}^{\text{miss}}$ and E_T of the transverse vector sum of tau neutrinos.

However in our case we have two neutrinos from each top decay chain, where both neutrinos are from different decays in the chain. There is one neutrino from the decay of the tau, and a neutrino from the decay of a W boson. This means that it is two steps in the decay chain separating the neutrino from the W-decay and the visible tau. One would therefore expect there to be less angular correlation between this neutrino and the tau, than between the tau and neutrino from the tau decay, as confirmed by Figure 6.7. Which in turn means that first condition of CA holds for a smaller fraction of events with this topology, leading to a poorer mass reconstruction. However, the rather long decay chain before reaching the visible tau would again suggest that there is less of a problem with back-to-back topology of the two visible taus. On the other hand since there is less correlation between the neutrinos from W decays and the visible taus there should be more cases where the CA breaks down due to the direction of the $E_{\mathrm{T}}^{\mathrm{miss}}$. As this would be more randomly oriented, and thus less likely to lie in between the two visible taus. A comparison of the reconstructed missing energy in an event and the vector sum of the four neutrinos in the transverse plane show significant differences especially in transverse energy, and to a lesser extent the direction of the missing energy (Figure 6.8). This will contribute towards a reduced reconstruction quality of the method.

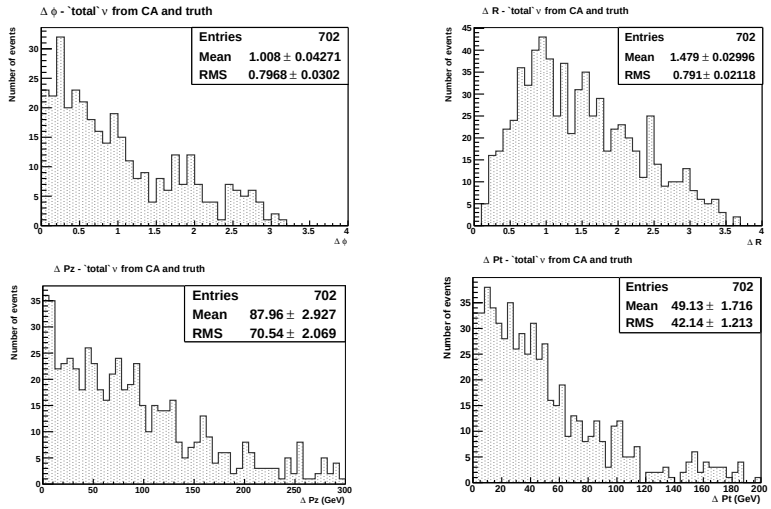

Figure 6.9: $|\Delta(\nu_{true}, \nu_{CA})|$ - $\Delta\phi$, ΔR, Δp_Z and Δp_{T} of the sum of true neutrinos and neutrinos from CA in event.

Using truth particles originating from $t\bar{t}$ events with two hadronic taus the the collinear approximation was applied to make two effective neutrinos along the direction of the visible true taus using the sum of neutrinos transverse energy. $\Delta\phi$, ΔR, Δp_Z and Δp_{T} between the sum of true neutrinos in the event and the the sum of the 'neutrinos' obtained using CA is shown in Figure 6.9. Relatively large deviations between the two with regards to direction and momentum is observed, indicating that the CA is not able to reconstruct the neutrinos properly for a large number of events.

By combining the two neutrinos obtained from the collinear approximation with truth matched reconstructed particles in our signal events we obtain top quarks with p_{T}, p_Z, ΔR and $\Delta\phi$ as seen in Figure 6.10. It is clear that we loose a large number of events compared to what we started out with in Figure 6.5. Roughly 25% of the total truth events in Figure 6.5 are left. There is however a significant improvement in the quality of reconstruction of the tops compared to the same figures without taking into account the neutrino information, as seen in Figure 6.6.

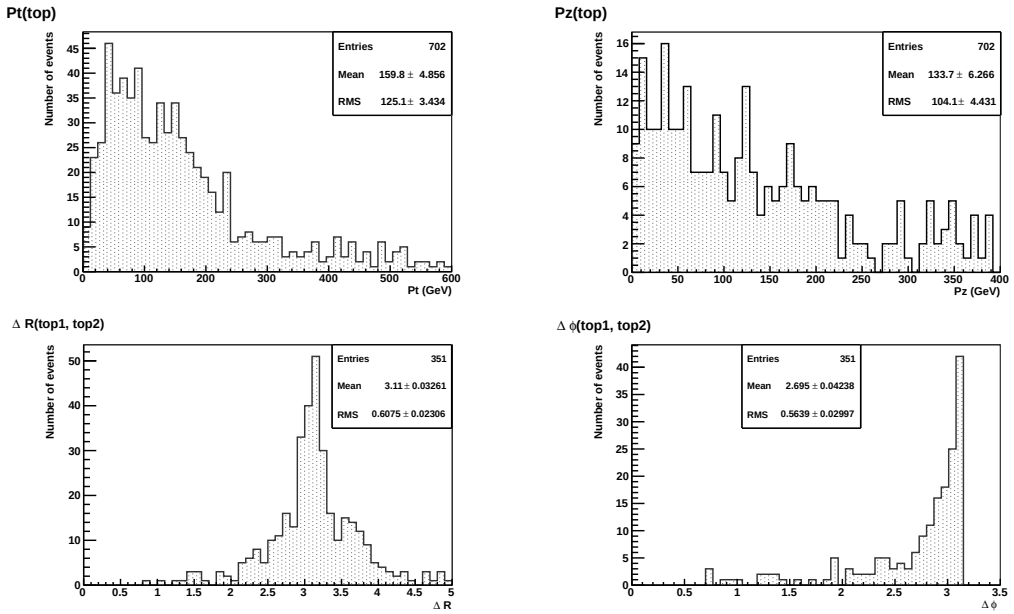

Figure 6.10: Truth matched reco tops using CA - Kinematics of tops reconstructed using truth matched reconstructed particles and CA to reconstruct neutrinos.

In the ideal case, using true b-quarks and taus, in addition to missing energy found from the sum of true neutrinos, the top mass can be reconstructed using the collinear

approximation. The result is shown in Figure 6.11a and for truth matched reconstructed particles in Figure 6.11b. The distributions have means at about 139 and 134 GeV respectively. Making a Gaussian binned fit to the peak of the distributions peak values of 130.5±3.6 and 120.5±8.0 are found, with a $\frac{\chi^2}{ndof}$ of 0.55 and 0.87, respectively. About half of the events are lost using CA for the truth particles, and about 90% for truth matched reconstructed particles. There is no major difference observed between combining correct and wrong combinations of tau and b either, although a smearing and flattening of the peak is observed. This suggests that the reconstructed neutrino momentum from CA dominates over the visible particle momenta. The characteristic CA high mass tail is also seen.

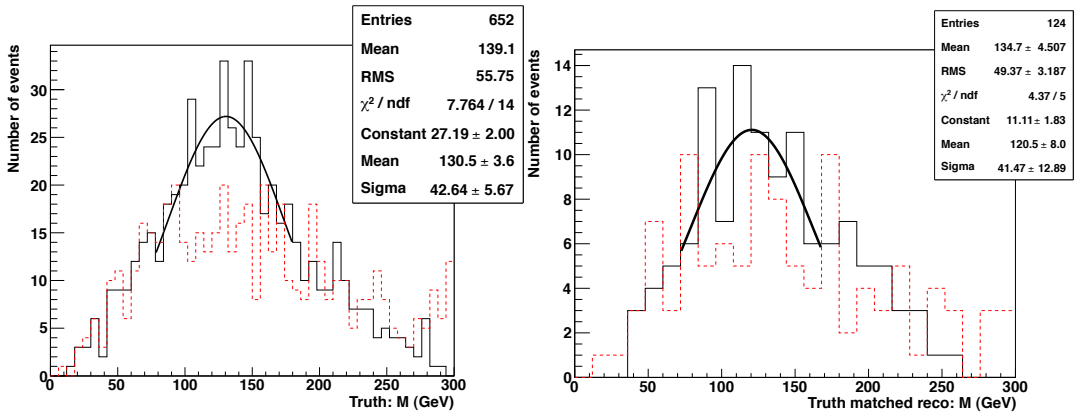

(a) Truth particles **(b)** Truth matched reconstructed particles

Figure 6.11: CA reconstructed top mass - CA used to reconstruct missing neutrino momentum. The black line is correct combinations of τ and b, while the red dotted line is for wrong combinations.

When only looking at reconstructed variables without relying on any truth information, as is the more realistic scenario faced in a data analysis, one still needs to be able to combine the tau and b/jet from the same decay chain. One hoped to do this by using an angular matching of the tau and b-quark, where the tau and b-quark closest together are assumed to have originated from the same top quark. However, as shown in Figure 6.12, there is no significant angular difference between right and wrong combinations of these two particles. This is due to there being two steps in each decay chain separating the visible tau and b, thus removing most of the original angular correlation between them. The amount of angular correlation also depends on

the boost of the top quark, where larger boost yield more collimated decay products and consequently a larger degree of angular correlation. One solution to this matching problem is selecting the tau and b combination that yields the smallest mass difference between the two tops in an event. This is motivated from the fact that in the ideal case the invariant mass of the two tops should be identical. Thus it is more likely that the combination that gives the smallest mass difference is the correct one. Figure 6.13 shows a clear improvement in the mass peak when selecting this combination relative to all possible combinations of tau and b quark, supporting this assumption.

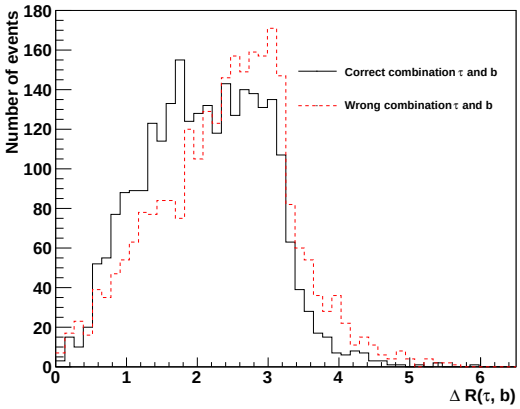

Figure 6.12: $\Delta R(\tau_{vis}, b)$ - Angle ΔR between correct (black) and wrong (red) combination of tau and b-quark in top-pair event.

Matching is however not the only challenge when dealing with reconstructed data, on also needs to make a selection of taus and jets. Ideally one would like to select two tight taus with opposite sign as these are most likely to be real taus from a top pair. However only a small fraction of events fulfil these requirements, see Table 6.1. A selection on which taus to use is a trade-off between the purity and efficiency of the selection. A selection using events with at least one tau with tight cut ID is used (top) for producing the results shown in Figure 6.13. If there is only one tight tau, the tau with the highest p_{T}, the leading tau, will be selected as the second tau. This is still only a small fraction of the total number of taus available. When considering a process as background rejection tool, a high efficiency is important. In this case the best tau pair available could be used as the lower plots in Figure 6.13 show. Here two tight taus, one tight and p_{T}-leading or p_{T}-leading and p_{T}-next leading tau are used depending on

what is available in the event. This clearly yields better statistics, but also yields a broader mass distribution, thus reducing sensitivity. A peak towards low mass values is also observed, which is probably due to misidentified taus. A rough Gaussian fit has been made to the two top mass distributions with a peak at 162 ± 8, and $\sigma = 68 \pm 6$ ($\frac{\chi}{ndof} = \frac{10.08}{10}$ and fit range 40-320 GeV) for events with at least one tight tau, and mean of 180 ± 10 with $\sigma = 100 \pm 13$ for the best available taus ($\frac{\chi}{ndof} = \frac{9.86}{11}$ and fit range 50-300 GeV).

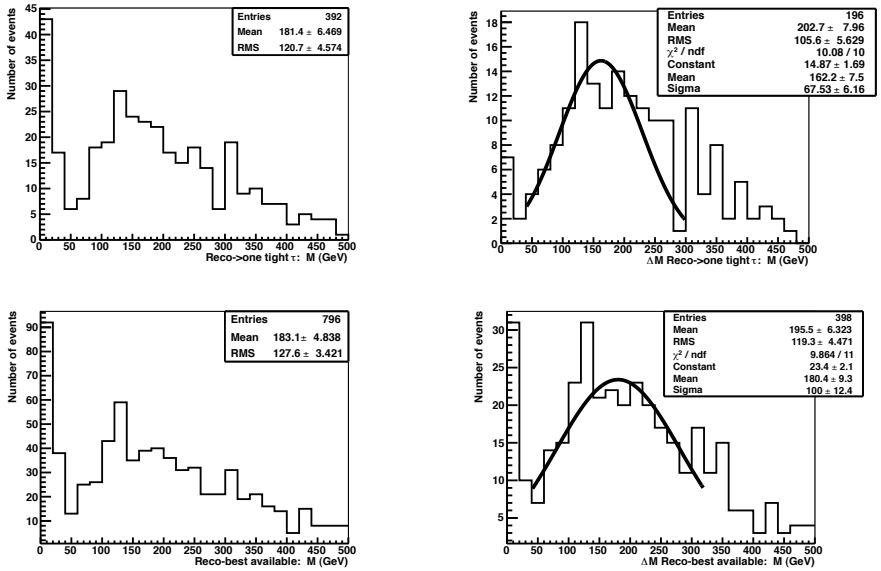

Figure 6.13: CA M(top) reco only - Left: All possible combinations of tau and b. Right: Combination of τ and b that yields smallest mass difference between the two tops with rough Gaussian fit. Top row: Events with at least one tight tau. Bottom: Best taus available in event.

6.3.2 Reduced Mass

A simpler and frequently used quantity is the reduced invariant mass reconstruction. This variable calculates the invariant mass from all visible four momenta with or without including missing energy information. If missing energy is also included it is called transverse mass. The missing energy is added to the invariant mass calculation like any other four vector, with the $E_{\mathrm{T}}^{\mathrm{miss}}$ four vector described as

$$p_{E_{\mathrm{T}}^{\mathrm{miss}}} = (E_{\mathrm{T}}^{\mathrm{miss}}, E_x^{\mathrm{miss}}, E_y^{\mathrm{miss}}, 0)$$

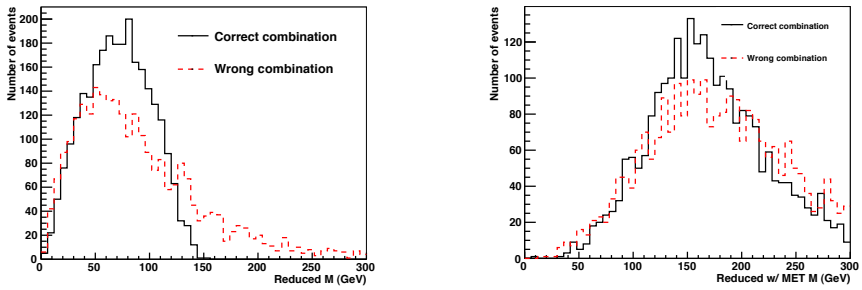

Figure 6.14: Truth: Reduced and transverse mass - Reduced and transverse top mass using truth variables. Black indicates correct combination of tau and b, while dotted red lines means wrong combination.

A major advantage of the reduced mass compared to CA is that is can be defined for all events thus preserving statistical power. However not fully accounting for neutrinos momenta biases the distribution towards lower values. There are larger difference in the distributions for right and wrong combinations of tau and b-quarks/jets of tau and b (black line), and wrong combinations (red dashed line). Compared to the collinear approximation the reduced mass naturally yields a lower mass peak value, as expected since this is not the full invariant mass of the top. However the peak is narrower than for CA, and there is no loss of statistics as there is with CA. The transverse mass distribution is broader with a tail towards high mass values. The difference between the correct and wrong combinations of tau and b-quark is very small, indicating that the missing energy term is dominating the mass distribution.

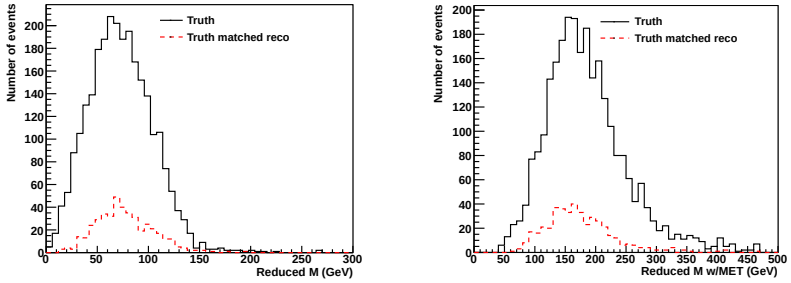

Figure 6.15: Truth reduced mass with smallest ΔM(top) selection - Reduced and transverse mass of the combinations of tau and b that yields the smallest mass difference between the two tops in the event. The black line is truth, while the red is truth matched reconstructed particles.

Support for selecting the combination of tau and b that yields the lowest top mass difference is obtained from Figure 6.15. It is clear that using this matching technique almost gives the same mass distribution as for true truth combinations. The relatively small fraction of tops reconstructed using truth matched reconstructed particles compared to the true number of top events is also seen. In Figure 6.16 the same masses are shown for truth matched reconstructed variables. It shows the same characteristics as seen in Figure 6.14. The loss in statistics for the truth matched reconstructed particles is due to the true particles failing to be reconstructed or being identified as taus with our additional criteria.

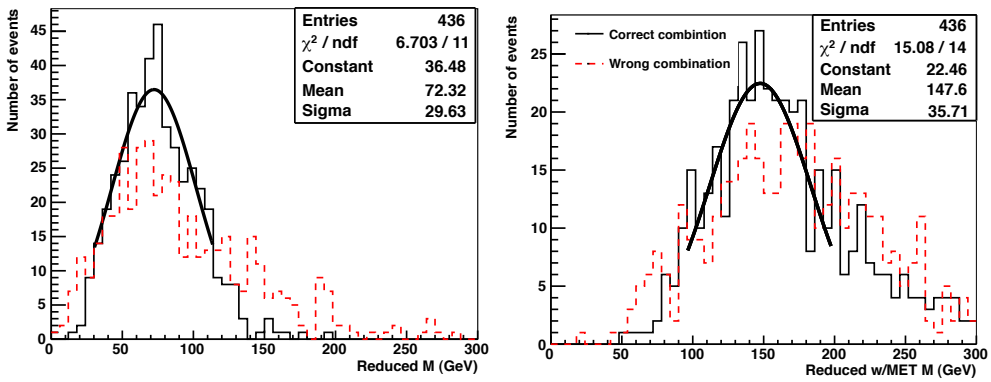

(a) **(b)**

Figure 6.16: Reduced and transverse top mass using truth matched reco variables. Black indicates correct combination of tau and b, while dotted red lines means wrong combination.

Looking at reconstructed variables only, the same considerations for selecting taus and correct combinations of taus as for CA needs to be made. Figure 6.17 shows the reduced mass (black lines) and transverse mass (red dotted lines) as well as the total invariant mass of the top pair are shown for different tau selections. The peaks seen in the truth variables plots are still visible. Requiring at least one tight tau approximately halves the statistics, but leaves a slightly narrower peak than for best available tau pair selection. In addition is gets rid of a large portion of the obviously erroneous very low mass values seen for both types of selection. The main advantage of the best available tau pair selection is that it retains the full statistics while at the same time producing

a clear mass peak. Fitting a Gaussian to the peak of the correct combinations of the reduced mass in Figure 6.16a yields a peak at 72 GeV with $\sigma = 30$ GeV. The corresponding fit for reduced mass requiring at least one tau in Figure 6.17 is a mean at 92 GeV and $\sigma = 39$ GeV. Fitting a Gaussian to the correct combination of reduced mass including $E_{\mathrm{T}}^{\mathrm{miss}}$ yields a peak at 148 GeV and $\sigma = 36$ GeV. While a Gaussian to the peak of the reduced mass including $E_{\mathrm{T}}^{\mathrm{miss}}$ for reconstructed variables Figure 6.17 yield a peak at 199 GeV and $\sigma = 71$ GeV. The peak is shifted towards higher values, and widened when using only reconstructed variables. Performing the same fits for the reconstructed variables where the best available taus has been used leaves the position of the peaks almost unchanged, while the Gaussian is slightly widened (Figure 6.17). The reduced and transverse mass method yield four times greater statistics than masses from CA. This alone makes the reduced mass method better suited for trying to reject $t\bar{t}$ events from other event topologies, which is the aim for the next chapter of this thesis. There is no significant difference observed between adding $E_{\mathrm{T}}^{\mathrm{miss}}$using CA and simply as another four-vector in the transverse mass.

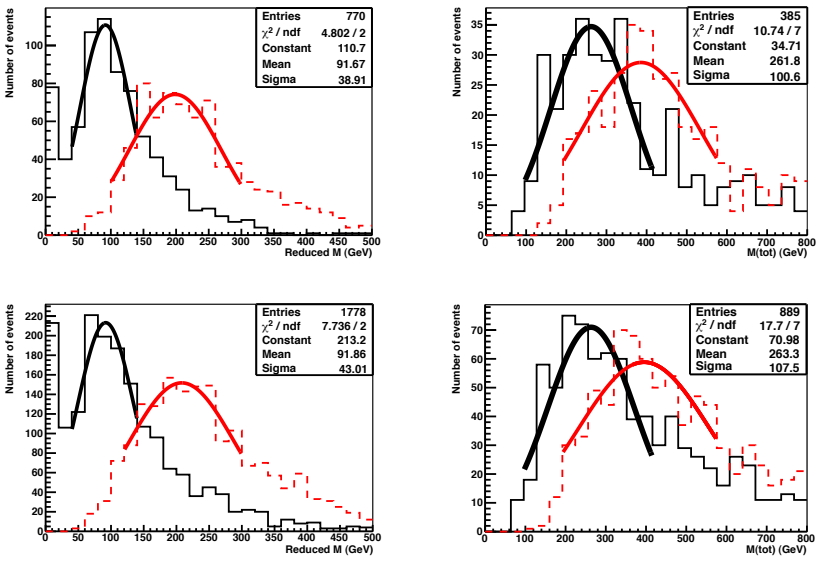

Figure 6.17: Reco: Reduced, transverse and total top mass. - Top: Required at least one tight tau. Bottom: Best available tau pair (two tight taus, one tight and leading or leading and next leading tau). Left: M(top) with combination of tau and b that yields smallest mass difference between the two tops. Right: M(top pair). Black line: Reduced mass. Red dotted line: Transverse mass (includes $E_{\mathrm{T}}^{\mathrm{miss}}$). Stat boxes are for the reduced masses.

7

Top Pairs as SUSY Background

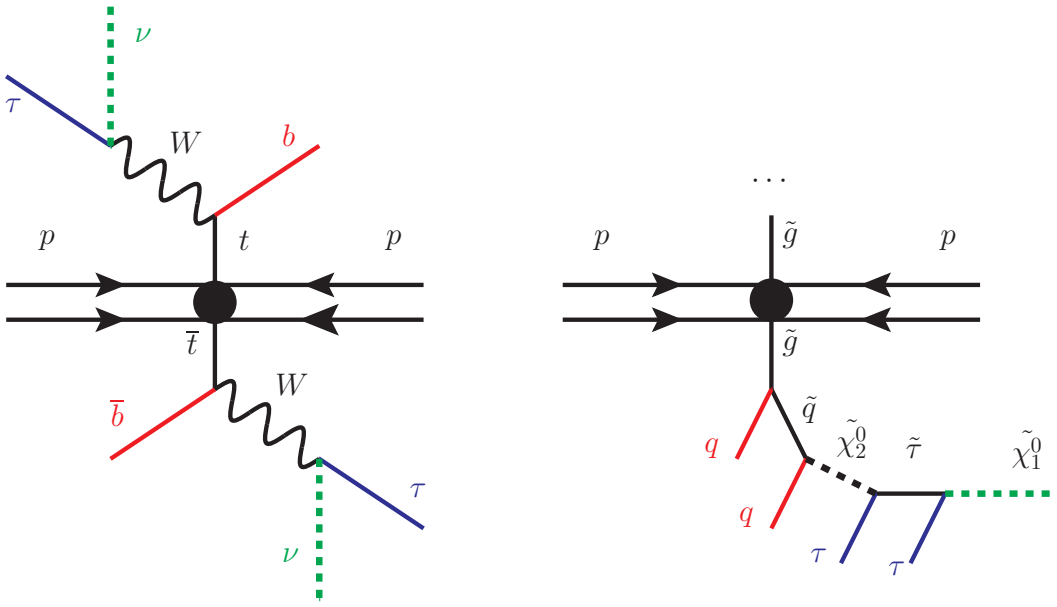

Figure 7.1: $t\bar{t}$ and SUSY events containing two taus - Similarities are indicated with the same color. Dotted lines are particles that escape detection.

Figure 7.1 shows a schematic view of $t\bar{t}$ and SUSY events with two taus. The similarities indicated by the same coloured lines, shows how similar the final states of these two types of events are. In both cases two high-p_T quarks, and consequently jets, are produced, in addition to two taus. Finally, both events contain particles that escape detection, neutrinos and neutralinos in $t\bar{t}$ and SUSY events respectively, and therefore missing energy. In order to detect this possible SUSY signature it is vital, but far from

Process	ID	Generator	Tags	Events	Cross-sec. [pb]
$t\bar{t}$	105200	Jimmy	e510, s765, r1302	999 387	89.4
SU4	106484	Herwig	e542, s765, r1302	49 954	59.95
H. tan(β)	118015	Herwig	e664, s765, r1302	9 982	0.82
H. tan(β)	118016			9 983	0.47
QCD J0	15009	Pythia	e468, s766, r1303	1 399 184	9752970000
QCD J1	15010			1 395 383	673020000
QCD J2	15011			1 398 078	41194700
QCD J3	15012			1 397 430	2193250
QCD J4	15013			1 397 401	87848.7
QCD J5	15014			1 391 612	2328.6
QCD J6	15015			1 347 654	33.85
QCD J7	15016			1 125 428	0.14
WW	105985	Herwig	e521, s765, r1302	249 837	17.4
ZZ	105986			249 725	1.27
WZ	105987			249 830	5.55
Z+jets	107670	Jimmy	e529, s765, r1302	303 359	830
Z+jets	107671			63 481	166
Z+jets	107672			19 492	50.3
Z+jets	107673			5 497	13.9
Z+jets	107674			1 499	3.62
Z+jets	107675			499	0.942
W+jets	107700	Jimmy	e511, s765, r1302	1 365 491	8290
W+jets	107701			254 753	1550
W+jets	107702			188 446	452
W+jets	107703			50 472	120.8
W+jets	107704			12 996	30.33
W+jets	107705			3 998	8.27

Table 7.2: MC samples used for SUSY analysis - MC samples used in this chapter. All samples are MC09, 7 TeV, release 15 v6.20 (p305), common tags s767 and r1306, produced by the SUSY group. Complete information can be found in AMI from the tag numbers.

trivial, to distinguish these two types of events, in order to remove the $t\bar{t}$ and isolate the SUSY signal. This chapter will examine methods to do this, before comparing the results to ATLAS data in the next chapter. MC sampled used in this chapter are listed in Table 7.2.

	SU4 - 106484			$t\bar{t}$ **- 105200**		
Cut	**Events**	**%**	**Ref.**	**Events**	**%**	**Ref.**
Total	2 098 ± 9.4	-	2 098	3 129 ± 3.1	-	3 129
Trigger	1 327 ± 7.5	63.3	1 327	1 134 ± 1.9	36.2	1 134
Jet cleaning	1 314 ± 7.4	99.1	1 314	1 114 ± 1.9	98.2	1 114
Prim. Vertex	1 314 ± 7.4	100	1 314	1 114 ± 1.9	100	1 114
No crack e	1 308 ± 7.4	99.5	1 308	1 100 ± 1.9	98.7	1 100
No e	1 155 ± 7.0	88.3	1 158	753.7 ± 1.5	68.5	759.8
No μ	1 128 ± 6.6	89.0	1 031	491.4 ± 1.2	65.2	497.4
High p_{T} jet	919.7 ± 6.2	89.4	919.2	317.5 ± 1.0	64.6	321.5
Low p_{T} jet	904.0 ± 6.2	98.3	903.2	312.6 ± 1.0	98.5	316.8
$E_{\mathrm{T}}^{\mathrm{miss}}$	690.3 ± 5.4	76.4	689.8	126.3 ± 0.63	40.4	127.2
One Tau	37.34 ± 1.3	5.41	35.37	14.84 ± 0.22	11.8	13.37
m_{Eff}	29.57 ± 1.1	79.2	28.52	11.75 ± 0.19	79.2	10.34
$\Delta\phi(\mathrm{jet}_1, E_{\mathrm{T}}^{\mathrm{miss}})$	29.23 ± 1.1	98.9	28.06	11.61 ± 0.19	98.8	10.20
$\Delta\phi(\mathrm{jet}_2, E_{\mathrm{T}}^{\mathrm{miss}})$	26.88 ± 1.1	92.0	26.21	10.59 ± 0.18	91.2	9.271
$\Delta\phi(\tau, E_{\mathrm{T}}^{\mathrm{miss}})$	25.79 ± 1.0	95.9	25.29	9.68 ± 0.17	91.4	8.391
m_T	16.47 ± 0.83	63.8	17.14	2.49 ± 0.088	25.8	2.154

Table 7.3: Baseline selection - Events left after event selections and object definitions used by the 0-lepton SUSY-group. % is the percent of events remaining compared to before the condition being applied. The column denoted by Ref. is the reference value taken from [34].

7.1 Baseline Selection

In order to ensure that a well understood event selection and common object definitions are used, a cross check with the baseline selection of the SUSY with taus working group was performed. This cross check was performed for the SU4 SUSY and $t\bar{t}$ sample. These object and event selections will be used in the further analysis, with slight modifications to suit a two tau analysis. Table 7.3 shows the baseline selections for a 0-lepton (using

the misleading ATLAS conventions; meaning no e or μ) analysis is shown to yield good agreement with the reference values. The number of events from a given MC sample are scaled to a certain luminosity by a factor

$$a = \frac{\sigma_{\text{sample}} \cdot \mathcal{L}}{N_{\text{sample}}}, \tag{7.1}$$

where σ_{sample} is the cross-section of the sample including efficiencies, $\mathcal{L}$ is the luminosity the sample should be scaled to, and N_{sample} is the number of generated events in the MC sample. The selections will be explained in more detail in the following sections.

7.1.1 Event Preselection

The first event selection criteria is on trigger information that aims to emulate the trigger used in most of the data taking periods, EF_j75_jetNoEF_EFxe25_noMu. This trigger selects events with high energy jets, and large amounts of missing energy. Both important signatures of SUSY events. As this trigger was not available in all data taking periods or in the MC samples used, the response of this trigger was emulated by combining triggers available in all periods. This is done by combining L1 and L2 jet-p_{T} information, with missing energy information at EF level. For an event to pass the trigger we require the jet trigger L1_J55 to fire, and trig_L2_jet_pt to be larger than 70 GeV and ETMiss_EF to be larger than 25 GeV ($E_{\text{T}}^{\text{miss}}$at event filter level).

The second selection, jet cleaning, removes events that contain bad jets. Bad jets are jets that are not associated with in-time real energy deposits in the calorimeter or badly reconstructed jets, which in turn leads to events with large fake $E_{\text{T}}^{\text{miss}}$. This can be due to hardware problems (HEC spikes, EM coherent), LHC beam conditions or cosmic ray showers [35]. Variables used to discriminate between good and bad jets include timing information and energy deposit variables. These are [36]:

- $f_{\text{em}}-$ Energy fraction in EM calorimeter.
- $f_{\text{hec}}-$ Energy fraction in the hadronic end-cap calorimeter.
- $n_{90}-$ Minimum number of cells containing at least 90% of the cluster energy.
- $f_{\text{Q}}-$ Fraction of LAr cells with a cell Q-factor greater than 4000. The Q-factor measures the difference between the measured and expected pulse shape used to reconstruct the cell energy.

- t_{jet} – Jet timing.
- f_{max} – Maximum energy fraction in one calorimeter layer.

The tight bad jet definition provided by the jet/etmiss group was applied. This defines a jet as bad if one of the criteria listed in Table 7.4 are satisfied.

Source removed	**Tight jet cleaning**
EM coherent noise	$f_{\text{em}} > 0.9$ and $f_{\text{Q}} > 0.6$
HEC spikes	$f_{\text{hec}} > 0.3$ and $f_{\text{Q}} > 0.3$
	$f_{\text{hec}} > 1 - f_{\text{Q}}$
	$f_{\text{hec}} > 0.8$ and $n_{90} \leq 5$
Cosmics and beam bkg.	$t_{\text{jet}} > 25$ns
	$f_{\text{em}} < 0.1$
	$f_{\text{max}} > 0.95$ and $\|\eta\| < 2$

Table 7.4: Criteria defining tight jet cleaning - and the source of bad jet removed

The fourth criterium, primary vertex, requires events to have a vertex with at least 4 tracks associated to it, removing non-collision events. The final preselection is on crack electrons. This rejects events that has crack electrons, i.e. electrons that pass through the region between the barrel and the end-cap of the detector ($1.37 < |\eta| < 1.52$). The energy of electrons in the crack region might no be properly measured, which may consequently lead to fake $E_{\text{T}}^{\text{miss}}$. The definition of a well reconstructed electron, and other objects, is given in Chapter 7.1.2.

7.1.2 Object Definitions

Electrons are required to have author 1 or 3, meaning that it is reconstructed from the standard calorimeter cluster algorithms and both the cluster and track-based algorithm respectively [37]. Electrons are further required to have $p_{\text{T}} > 20$ GeV , $|\eta| < 2.47$ in addition to passing the robustMedium electron identification algorithm. This algorithm is optimised against p_{T} and $|\eta|$ and uses calorimeter, track and information from the combination of these two. This includes information on shower shape, leaking into the hadronic calorimeter, track quality and track-calorimeter cluster matching [38]. Electron candidates touching dead OTX are rejected. OTX (optical transmitter) is a part of the calorimeter readout electronics [28].

Muons are required to be reconstructed by one of the following algorithms: StacoMuon, isCombinedMuon or segment-tagged muons as defined in [39]. The differences in the algorithms is mainly related to whether the muons are reconstructed from tracks in the inner detector or the muon system, or a combination of the two. Additionally the muons are required to have $p_T > 20$ GeV, $|\eta| < 2.47$. The muon tracks are further required to be isolated (ptcone20 < 1.8 GeV), meaning that the sum of transverse momenta of all tracks within $\Delta R < 0.2$ of the muon are required to be smaller than 1.8 GeV. Inner detector quality cuts are also applied. At least one hit in the TRT, and at least six in the SCT are required. Muons with $|\eta| < 1.9$ are required to have at least six hits in the TRT. For muons with more than five TRT hits it is required that less than 10% of the total number of hits are TRT outlier hits. For combined muons with momentum measured in the muon system lower than 50 GeV it is required that

$$\frac{p_{\text{MS,extrap.}} - p_{\text{ID}}}{p_{\text{ID}}} > -0.4, \tag{7.2}$$

where $p_{\text{MS,extrap}}$ is the momentum measured in the muon system extrapolated back to the primary vertex and p_{ID} is the momentum measured in the inner detector.

Jets (AntiKt4Topo) with a calibration (EMJES) is used. The calibration factor corrects for pile-up effects and the direction and energy of the jet as found necessary in [40]. The jet algorithm makes use of topological clusters with a distance parameter $R = 0.4$ [41]. Jets are additionally required to satisfy $\eta < 2.5$ and $p_{\text{T}} > 20$ GeV.

The missing energy variable used is MET_Simplified20_RefFinal with a muon correction from the selected muons, without isolation the isolation requirement applied.

The taus are hadronically decaying taus reconstructed by TauRec (antiKt4) and are required to fulfil the following criteria

- $\text{E}_T > 20$ GeV
- Number of tracks = 1 or 3
- |Charge| = 1
- BDT > 0.7
- Electron veto tight
- Muon veto

- Calibrated EM fraction < 0.95

The electron and muon veto are used to ensure that the selected taus are not electrons or muons faking taus. Calibrated EM fraction requires that less than 95% of the total tau energy deposited in the calorimeters are deposited in the EM calorimeter. Which further helps distinguishing taus from electrons.

7.1.3 Overlap Removal

Overlap removal is performed if candidates passing the object selection overlap, with objects defined as above. The overlap is determined purely geometrically by ΔR, and the removal performed as follows

- If an electron or muon is within $\Delta R < 0.2$ of a tau, the electron or muon is kept and the tau is rejected.
- If an electron or a tau is within $\Delta R < 0.2$ of a jet, the electron or tau is kept and the jet is rejected.
- If an electron is within $0.2 < \Delta R < 0.4$ or a muon within $\Delta R < 0.4$ of a jet, the electron or muon is rejected. As they are assumed to belong to the jet.

7.1.4 Event Selection

After event preselection and overlap removal basic event selection is performed on the objects defined above. The two selection criteria, no e and no μ, removes events containing electrons and muons, respectively. High-p_{T} jet demands that events contain at least one jet with $p_T > 120$ GeV, while low-p_{T} jet selects events with ≥ 2 jets with $p_T > 30$ GeV (including the jet with $p_T > 120$ GeV). The $E_{\mathrm{T}}^{\mathrm{miss}}$ cut only accepts events with $E_{\mathrm{T}}^{\mathrm{miss}} >$ 100 GeV. Both the leading jet p_{T} and $E_{\mathrm{T}}^{\mathrm{miss}}$cut is justified not only for its separating powers between signal and background, but also to a large extent due to trigger considerations. Figure 7.2 shows the trigger efficiencies of the $E_{\mathrm{T}}^{\mathrm{miss}}$and jet part of the trigger. The cut values indicated by dashed lines are chosen to be at the start of the plateaus where the trigger efficiency is close to one. This is done to avoid trigger effects from comparing events in regions with different trigger efficiencies.

The remainder of the selection criteria are specific to the one tau analysis, and will consequently not be kept in the two tau analysis. This includes the selection tau

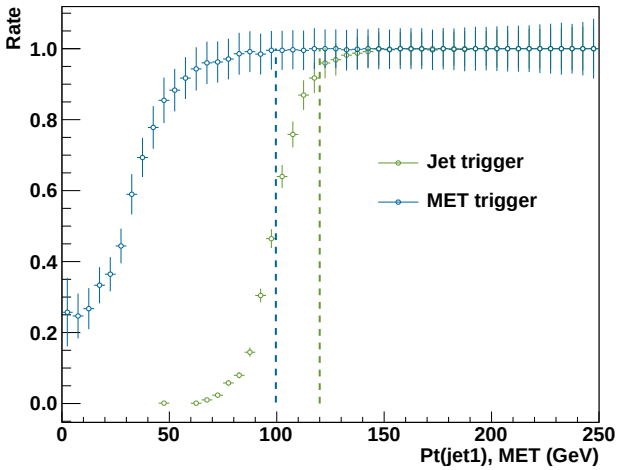

Figure 7.2: Trigger efficiencies - Shows the trigger rate of the jet part of the trigger (L1_J55) as a function of offline leading jet p_{T} (Green markers), and the trigger rate of the $E_{\mathrm{T}}^{\mathrm{miss}}$part of the trigger (ETMiss_EF) as a function of offline $E_{\mathrm{T}}^{\mathrm{miss}}$(blue markers) in the SU4 MC sample. The dashed lines indicates cut values on leading jet p_{T} and $E_{\mathrm{T}}^{\mathrm{miss}}$respectively.

selection, which only accepts events with at least one tau. The remainder of the cuts are mainly performed in order to reduce QCD background. m_{Eff} requires that

$$\frac{E_{\mathrm{T}}^{\mathrm{miss}}}{m_{\mathrm{Eff}}} > 0.25, \tag{7.3}$$

where $E_{\mathrm{T}}^{\mathrm{miss}}$is as defined above, and m_{Eff} is given by

$$\begin{aligned} m_{\mathrm{Eff}} &= |P_{T\,\mathrm{leadingjet}}| + |P_{T\,\mathrm{next-leadingjet}}| \\ &+ |E_{T\,\mathrm{leadingtau}}| + \left(|E_{T\,\mathrm{next-leadingtau}}|\right) + |E_{\mathrm{T}}^{\mathrm{miss}}|, \end{aligned} \tag{7.4}$$

where E_{T} of the next-leading tau is included for two tau analyses. $\Delta\phi(\mathrm{jet}_{1,2}, E_{\mathrm{T}}^{\mathrm{miss}})$ requires that $\Delta\phi(jet, E_{\mathrm{T}}^{\mathrm{miss}}) > 0.4$, where jet1 and jet2 is the p_{T} leading and p_{T}-next-leading jet respectively. While $\Delta\phi(\tau, E_{\mathrm{T}}^{\mathrm{miss}})$ similarly requires that $\Delta\phi(\tau, E_{\mathrm{T}}^{\mathrm{miss}}) > 0.1$, where τ is the p_{T}leading tau of the event. Finally, it is required that $m_T > 100$ GeV to reduce the contribution from W bosons with tau decays. This is the transverse mass of the leading tau and the missing energy, calculated as follows

$$m_T = \sqrt{m_\tau^2 + 2E_{\mathrm{T}}^{\mathrm{miss}} E_{T\tau}^2 - E_{T\tau}\cos[\Delta\phi(\tau, E_{\mathrm{T}}^{\mathrm{miss}})]} \tag{7.5}$$

7.2 Selecting mSUGRA Points

The SU4 SUSY sample is a low mass benchmark point used in the the ATLAS experiment. As this point contains low mass SUSY sparticles and has a relatively high cross section it has already been ruled out by experiment. Another set of SUSY points that are not excluded will therefore be chosen and used in the remainder of this analysis. Supersymmetric models gives varying predictions depending on what the free parameters of the theory are chosen to be. Different parameters leads to different branching fractions as well as masses and mass hierarchies of the SUSY particles. It is thus possible to choose values of the model that are measurable and satisfies current experimental constraints. For this analysis a tau-rich model within experimental bounds as of today, is desirable.

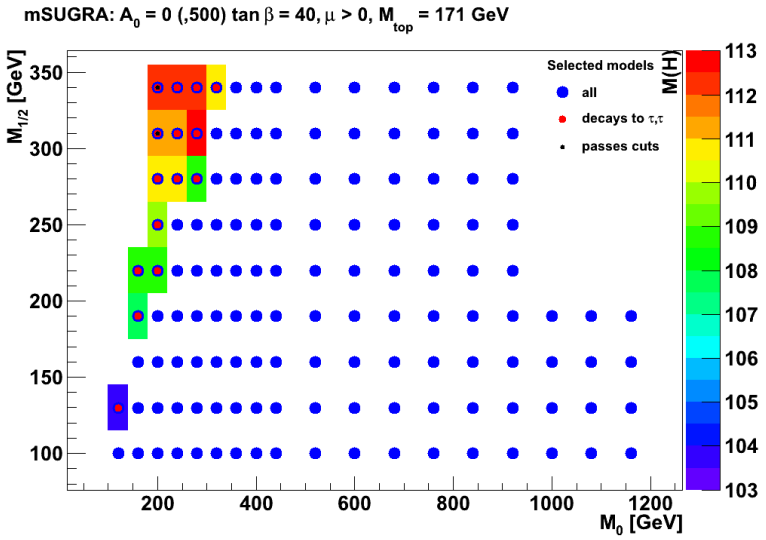

Figure 7.3: Selecting high $\tan(\beta)$ **points** - Points in ATLAS high $\tan(\beta)$ grid. Red dots within blue means models with decay to $\tilde{\tau}$ and τ. Black dots within the red are points that satisfy our criteria. Colours beneath points indicate the Higgs mass of the model. Plot made by Thomas Burgess.

ATLAS has produced a high $\tan(\beta)$ grid, which is a collection of mSUGRA points with $\tan(\beta) = 40$. The high $\tan(\beta)$ grid has parameters

$$\tan(\beta) = 40, A_0 = 0 \vee 500, \mu > 0, M(t) = 171\text{GeV},$$

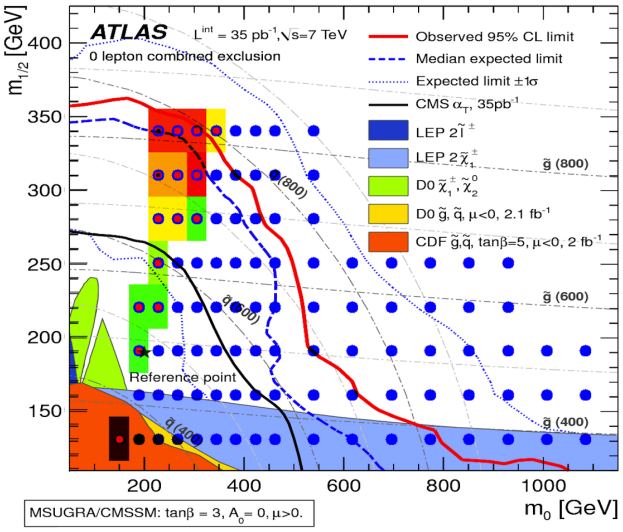

Figure 7.4: High $\tan(\beta)$ **grid with 0-lepton exclusion** - As the 0 leptons analysis is not highly dependent on $\tan\beta$ one can get a rough estimate for the $\tan\beta = 40$ points by doing an overlay with the 0 lepton exclusion limits for $\tan\beta = 3$. Plot made by Thomas Burgess.

where $M(t)$ is the top quark mass and m_0 and $m_{\frac{1}{2}}$ varies in the ranges 100 - 1200 GeV and 100 - 350 GeV respectively. These points are tau rich, contains a large number of b-jets in addition to having a relatively high neutral Higgs mass. Points with desirable characteristics were selected from this grid.

The decay chain for a tau signal in the co-annihilation region is

$$\tilde{g} \to q, \tilde{q}_L \to q, \tilde{\chi}_2^0 \to \tau, \tilde{\tau} \to \tau, \tilde{\chi}_1^0 \tag{7.6}$$

This requires the following mass hierarchy

$$M(\tilde{q}_L) > M(\tilde{\chi}_2^0) > M(\tilde{\tau}) > M(\tilde{\chi}_1^0) \tag{7.7}$$

Co-annihilation requires that the mass difference between $\tilde{\tau}$ and $\tilde{\chi}_1^0$ is small. However, the soft tau must still be detectable to be of interest to us, necessitating a lower bound on this mass difference. A mass difference of 3 GeV $< \Delta M(\tilde{\tau}, \tilde{\chi}_1^0) <$ 20 GeV, was thus required. It should be noted that this lower bound is below what is detectable with ATLAS for staus decaying at rest in the lab frame, as track based tau reconstruction requires a 6 GeV track, and calorimeter tau reconstruction requires 10 GeV energy deposit in the calorimeters.

The current limits on the Higgs mass constraints which SUSY points are allowed, as the SUSY points needs to produce a neutral Higgs consistent with the current Higgs mass limits. From LEP the 95% confidence level lower Higgs mass limit is 114.4 GeV [42]. The experimental results depend on the underlying model, which limits them to the Standard Model Higgs. Supersymmetric models could thus prefer another Higgs mass from the same data sample [19]. mSUGRA points with Higgs mass above 111 GeV were therefor selected. As this is a study of SUSY with taus, tau-rich models are of interest. A high branching ratio to $\tilde{\tau}, \tau$ pairs was thus required. More specifically points with a branching ratio of BR$(\tilde{\tau}^{\pm}, \tau^{\mp}) > 0.9$ was chosen. In addition to this the lightest left squark mass was required to be low, in order for events to be produced at the expected luminosity: M$(\tilde{q}_L) < 1$ TeV. The points in this grid are generated using IsaSUGRA which calculates the branching ratios and masses. Cross-sections can be determined in Herwig or Prospino, while neutralino relic densities can be found through Dark Susy.

Model	M_0	$M_{1/2}$	$\Delta M(\chi_1^0, \tilde{\tau})$	BR$(\tilde{\tau}^{\pm}\tau^{\mp})$	M$(\tilde{g})$	M(H_L)
118015	200	310	17.70	0.992	744.7	111.4
118016	200	340	6.98	0.970	810.9	112.1

Table 7.5: Selected high tan(β) **models** - Shows the main parameters of the two high tan(β) models that pass our selection criteria. Mass quantities are in GeV.

Applying the above conditions leaves the two points from the ATLAS high tan(β) grid shown in Table 7.5. In Figure 7.3 the models in the high tan(β) grid are showed in the $M_{\frac{1}{2}}$-M_0 plane. The blue dots are all the models, red dots are points that has $\tilde{\tau} + \tau$ decay channel. While the black dots are indicates points passing our requirements. The background colour shows the Higgs mass of the mSUGRA point. There are other points where taus are also produced, but these are via a different decay chain (three-body decay).

Figure 7.4 shows an overlay of Figure 7.3 with an exclusion plot from 0-lepton analysis on the tan(β) = 3 grid. It is clear that the selected points are bordering on being excluded, as the 0-lepton searches should not depend much on tan(β). Applying the same conditions to the low tan(β) grid (tan(β) = 3, $A_0 = 0$ or 500, $\mu > 0$, M(t) > 171 GeV) produced no interesting points. This is mainly due to the low mass of the Higgs in this grid.

7.3 Two Tau Cutflow

Cut	118015	118016	SU4	$t\bar{t}$
Total	28.79 ± 0.29	16.42 ± 0.16	2098 ± 9.4	3129 ± 3.1
Trigger	28.19 ± 0.29	16.17 ± 0.16	1327 ± 7.5	1134 ± 1.9
Jet cleaning	27.51 ± 0.28	15.90 ± 0.16	1314 ± 7.4	1115 ± 1.9
Prim. vertex	27.51 ± 0.28	15.90 ± 0.16	1314 ± 7.4	1115 ± 1.9
No crack e	27.43 ± 0.28	15.85 ± 0.16	1309 ± 7.4	1100 ± 1.9
No e	25.22 ± 0.27	14.84 ± 0.16	1155 ± 7.0	753.6 ± 1.5
No μ	23.47 ± 0.26	13.88 ± 0.15	1128 ± 6.6	491.0 ± 1.2
High p_{T} jet	23.00 ± 0.26	13.65 ± 0.15	907.2 ± 6.2	310.8 ± 1.0
Low p_{T} jet	22.23 ± 0.25	13.15 ± 0.15	880.0 ± 6.1	304.1 ± 1.0
$E_{\mathrm{T}}^{\mathrm{miss}}$	20.91 ± 0.25	12.55 ± 0.14	677.4 ± 5.3	122.5 ± 0.62
two τ	0.9663 ± 0.053	0.3075 ± 0.022	13.02 ± 0.74	3.488± 0.10

Table 7.6: Two tau cutflow on high $\tan(\beta)$ **models, SU4 and** $t\bar{t}$ - Shows the number of events after each cut normalised to 35pb^{-1}.

Using the same event preselection and object definitions, with the exception for taus, as in Chapter 7.1 a new cut flow to suit a two tau analysis was made. The difference in object definitions is in the selection of taus, where two taus with BDT > 0.5 was used. Additionally to the QCD and W requirements following the selection on number of taus were removed. The loosening of the BDT requirement was done to retain more statistics. This however is expected to lead to more misidentified taus, mainly from QCD jets identified as taus, as discussed in Chapter 5. The removal of the QCD cuts and loosening of the tau ID should to a large extent be counteracted by the fact that the QCD background is significantly reduces by selecting two taus as opposed to one. As expected the cuts are identical to those in the one tau cutflow in Table 7.3 for all the event preselection cuts. There are slight deviations on the results of electron, muon and jet cuts. This is can be understood by the change in the tau selection, where a loose tau object definition will lead to selection of mote taus, and consequently a different overlap removal with the other leptons and jets.

Table 7.6 shows this new cutflow for the two high $\tan(\beta)$ points found in Chapter 7.2 and $t\bar{t}$ normalised to an integrated luminosity of 35 pb^{-1}. The new tau cut is quite hard, keeping only 4.6%, 2.6% and 2.85% of high $\tan(\beta)$ 118015, 118016 and $t\bar{t}$

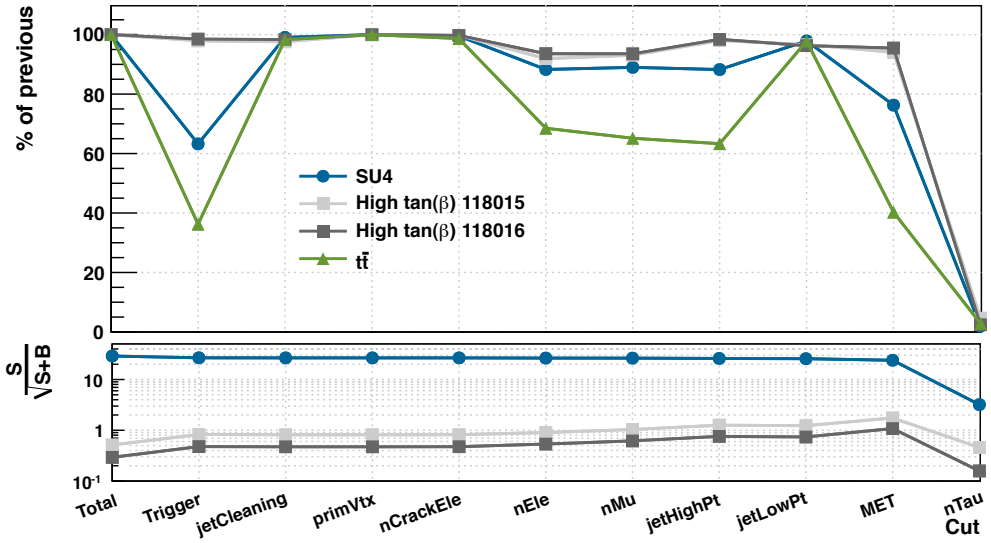

Figure 7.5: Significance and percentage remaining after cuts - Percentage of events left with respect to previous event and $\frac{S}{\sqrt{S+B}}$ after each cut scaled to 35 pb^{-1} integrated luminosity. Background here is $t\bar{t}$ only.

respectively. As expected more events in model 118015 than in 118016 pass the tau cut. This is is due to the fact that the soft tau in 118016 is often not reconstructable due to its low momentum, evident from the low mass difference between the lightest neutralino and tau, shown in Table 7.5. Compared to SU4 in Table 7.3 it is clear that the two high tan(β) models has a relatively low production cross section, and a total of 16.42 and 28.79 events are expected at 35 pb^{-1} for model 118015 and 118016 respectively, compared to 2 098 SU4 events at the same luminosity. On the other hand a larger percentage of the events in these models pass the trigger, jet, missing energy and tau cuts than for SU4 events, as shown in 7.5.

Figure 7.5 shows the significance and percentage of events remaining with respect to before the cut for different SUSY models after each of the cuts made in Table 7.6 for an integrated luminosity of 35 pb^{-1}. The significance is obtained using the measure

$$R = \frac{S}{\sqrt{S+B}}, \tag{7.8}$$

where S and B are the number of signal and background events respectively. The significance for the two high $\tan\beta$ points increase steadily until the tau cut, where it drops of sharply. This is justified by the fact that this is not a cut performed to

optimise the significance as the others are, but rather a cut that is enforced through requiring a two tau analysis. This cut should be optimised for maximum separation of signal with respect to QCD by optimising the choice of BDT for one and three prong taus separately.

7.4 Mass Variables

The difference in the decay chains shown in Figure 7.1 should result in different invariant masses of the same final state particles as they originate from particles of different masses. This information may be used to separate SUSY from $t\bar{t}$ events by using the mass variables investigated in Chapter 6. CA was found to have a lower efficiency and no significant improvement of the reconstructed mass compared to the reduced mass.

The reduced mass was found to give a narrower peak, and a larger difference between correct and wrong combinations of jets and taus compared to the reduced mass including missing energy. This should make it more suitable for both making the correct particle combinations as well as separating it from a SUSY signal.

Figure 7.6 shows the distributions, signal left, background rejected and significance for a given cut value for the heaviest, lightest and total reduced mass respectively. The optimal cut value for the combination of the two high tan(β) models are indicated by a vertical line. The optimisation was done by finding the cut value of the variable that yields the highest value of significance for the sum of the two SUSY points. The optimisation was performed on the sum of the of the two to increase statistics and avoid too strong model dependence. Table 7.7 shows the optimised cut values for the reduced mass variables, and the signal kept, background rejected of these cuts. All numbers and figures are normalised to 35 pb^{-1} integrated luminosity. Instead of using the $E_{\mathrm{T}}^{\mathrm{miss}}$

			118015		**118016**	
Variable	**Cut [GeV]**	**Bkg rej. [%]**	**left [%]**	$\frac{S}{\sqrt{S+B}}$	**left [%]**	$\frac{S}{\sqrt{S+B}}$
Heaviest M_{top}	195	43	87	0.50	89	0.18
Lightest M_{top}	111	43	85	0.49	87	0.18
Total M_{tops}	563	55	78	0.50	82	0.19

Table 7.7: Cut values for reduced mass variables - Optimised for maximal significance on combination of both high tan(β) models.

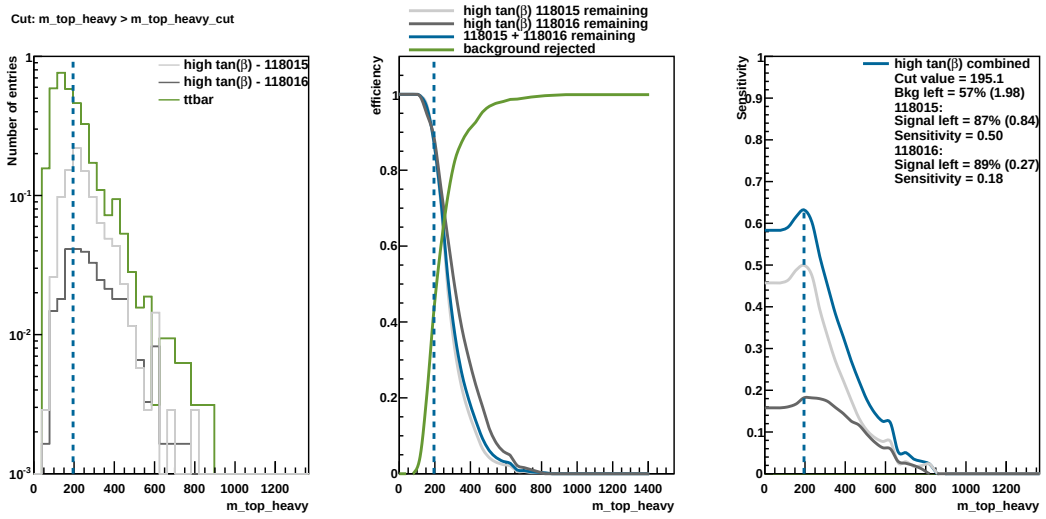

(a) Heaviest reduced mass of top (GeV)

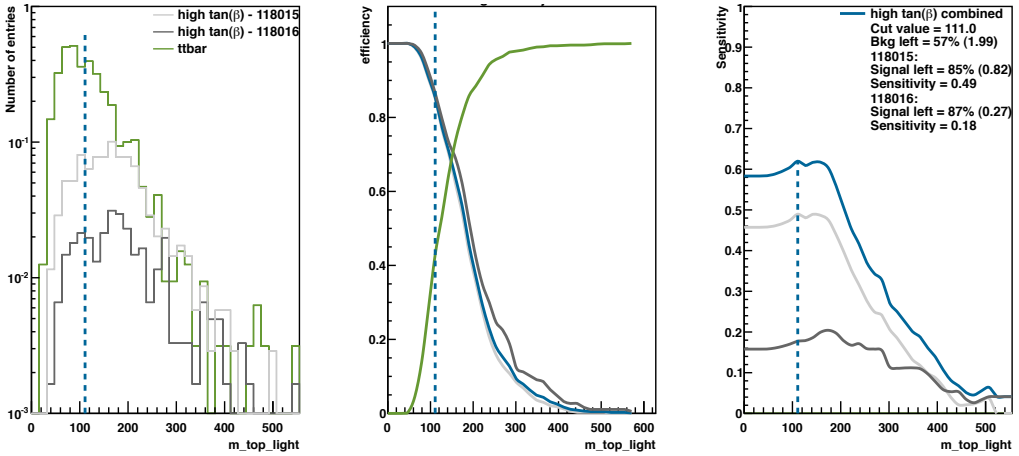

(b) Lightest reduced mass of top (GeV)

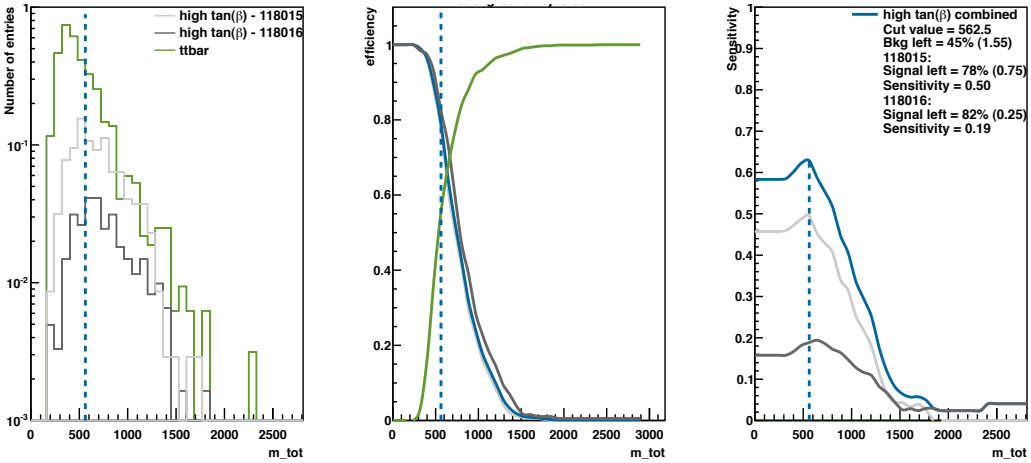

(c) Total reduced mass (GeV)

Figure 7.6: Mass variable cuts - Left: Distribution. Middle: Signal left and $t\bar{t}$ rejected. Right: Sensitivity of models with respect to $t\bar{t}$. Dashed line indicates maximum sensitivity.

information in the reduced mass variable, the $E_{\mathrm{T}}^{\mathrm{miss}}$ may be combined with the reduced mass in two dimensional distributions in order to increase the discriminatory power. Single variables and correlations between discriminatory variables will be investigated in the following sections.

7.5 Additional Variables

Looking at single mass variables in the previous section yields some discriminating power between top pair events and a SUSY signal. However, other variables and combinations of these looking for possible correlations in two dimensions can improve the separation between these to types of events. To this end a total of 57 variables and the combinations of these variables were investigated. Most of the variables are kinematic variables of taus and jets, but it also includes event shape variables and other variables defined by the SUSY group at ATLAS [43]. Small Ntuples were made for all the MC samples containing the variables to be investigates. Automated scripts to optimise single cuts and two-dimensional selections on all the correlations of the variables was developed.

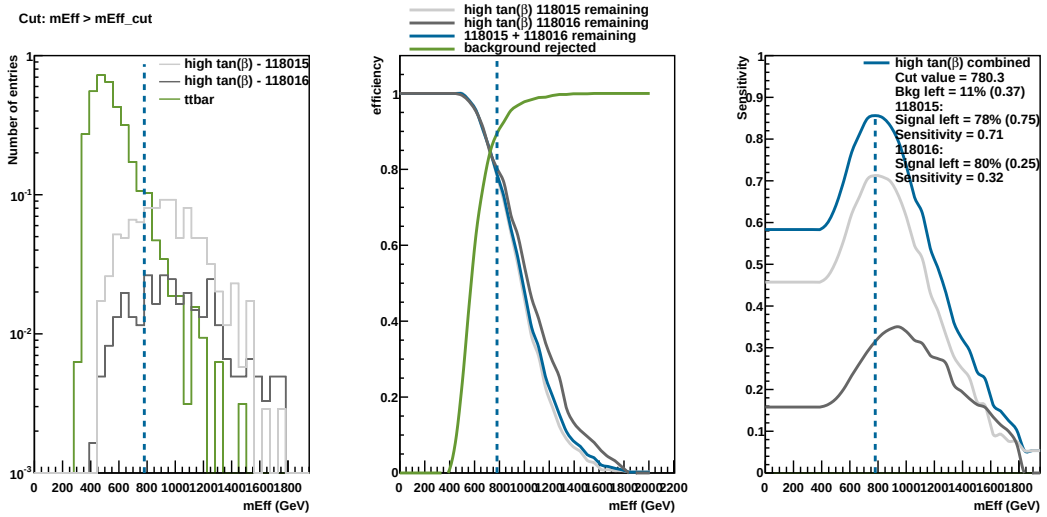

Figure 7.7: Cut on m_{Eff} - Individual high tan(β) models and combinations of the two (dashed). Left: variable distribution. Middle: Signal remaining and background rejected, Right: Significance

The investigated variables that was found to improve the significance are listed in

Table 7.8. This shows the cut optimised for the largest sensitivity of the sum of the two points compared to $t\bar{t}$ background, along with the effects of this cut on $t\bar{t}$ and SUSY samples. Optimisation is done after the cuts in Table 7.6. The kinematic variables include angles between combinations of jets and taus in the transverse plane, $\Delta\phi$, $\Delta\eta$ and ΔR. Scalar and vector sums and differences of combinations of jet and tau energy and momentum variables, in addition to individual energy and angular variables. The transverse mass between the jets and taus was investigates, given as

$$m_T(1,2) = \sqrt{\left(\sqrt{E_1^2 - p_{z,1}^2} + \sqrt{E_2^2 - p_{z,2}^2}\right)^2 - (p_{x,1} + p_{x,2})^2 - (p_{y,1} + p_{y,2})^2}, \quad (7.9)$$

where $1, 2$ indicates the first and second particle. The transverse mass between a particle and $E_{\mathrm{T}}^{\mathrm{miss}}$, which is a two vector in the transverse plane is defined as

$$m_T^f = \sqrt{m_f^2 + 2 \cdot p_{\mathrm{T}}^f \cdot E_{\mathrm{T}}^{\mathrm{miss}} \cdot (1 - \cos\Delta\phi(f, E_{\mathrm{T}}^{\mathrm{miss}}))}, \quad (7.10)$$

where f indicates the particle.

The SUSY variables that improved the significance are defined as

$$H_T = |p_T(\mathrm{jet}_1)| + |p_T(\mathrm{jet}_2)| + |p_T(\tau_1)| + |p_T(\tau_2)| \quad (7.11)$$

where subscript 1 and 2 means p_T-leading and next-leading respectively. $H_{\mathrm{T,miss}}$ is defined as

$$H_{\mathrm{T,miss}} = \sum_{\mathrm{jets},\tau\mathrm{s}} \boldsymbol{p}_T, \quad (7.12)$$

where jets are all the jets satisfying $p_T > 30$ GeV and $|\eta| < 4.5$ in the event, and the taus are the two selected taus. m_{Eff} may be re-written as

$$m_{\mathrm{Eff}} = H_T + E_{\mathrm{T}}^{\mathrm{miss}}. \quad (7.13)$$

Distributions, signal remaining, background rejected and significance for the four variables that yielded the highest significance for the two points are shown in figures 7.8 and 7.7. m_{Eff} is found to yield the highest significance, followed closely by $E_{\mathrm{T}}^{\mathrm{miss}}$and finally HT and $H_{\mathrm{T,miss}}$. These variables describe roughly the same quantities, where m_{Eff} is just the sum of $E_{\mathrm{T}}^{\mathrm{miss}}$and HT, while also $H_{\mathrm{T,miss}}$ describe the transverse momentum of taus and jets in an event, the similar performance is in this respect not surprising.

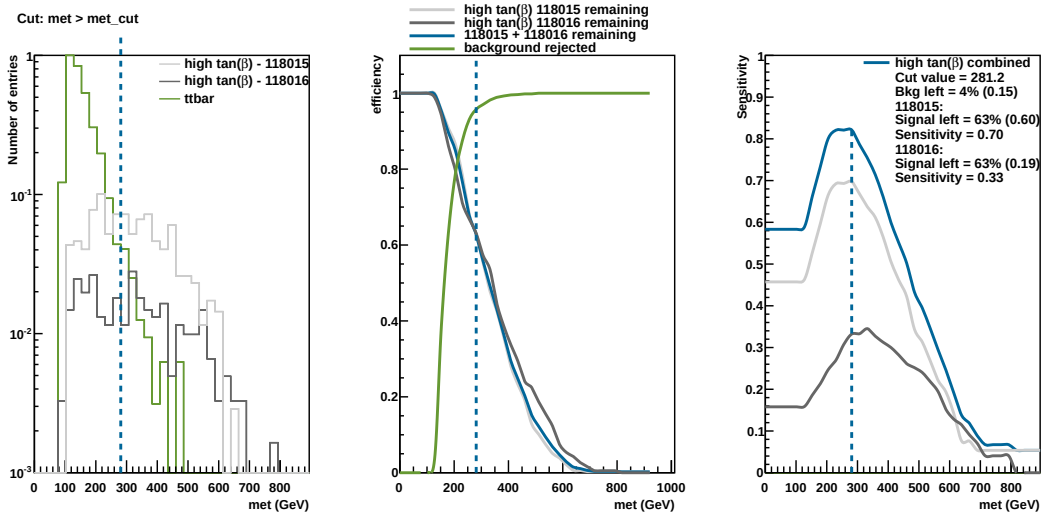

(a) $E_{\mathrm{T}}^{\mathrm{miss}}$

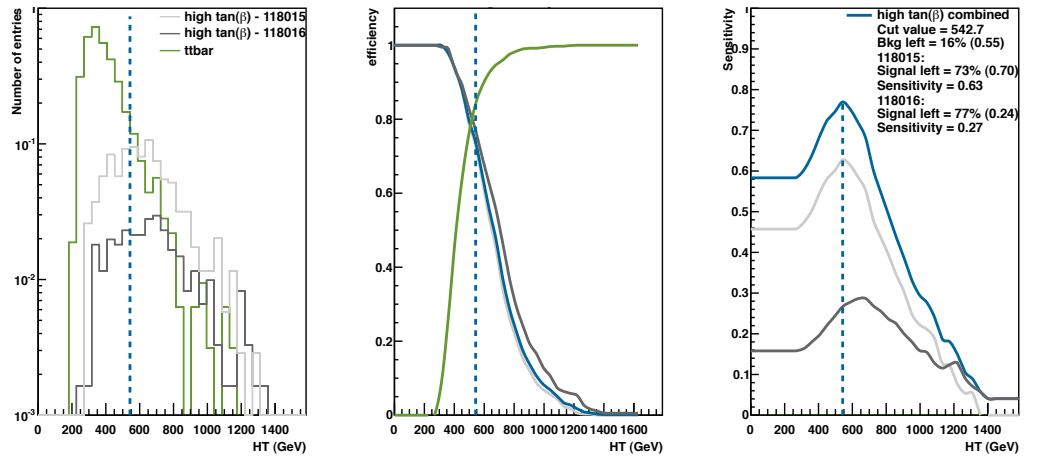

(b) H_T

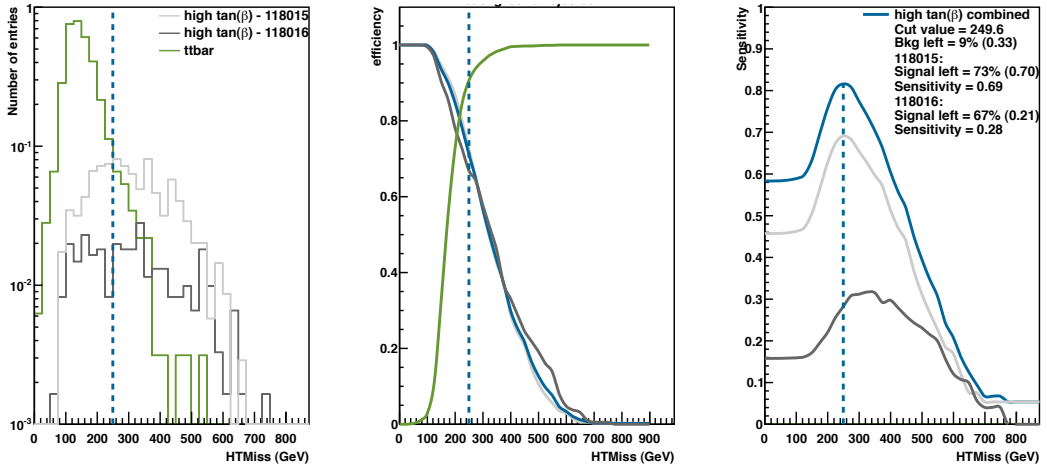

(c) $H_{\mathrm{T,miss}}$

Figure 7.8: Other variable - Left: Distribution. Middle: Signal left and $t\bar{t}$ rejected. Right: Sensitivity of models with respect to $t\bar{t}$. Dashed line indicates maximum sensitivity.

Looking at correlations between these variables may reveal some advantageous relations, enabling a cut in two dimensions to improve on two single variable cuts. This will be investigated in the following section.

			118015		118016	
Variable	**Cut [GeV]**	**Bkg rej. [%]**	**left [%]**	$\frac{S}{\sqrt{S+B}}$	**left [%]**	$\frac{S}{\sqrt{S+B}}$
$H_{\mathrm{T,miss}}$	250	91	73	0.69	67	0.28
H_T	543	84	73	0.63	77	0.27
$\mathrm{P}(\mathrm{jet}_1)$	283	43	86	0.49	86	0.18
$\mathrm{P}(\mathrm{jet}_2)$	184	60	75	0.49	67	0.16
$\Delta\eta(\mathrm{jet}_1, \mathrm{jet}_2)$	2.2	5	98	0.46	100	0.16
$\Delta P(\mathrm{jets}, \mathrm{taus})$	189.4	25	92	0.47	82	0.15
$\Delta R(\mathrm{jet}_1, \mathrm{jet}_2)$	3.8	6	97	0.46	98	0.16
$\Delta\phi(\mathrm{jet}_2, E_{\mathrm{T}}^{\mathrm{miss}})$	3.1	14	90	0.46	89	0.16
$E_T(\mathrm{jet}_1)$	273	85	62	0.56	67	0.24
$E_T(\mathrm{jet}_2)$	147	85	58	0.55	55	0.20
$\Sigma\lvert E_T(\mathrm{jets})\rvert$	366	79	76	0.60	76	0.24
$\Sigma\vec{E}_T(\mathrm{jets})$	405	87	64	0.60	63	0.24
$\Sigma\vec{E}_T(\mathrm{jets,\ taus})$	459	79	75	0.60	76	0.24
m_{Eff}	780	89	78	0.71	80	0.32
$m_T(\mathrm{jet}_1, E_{\mathrm{T}}^{\mathrm{miss}})$	466	88	72	0.66	70	0.27
$m_T(\mathrm{jet}_2, E_{\mathrm{T}}^{\mathrm{miss}})$	310	93	58	0.63	49	0.24
$m_T(\mathrm{jets})$	66	4	99	0.46	100	0.16
$m_T(\mathrm{jets}, \mathrm{taus})$	561	65	71	0.49	78	0.20
$E_{\mathrm{T}}^{\mathrm{miss}}$	281	96	63	0.70	63	0.33
Th_T	0.1	4	99	0.46	98	0.16

Table 7.8: 1D cut values - Optimised for maximal $\frac{S}{\sqrt{S+B}}$ on sum of the two high $\tan(\beta)$ points with only $t\bar{t}$ considered as background.

7.6 Combinations of Variables

In previous sections all the variables have been considered separately. However performing cuts in two dimensions spanned by two variables can prove to be a significant improvement over consecutive one dimensional cuts, provided there is different correlations between the variables in the signal and background sample.

There are different ways to perform the cuts in two dimensions, and in how to optimise the cut values. One way to make a cut in two dimensions is to cut on an ellipse in the plane spanned by the two variables. Optimising the cut can be done by finding the ellipse that gives largest significance after removing events laying within or outside a given ellipse. The ellipse has major and minor axis along the x- or y axis. A simpler method that avoids the rather brute-force optimisation of an ellipse in two dimensions is also possible. This is done by making a "radius" of the two variables, before making a one dimensional cut on this radius maximising significance as in the previous section. Although this method is simpler and quicker than the elliptical cut it constitutes a small information loss. Both these methods rely on optimisation of significance on variable distributions directly. In stead the cut can be made by a simple, statistically well defined method called Fisher discriminant analysis. The fundamental properties of this method will be explained in the following section.

7.6.1 Fisher Discriminant Analysis

Given a vector of data $\boldsymbol{x} = (x_1, ..., x_n)$, from which one would like to construct a one-dimensional test statistic $t(\boldsymbol{x})$ to distinguish between two hypotheses H_0 and H_1, e.g. signal and background. The best test statistic is given by the likelihood ratio [44]

$$t(\boldsymbol{x}) = \frac{f(\boldsymbol{x}|H_0)}{f(\boldsymbol{x}|H_1)} \tag{7.14}$$

This however requires that $f(\boldsymbol{x}|H_0)$ and $f(\boldsymbol{x}|H_1)$ are known. They can be determined from Monte Carlo simulations, but this quickly becomes cumbersome for large n. In stead a simpler assumption about the form of $t(\mathbf{x})$ can be made. The best function of this form according to some criteria can then be selected. The simplest form for the test statistics is a linear function, from which the Fisher discriminant function can be constructed [44]:

$$t(\boldsymbol{x}) = \sum_{i=1}^{n} a_i x_i = \boldsymbol{a}^T \boldsymbol{x}, \tag{7.15}$$

where $\boldsymbol{a}^T = (a_1, ..., a_n)$ is the row vector of coefficients. The goal is to determine a_i such that the separation between the probability density functions $g(t|H_0)$ and $g(t|H_1)$ is maximised. One approach to maximise this separation was developed by Fisher [45].

Each hypothesis is characterised by a certain expectation value, $\tau_{0,1}$, and variance, $\Sigma_{0,1}$, for t. To maximise the separation between the hypotheses one should maximise

$|\tau_0 - \tau_1|$, while the spread around these mean values, determined by the variances, should be as low as possible. A measure of separation that takes both of these factors into account is

$$J(\boldsymbol{a}) = \frac{(\tau_0 - \tau_1)^2}{\Sigma_0^2 + \Sigma_1^2}. \tag{7.16}$$

Equation 7.16 can be written in terms of a_i and the mean values and covariance matrix of the data $\boldsymbol{x}$, provided that the data are normally distributed. In doing so and setting the derivative of $J(\mathbf{a})$ with respect to a_i equal to zero to find the maximum separation gives

$$\boldsymbol{a} \propto W^{-1}(\boldsymbol{\mu_0} - \boldsymbol{\mu_1}), \tag{7.17}$$

where $\boldsymbol{\mu}_{0,1}$ are the expectation values of the data $\boldsymbol{x}$ for the hypothesis $H_{0,1}$. And $W_{ij} = (V_0 + V_1)_{ij}$, where $V_{0,1}$ are the covariance matrices of the data for hypothesis $H_{0,1}$. The test statistics based on equations 7.15 and 7.17 is called Fishers linear discriminant function [44]

Now that the $\boldsymbol{a}$ is determined for the hypothesis signal and background, the Fisher sum $t(x)$ can be calculated for each variable pair in an event. A one-dimensional cut can then be made on this sum by optimising the sensitivity.

7.6.2 Comparing Cut Methods

The performance of the three cut methods on the variable combinations yielding the largest discriminatory power can be seen in tables 7.9, 7.10, 7.11. The elliptical cut and the cut on the Fisher sum is found to perform quite similarly. Due to the simplicity of the method the elliptical cut will be used in the further analysis. The last cut method investigated is on a radius, which allows for quicker and simpler cut optimisation. This is done by scaling each of the two axis to one, before calculating the radius from the origin in this scaled coordinate system. The cut is then optimised and performed on this one dimensional radius. This method corresponds to optimisation on a single elliptical shape in the unscaled histogram, and in this respect is a simplification of the elliptical cut. Using this method a slightly lower sensitivity than for the elliptic and fisher cut is obtained, but it proves a significant improvement over a simple radius/circular cut on the unscaled histogram.

Plots showing the performance of the different cut methods can be seen for the variables yielding highest significance and the different methods in figures 7.9 - 7.13. It

			118015		118016	
Variables	**Cut [GeV]**	**Bkg rej. [%]**	**Left [%]**	$\frac{S}{\sqrt{S+B}}$	**Left [%]**	$\frac{S}{\sqrt{S+B}}$
$E_{\mathrm{T}}^{\mathrm{miss}}$, $\sum \mid E_T(jets) \mid$	277, 663	94	77	0.76	73	0.34
$E_{\mathrm{T}}^{\mathrm{miss}}$, $\mathrm{M}_T$jets	242, 681	93	77	0.75	73	0.33
HT, HTmiss	871, 271	91	79	0.74	75.4	0.32
$E_{\mathrm{T}}^{\mathrm{miss}}$, HT	259, 902	93	78	0.75	77	0.34
$m_T(\mathrm{jet2}, E_{\mathrm{T}}^{\mathrm{miss}})$, m_{Eff}	558, 839	93	77	0.75	79	0.35
$E_{\mathrm{T}}^{\mathrm{miss}}$, m_{Eff}	349, 917	92	79	0.75	80	0.34
$E_T(\mathrm{jet2})$, $H_{\mathrm{T,miss}}$	223, 271	91	82	0.75	75	0.31

Table 7.9: Elliptic - the cut selects points outside the ellipse given by the the minor- and major axis in cut column along the axes defined by the variables. $t\bar{t}$ rejected, signal kept and significance of cut also given.

			118015		118016	
Variables	**Cut**	**Bkg rej. [%]**	**Left [%]**	$\frac{S}{\sqrt{S+B}}$	**Left [%]**	$\frac{S}{\sqrt{S+B}}$
$\sqrt{\left(\frac{E_{\mathrm{T}}^{\mathrm{miss}}}{883}\right)^2 + \left(\frac{\sum\lvert E_T(jets)\rvert}{1149}\right)^2}$	0.39	87	86	0.73	81	0.29
$\sqrt{\left(\frac{E_{\mathrm{T}}^{\mathrm{miss}}}{883}\right)^2 + \left(\frac{M_T(jets)}{1139}\right)^2}$	0.39	93	72	0.71	71	0.32
$\sqrt{\left(\frac{HT}{1566}\right)^2 + \left(\frac{HTmiss}{864}\right)^2}$	0.46	93	72	0.72	0.34	75
$\sqrt{\left(\frac{E_{\mathrm{T}}^{\mathrm{miss}}}{906}\right)^2 + \left(\frac{HT}{1603}\right)^2}$	0.40	89	82	0.73	82	0.31
$\sqrt{\left(\frac{m_T(\mathrm{jet2},E_{\mathrm{T}}^{\mathrm{miss}}}{404}\right)^2 + \left(\frac{m_{\mathrm{Eff}}}{946}\right)^2}$	0.48	92	77	0.73	74	0.32
$\sqrt{\left(\frac{E_{\mathrm{T}}^{\mathrm{miss}}}{398}\right)^2 + \left(\frac{m_{\mathrm{Eff}}}{868}\right)^2}$	0.45	91	81	0.74	81	0.33
$\sqrt{\left(\frac{E_T(\mathrm{jet2})}{192}\right)^2 + \left(\frac{H_{\mathrm{T,miss}}}{293}\right)^2}$	0.34	88	85	0.74	77	0.29

Table 7.10: Radius - optimal cut selects the radius higher than the indicated cut value. $t\bar{t}$ rejected, signal kept and significance of cut also given.

			118015		118016	
Variables	**Cut**	**Bkg rej. [%]**	**Left [%]**	$\frac{S}{\sqrt{S+B}}$	**Left [%]**	$\frac{S}{\sqrt{S+B}}$
$E_{\mathrm{T}}^{\mathrm{miss}}$, $\sum \mid E_T(jets) \mid$	0.01	90	83	0.74	78	0.31
$E_{\mathrm{T}}^{\mathrm{miss}}$, $\mathrm{M}_T$jets	0.17	96	73	0.76	70	0.35
HT, HTmiss	-0.04	85	88	0.72	83	0.29
$E_{\mathrm{T}}^{\mathrm{miss}}$, HT	0.10	92	78	0.74	80	0.34
$m_T(\mathrm{jet2}, E_{\mathrm{T}}^{\mathrm{miss}})$, m_{Eff}	0.12	93	78	0.75	77	0.34
$E_{\mathrm{T}}^{\mathrm{miss}}$, m_{Eff}	0.10	92	78	0.74	80	0.34
$E_T(\mathrm{jet2})$, $H_{\mathrm{T,miss}}$	0.04	91	82	0.75	73	0.31

Table 7.11: Fisher - Optimal cut selects fisher sum higher than the given cut value. $t\bar{t}$ rejected, signal kept and significance of cut also given.

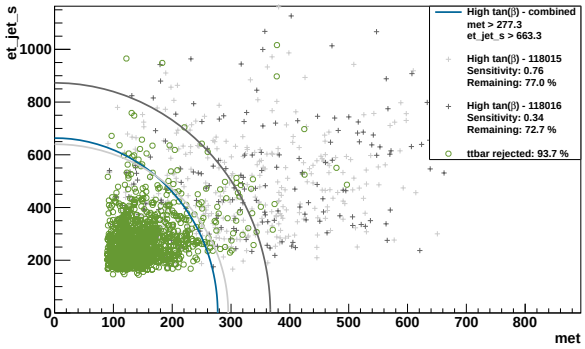

(a) $E_{\mathrm{T}}^{\mathrm{miss}}$vs $\sum |E_T(jets)|$ (GeV)

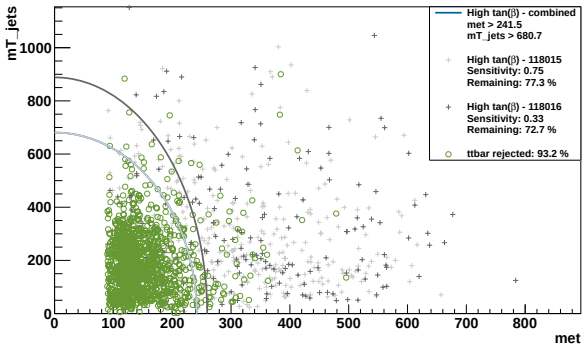

(b) $E_{\mathrm{T}}^{\mathrm{miss}}$vs $\mathrm{M}_T(jets)$ (GeV)

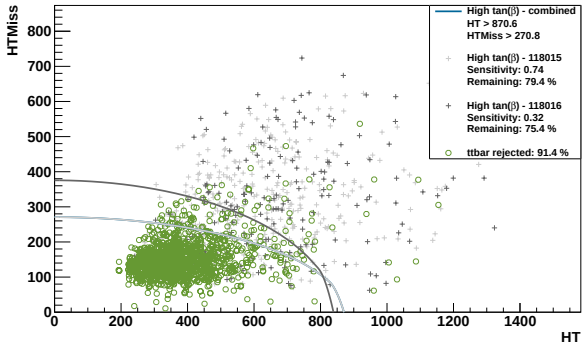

(c) H_T vs $H_{\mathrm{T,miss}}$ (GeV)

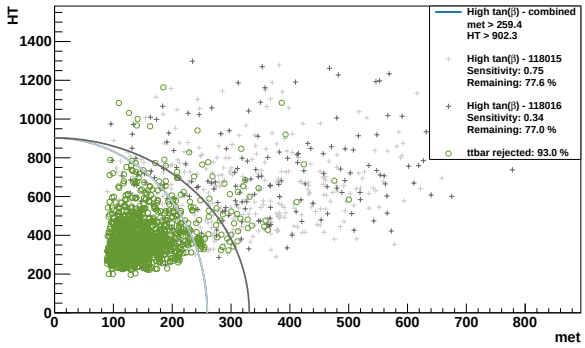

(d) $E_{\mathrm{T}}^{\mathrm{miss}}$vs H_T (GeV)

Figure 7.9: Elliptical cuts - Selected elliptical cuts. Cuts optimised for maximum significance at 35 pb^{-1}. Optimal ellipse for combination of high tan(β) models (dashed), and individual (gray).

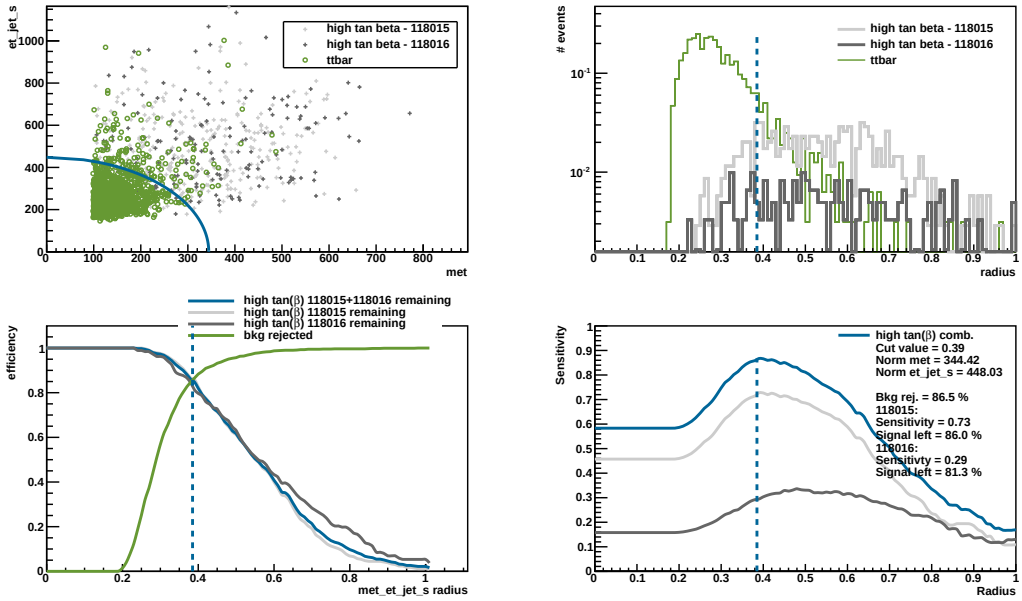

(a) $E_{\mathrm{T}}^{\mathrm{miss}}$ vs $\sum |E_T(jets)|$ (GeV)

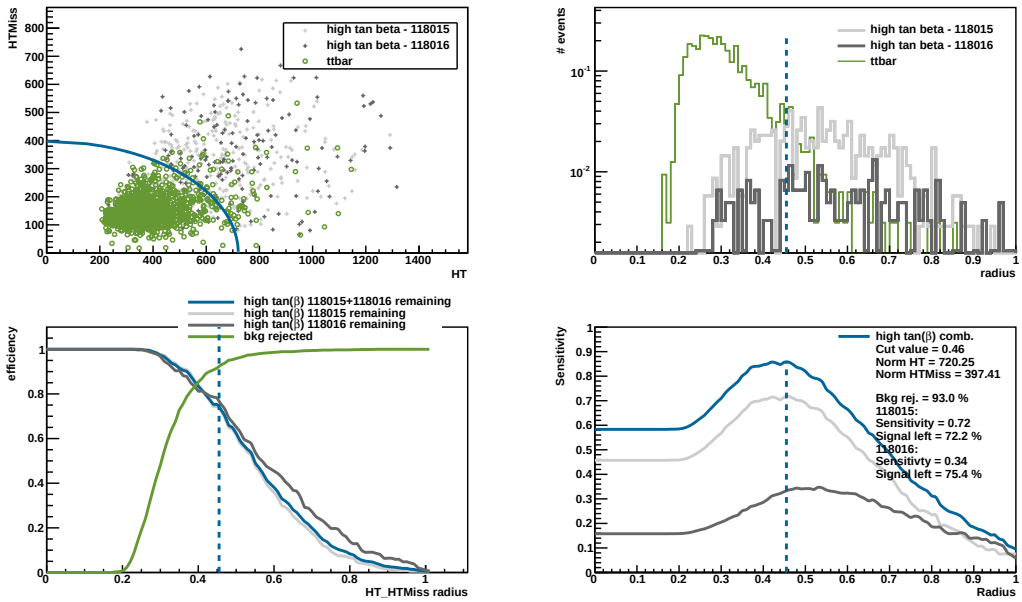

(b) H_T vs $H_{\mathrm{T,miss}}$ (GeV)

Figure 7.10: Radius cuts - Selected radius cuts. Cuts optimized for maximum significance at 35 pb^{-1}. Optimal cut values for the combination of high tan(β) models indicated by dashed lines.

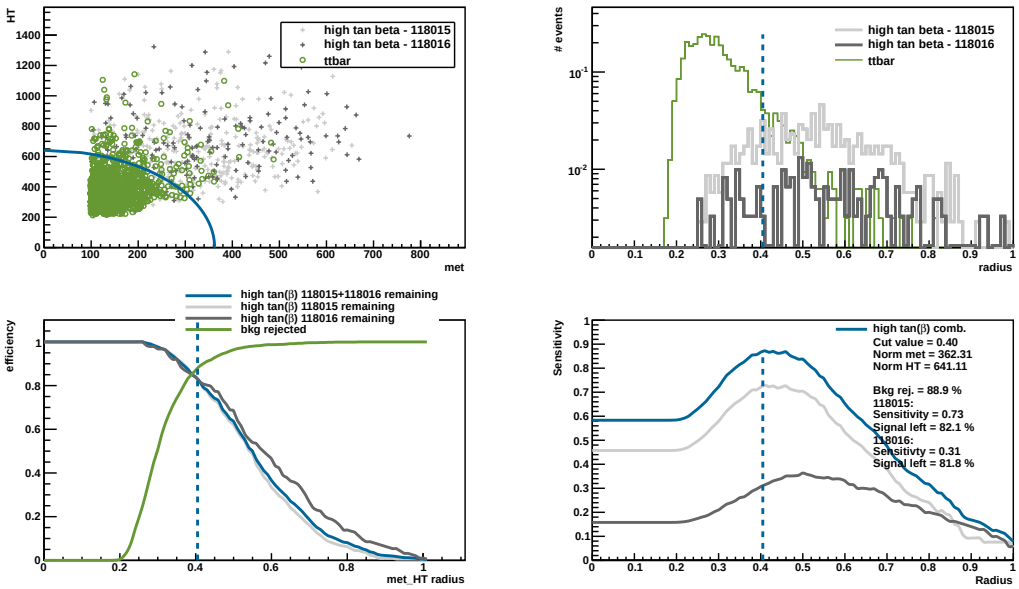

(a) $E_{\mathrm{T}}^{\mathrm{miss}}$vs H_T (GeV)

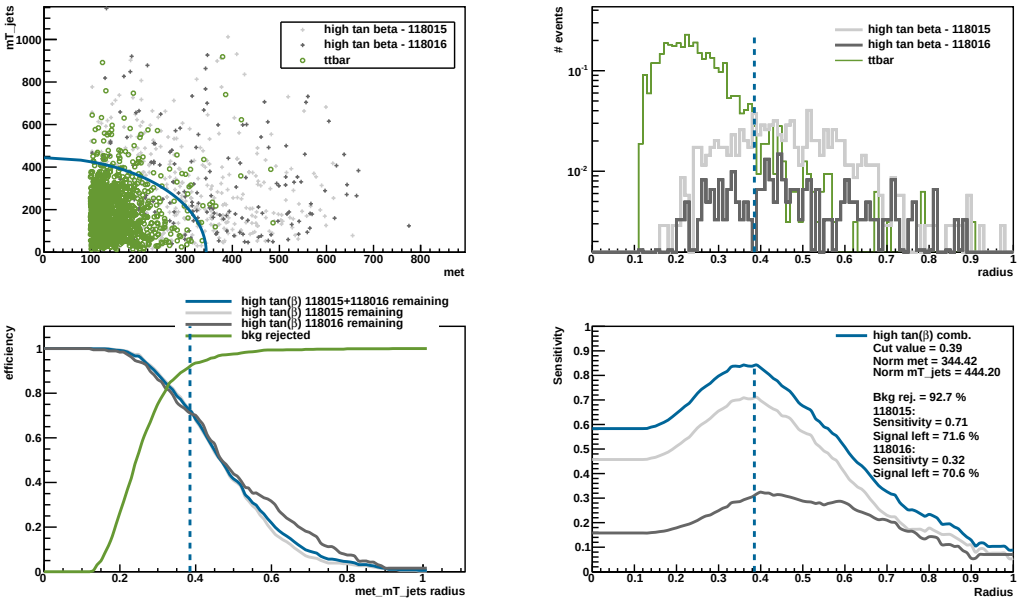

(b) $E_{\mathrm{T}}^{\mathrm{miss}}$vs $\mathrm{M}_T(jets)$ (GeV)

Figure 7.11: Radius cuts - Selected radius cuts. Cuts optimized for maximum significance at 35 pb^{-1}. Optimal cut values for the combination of high tan(β) models indicated by dashed lines.

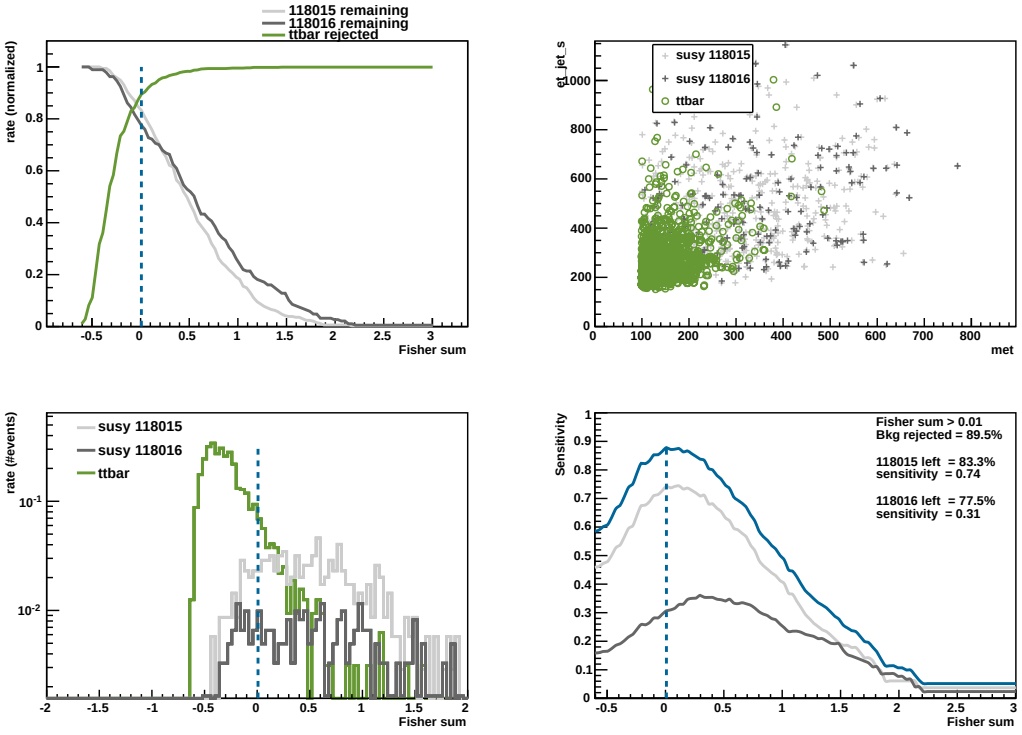

(a) $E_{\mathrm{T}}^{\mathrm{miss}}$vs $\sum |E_T(jets)|$ (GeV)

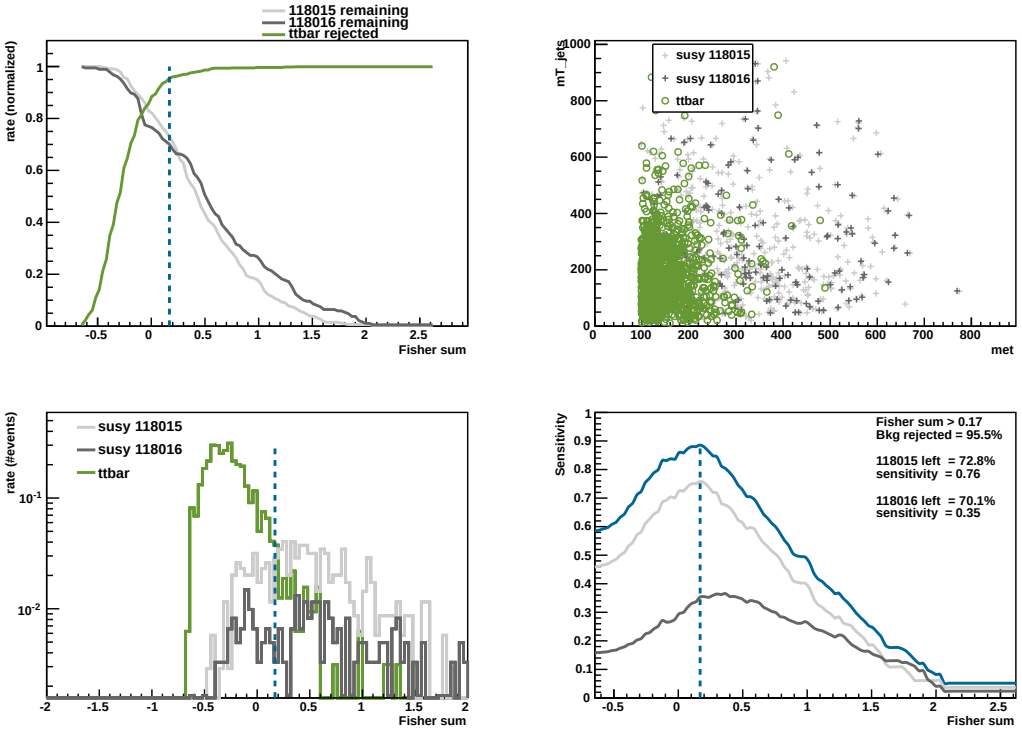

(b) $E_{\mathrm{T}}^{\mathrm{miss}}$vs $\mathrm{M}_T(jets)$ (GeV)

Figure 7.12: Fisher cuts - Selected fisher cuts. Cuts optimised for maximum significance of the fisher sum at 35 pb^{-1}. Optimal cut values for the combinations of high tan(β) models indicated by dashed lines. Top left: signal remaining and background rejected. Top right: distribution. Bottom left: Fisher sum. Bottom right: Significance

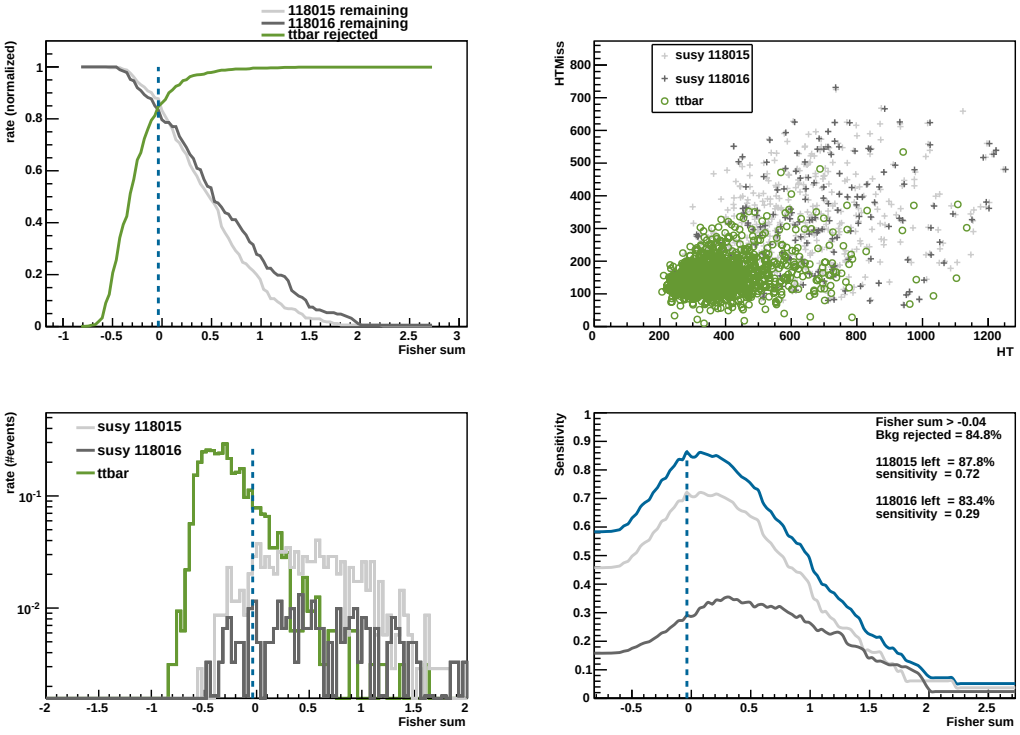

(a) H_T vs $H_{\mathrm{T,miss}}$ (GeV)

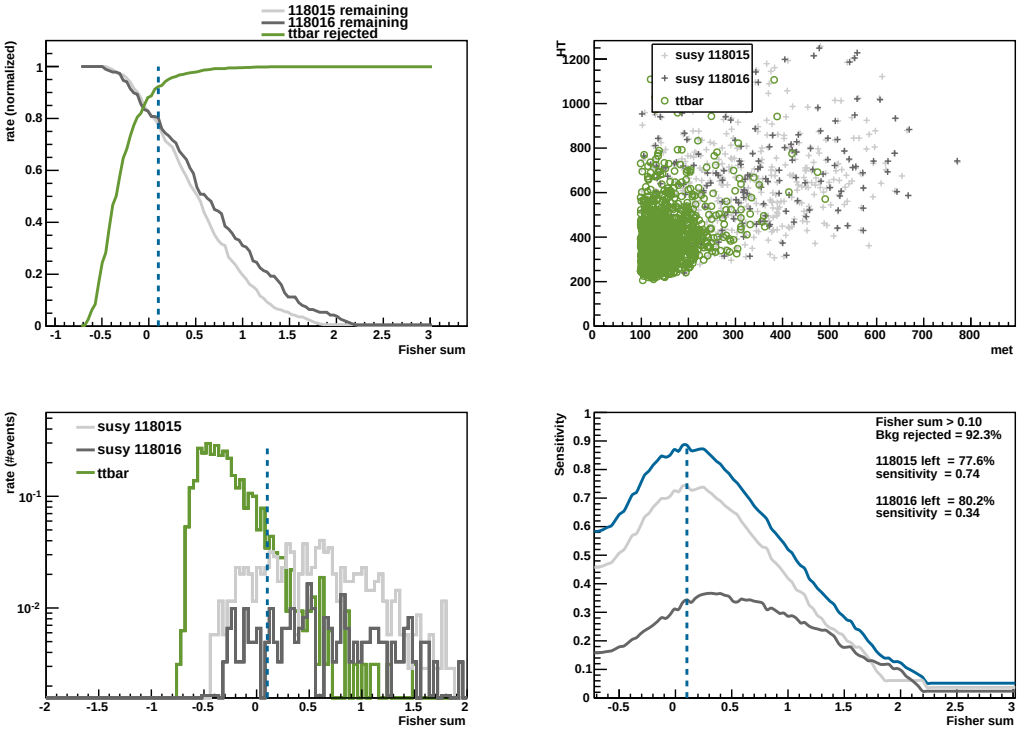

(b) $E_{\mathrm{T}}^{\mathrm{miss}}$vs H_T (GeV)

Figure 7.13: Fisher cuts - Selected fisher cuts. Cuts optimised for maximum significance of the fisher sum at 35 pb^{-1}. Optimal cut values for the combinations of high tan(β) models indicated by dashed lines. Top left: signal remaining and background rejected. Top right: distribution. Bottom left: Fisher sum. Bottom right: Significance

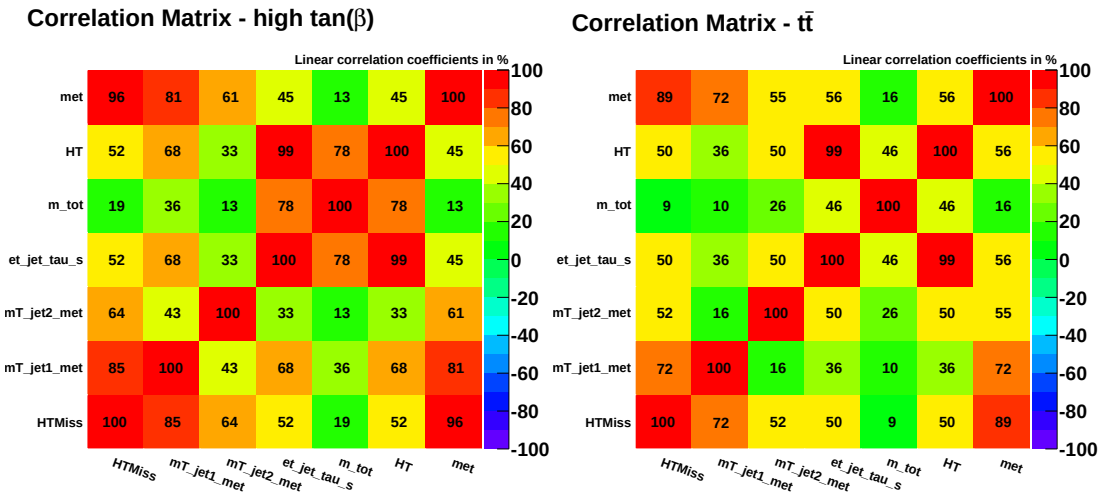

(a) High tan(β) **(b)** $t\bar{t}$

Figure 7.14: Correlation matrices for signal and background - Signal is the two high tan(β) models and background is $t\bar{t}$

is clear from some of the significance curves that some cut values could be chosen to be slightly lower to retain more signal in the cases where the peak is quite broad and no significant amount of significance is gained from cutting on exactly the maximum sensitivity.

Performing one of these cuts leaves too low statistics for making further cuts. Looking at the correlations between the different variables in Figure 7.14 shows that many of the variables with highest discriminatory powers are quite correlated. In other words performing another selection on one of the other highly correlated variables will not provide much improvement in separating signal from background processes.

7.7 Other Backgrounds

To compare predictions from MC simulations with data it is necessary to include other relevant backgrounds. This includes events consisting of W or Z bosons in addition to jets, pairs of bosons, WW, WZ and ZZ, commonly referred to as di-boson events. Lastly QCD also has to be taken into account. Applying the same selection criteria as for $t\bar{t}$ in addition to the elliptical cut on $E_{\mathrm{T}}^{\mathrm{miss}}$and $\sum E_T(jets)$ as optimised on $t\bar{t}$

events, on these samples yields the results shown in Figure 7.12. The elliptical cut removes large parts of $t\bar{t}$, W+jets, Z+jets and di-boson and QCD events. A significant fraction of QCD events still remain, with the contribution from QCD alone is larger than the other backgrounds combined (Table 7.13).

Cut	**118015**	**118016**	**SU4**	$t\bar{t}$
Total	28.79 ± 0.29	16.42 ± 0.16	2098 ± 9.4	3129 ± 3.1
Trigger	28.19 ± 0.29	16.17 ± 0.16	1327 ± 7.5	1134 ± 1.9
Jet Cleaning	27.51 ± 0.28	15.90 ± 0.16	1314 ± 7.4	1115 ± 1.9
Prim. Vertex	27.51 ± 0.28	15.90 ± 0.16	1314 ± 7.4	1115 ± 1.9
No crack e	27.43 ± 0.28	15.85 ± 0.16	1308 ± 7.4	1100 ± 1.9
No e	25.22 ± 0.27	14.84 ± 0.16	1155 ± 7.0	753.6 ± 1.5
No μ	23.47 ± 0.26	13.88 ± 0.15	1128 ± 6.6	491.0 ± 1.2
Jet high p_{T}	23.00 ± 0.26	13.65 ± 0.15	907.2 ± 6.2	310.8 ± 1.0
Jet low p_{T}	22.23 ± 0.25	13.15 ± 0.15	880.0 ± 6.1	304.1 ± 1.0
$E_{\mathrm{T}}^{\mathrm{miss}}$	20.91 ± 0.25	12.55 ± 0.14	677.4 ± 5.3	122.50 ± 0.62
Two τ	0.966 ± 0.053	0.308 ± 0.022	13.02 ± 0.74	3.49± 0.10
Ellipse	0.770±0.048	0.225± 0.019	3.49 ± 0.38	0.278±0.030
$\frac{E_{\mathrm{T}}^{\mathrm{miss}}}{\sum_{\mathrm{jets}}(E_{\mathrm{T}})+E_{\mathrm{T}}^{\mathrm{miss}}}$	0.720±0.046	0.212±0.019	3.36 ± 0.38	0.240±0.027
$\Delta\phi(jet1, E_{\mathrm{T}}^{\mathrm{miss}})$	0.717±0.046	0.211±0.019	3.36 ± 0.38	0.222±0.026
$\Delta\phi(jet2, E_{\mathrm{T}}^{\mathrm{miss}})$	0.667±0.044	0.211±0.019	2.98 ± 0.35	0.169±0.023

Table 7.12: Two tau selection all backgrounds - Shows the number of events after each selection criteria normalised to 35pb^{-1}.

There are several ways to reduce QCD background. One is increase the requirement on tau BDT for three prongs taus to 0.7, which would reject QCD as fewer events would pass the two tau selection. Other options includes cuts on $\frac{E_{\mathrm{T}}^{\mathrm{miss}}}{m_{\mathrm{Eff}}}$ and the angle between the jets in the events and the direction of $E_{\mathrm{T}}^{\mathrm{miss}}$ in the transverse plane, $\Delta\phi(jet, E_{\mathrm{T}}^{\mathrm{miss}})$. The latter is useful as $E_{\mathrm{T}}^{\mathrm{miss}}$in QCD events often come from mis-measured jets, which means that the $E_{\mathrm{T}}^{\mathrm{miss}}$will point in the direction of the jet. The first variable is useful as many QCD events pass the elliptical cut despite having only modest $E_{\mathrm{T}}^{\mathrm{miss}}$as the jet energy in the event is large, which corresponds to low values of $\frac{E_{\mathrm{T}}^{\mathrm{miss}}}{m_{\mathrm{Eff}}}$.

Cut values optimised for maximum significance with respect to the two high $\tan\beta$ samples and QCD are shown in Figure 7.16. The variable m_{Eff}, and consequently $\frac{E_{\mathrm{T}}^{\mathrm{miss}}}{m_{\mathrm{Eff}}}$, varies depending on the number of taus in an event. This is not desirable with

Cut	W+jets	Z+jets	di-boson	QCD
Total	153 308 ± 173	37 279 ± 59	849 ± 1.3	$366{\cdot}10^9$ ± $144{\cdot}10^9$
Trigger	2 967.5 ± 19.2	315.8 ± 5.3	94.96 ± 0.42	$4.45{\cdot}10^6$ ± $0.27{\cdot}10^6$
Jet Cleaning	2 899.6 ± 18.9	302.1 ± 5.2	93.70 ± 0.42	$4.43{\cdot}10^6$ ± $0.27{\cdot}10^6$
Prim. Vertex	2 898.9 ± 18.9	302.0 ± 5.2	93.63 ± 0.42	$4.43{\cdot}10^6$ ± $0.27{\cdot}10^6$
No crack e	2 888.7 ± 18.8	299.7 ± 5.2	91.65 ± 0.42	$4.43{\cdot}10^6$ ± $0.27{\cdot}10^6$
No e	2 704.6 ± 18.2	262.8 ± 4.8	45.32 ± 0.29	$4.39{\cdot}10^6$ ± $0.27{\cdot}10^6$
No μ	2 530.8 ± 17.6	217.6 ± 4.4	23.23 ± 0.21	$4.39{\cdot}10^6$ ± $0.27{\cdot}10^6$
Jet high p_{T}	1 366.3 ± 12.6	114.8 ± 3.2	11.58 ± 0.14	$2.12{\cdot}10^6$ ± $0.11{\cdot}10^6$
Jet low p_{T}	847.5 ± 9.1	84.2 ± 2.7	9.22 ± 0.13	$2.02{\cdot}10^6$ ± $0.11{\cdot}10^6$
$E_{\mathrm{T}}^{\mathrm{miss}}$	342.8 ± 5.8	16.6 ± 1.2	3.10 ± 0.08	6551 ± 157
Two τ	4.09±0.59	1.13±0.29	0.0204±0.0054	12.4± 4.5
Ellipse	0.71±0.24	0	0.0068±0.0034	1.32±0.46
$\frac{MET}{\sum_{\mathrm{jets}}(E_{\mathrm{T}})+E_{\mathrm{T}}^{\mathrm{miss}}}$	0.48±0.20	0	0.0050±0.0034	0.27±0.21
$\Delta\phi(jet1, E_{\mathrm{T}}^{\mathrm{miss}})$	0.48±0.20	0	0.0050±0.0034	0.25±0.21
$\Delta\phi(jet2, E_{\mathrm{T}}^{\mathrm{miss}})$	0.48±0.20	0	0.0050±0.0034	0.23±0.21

Table 7.13: Two tau selection all backgrounds - continued. Shows the number of events after each selection criteria normalised to 35pb^{-1}.

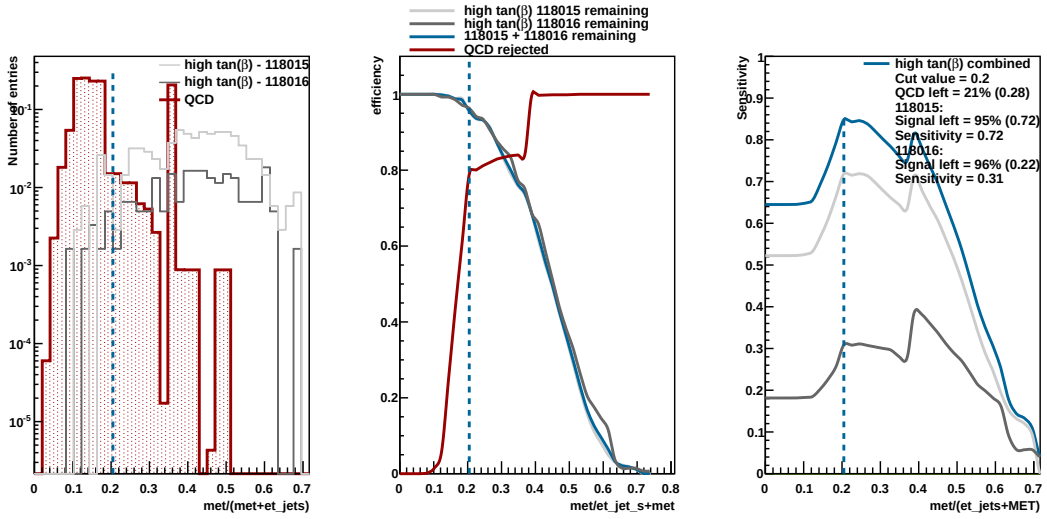

Figure 7.15: $\frac{E_{\mathrm{T}}^{\mathrm{miss}}}{\sum E_T(jets)+E_{\mathrm{T}}^{\mathrm{miss}}}$ - QCD removing cut. Individual high tan(β) models and combinations of the two. Left: variable distribution. Middle: Signal remaining and background rejected, Right: Significance

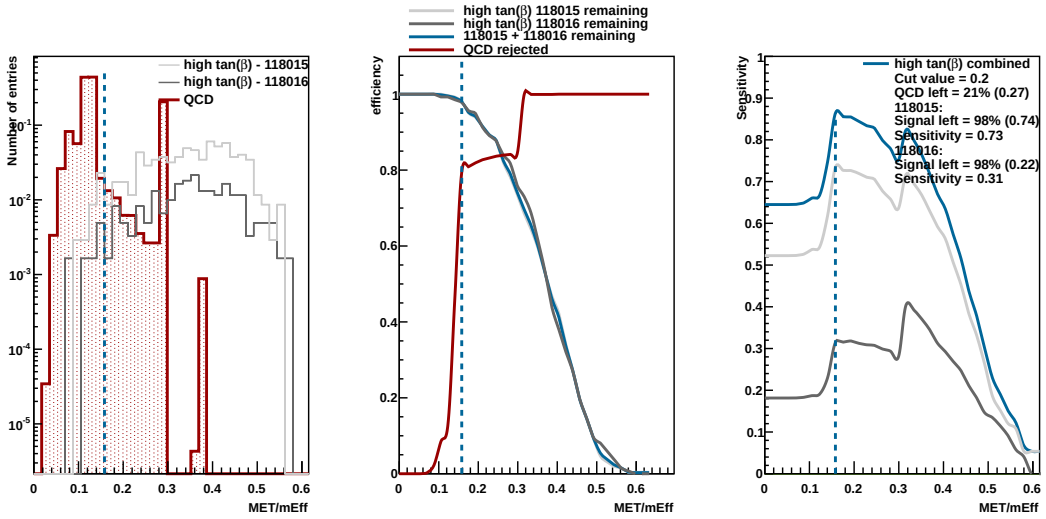

(a) $\frac{E_{\mathrm{T}}^{\mathrm{miss}}}{mEff}$

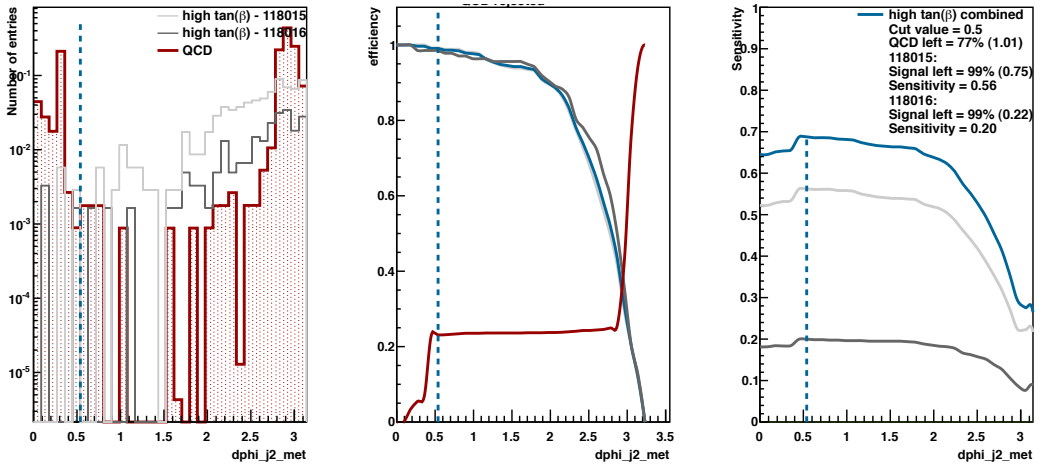

(b) $\Delta\phi(jet2, E_{\mathrm{T}}^{\mathrm{miss}})$

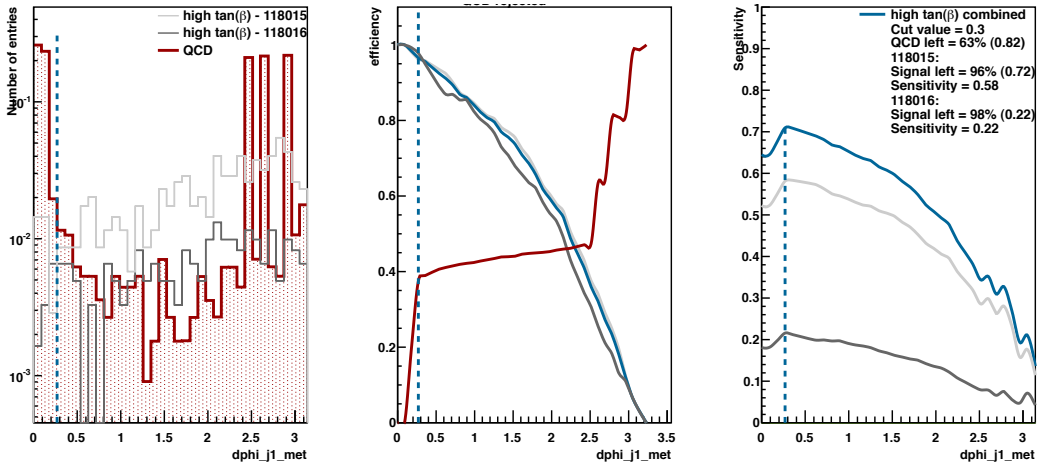

(c) $\Delta\phi(jet1, E_{\mathrm{T}}^{\mathrm{miss}})$

Figure 7.16: QCD reducing cuts - Left: Distribution. Middle: Signal left and QCD rejected. Right: Sensitivity of models with respect to QCD. Dashed line indicates maximum sensitivity.

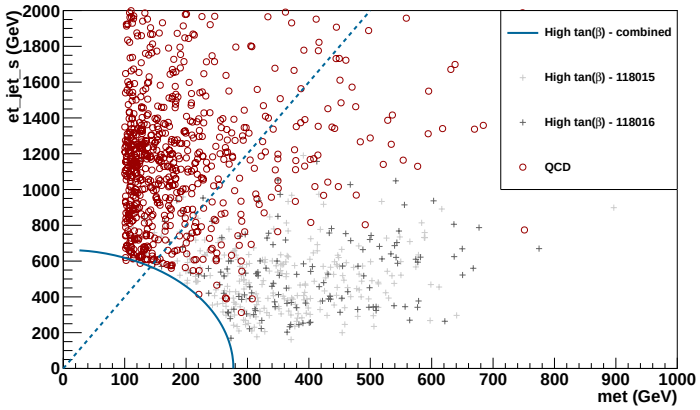

Figure 7.17: $E_{\mathrm{T}}^{\mathrm{miss}}$**vs** $\sum E_{\mathrm{T}}(jets)$ - After elliptical cut indicated by ellipse. Dashed line is $\frac{E_{\mathrm{T}}^{\mathrm{miss}}}{\sum E_T(jets)+E_{\mathrm{T}}^{\mathrm{miss}}} = 0.2$ indicating which regions passes this QCD-reducing requirement.

regards to the QCD background estimation to be made in the next chapter. Instead a selection can be made on $\frac{E_{\mathrm{T}}^{\mathrm{miss}}}{\sum E_T(jets)+E_{\mathrm{T}}^{\mathrm{miss}}}$ which is independent of the number of taus while still performing similarly to the above mentioned cut (Figure 7.15). A cut on $\frac{E_{\mathrm{T}}^{\mathrm{miss}}}{\sum E_T(jets)+E_{\mathrm{T}}^{\mathrm{miss}}} > 0.2$ is seen to remove 79% of the QCD background, while almost all of the two SUSY models remain after the elliptical cut. This criteria in combination with the elliptical cut can be seen for signal and QCD in Figure 7.17. The QCD events with relatively low $E_{\mathrm{T}}^{\mathrm{miss}}$, but high jet E_{T} is clearly shown to evade the elliptic cut. The dashed line indicates $\frac{E_{\mathrm{T}}^{\mathrm{miss}}}{\sum E_T(jets)+E_{\mathrm{T}}^{\mathrm{miss}}} = 0.2$. Applying this criteria to all the samples yield a total of expected SM contribution of 1±0.3, while 0.72±0.05 and 0.21±0.02 of the two SUSY models are expected at 35 pb^{-1}.

From the expected numbers of events at an integrated luminosity of 35 pb^{-1} for SM backgrounds and the SUSY models it is clear that no major conclusion can be drawn with this amount of data. By scaling the expected values by the integrated luminosity a rough sketch of the significance as a function of integrates luminosity can be made. This however does not take into account that tighter, and addition selection criteria, can be applied as larger statistics of MC simulations and data become available. Figure 7.18 shows such a sketch, where the selections in Table 7.12 has been applied. From this sketch an estimated amount of 3 fb^{-1} and 24 fb^{-1} integrated luminosity are required for a significance of 5 for 118015 and 118016 respectively. Although this amount of data is not currently available from the ATLAS experiment, a smaller amount of data

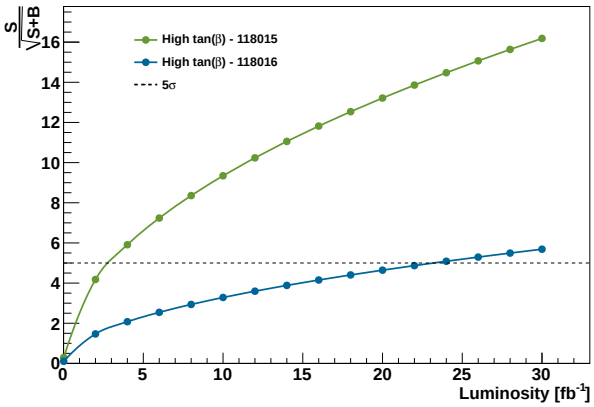

Figure 7.18: Significance as function of integrated luminosity - The graph shows a rough sketch of significance of the two SUSY models as a function of integrated luminosity after the selections in Table 7.12 are applied. The 5σ needed for discovery is indicated by the dashed line.

can be used to set limits on the production cross section of these models. In the next chapter the selections obtained in this chapter from MC simulations will be applied to ATLAS data, and predictions from these simulations will be compared to those of the data.

7.8 Determining Sparticle Masses

Once a possible SUSY signal has been discovered and enough statistics to investigate kinematics of the SUSY model has been accumulated, the sparticle masses of the model can be determined. In the case of an neutralino LSP, as in the high tan(β) models investigated here, there are no good mass peaks available for reconstruction due to the LSP escaping detection. Combinations of masses can however be measured by kinematic edges. When the second-lightest neutralino (χ_2^0) decays through a real slepton, which in our case is a stau ($\tilde{\tau}$)

$$\chi_0^2 \to \tau\tilde{\tau} \to \tau^+\tau^-\chi_1^0,$$

the resulting invariant mass of the two leptons is a triangle distribution with a sharp cut off as shown in Figure 7.19.

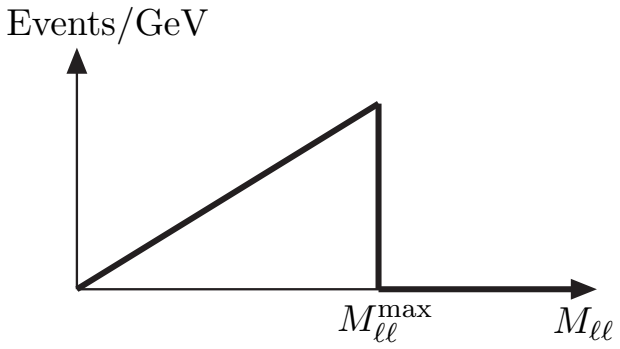

Figure 7.19: Dilepton invariant mass distribution - from events with $\chi_0^2 \to l\tilde{l} \to l^+l^-\chi_1^0$. No detector effects or cuts included. Figure taken from [21]

The endpoint of this distribution is at [21]

$$M_{\tau\tau}^{max} = m_{\chi_2^0}\left(1 - \frac{m_{\tilde{\tau}}^2}{m_{\chi_2^0}^2}\right)^{\frac{1}{2}}\left(1 - \frac{m_{\chi_1^0}^2}{m_{\tilde{\tau}}^2}\right)^{\frac{1}{2}} \tag{7.18}$$

Which with the masses given in Table 7.14 yields

$$M_{\tau\tau}^{max,118015} = 88.47 \text{ GeV} \qquad M_{\tau\tau}^{max,118016} = 65.29 \text{ GeV}. \tag{7.19}$$

The shape of this distribution will however be distorted by detection and measurement effects. But most importantly for taus it will be affected by the fact that the complete lepton momentum for taus is not reconstructed, due to the tau decaying into a neutrino which escapes detection. This distribution can be seen for true tau pairs in our two high tan(β) models and in the $t\bar{t}$ sample for opposite, same and combinations of both signed tau pairs in Figure 7.20 for taus with $p_T > 20$ GeV, $|\eta| < 2.5$ and with 1 or 3 prongs after the cuts in Table 7.6 are applied. The triangle shape is clearly visible for the two high tan(β) models.

Model	$M_{\chi_1^0}$ (GeV)	$M_{\chi_2^0}$ (GeV)	$M_{\tilde{\tau}}$ (GeV)
118015	124.15	231.45	141.85
118016	136.91	256.39	143.89

Table 7.14: High $\tan\beta$ **sparticle masses** - Two lightest neutralino and stau masses of the two high tan(β) models.

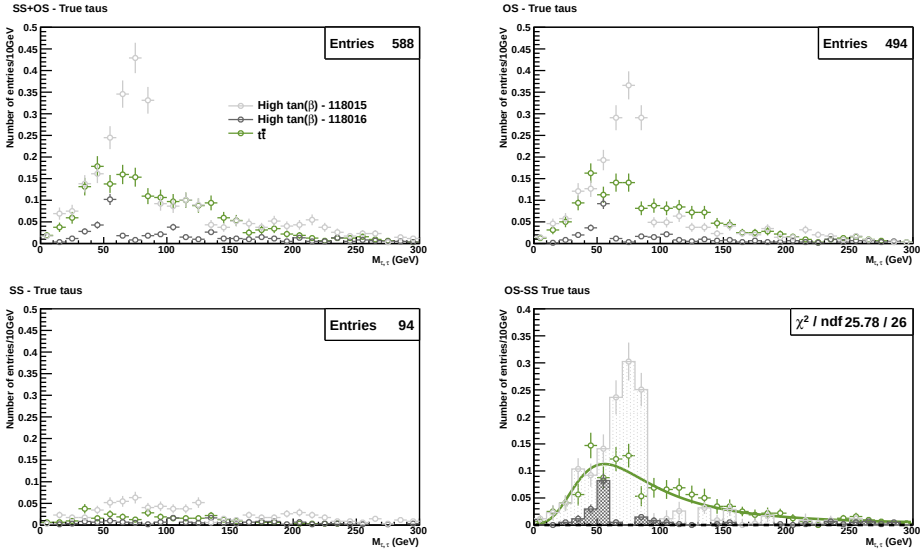

Figure 7.20: Invariant mass of true taus - In high tan(β) models and $t\bar{t}$. Top left: Combined distribution of opposite (OS) and same sign (SS) tau pairs. Top right: OS. Bottom left:SS. Bottom right: OS-SS. Green curve is a landau fitted to the $t\bar{t}$ distribution.

As the signal should yield only opposite signed tau pairs, and assuming that the background contributes equally to same and opposite signed tau pairs, the background can be subtracted by subtracting the same (SS) from the opposite signed (OS) distribution. The resulting invariant mass distributions are shown bottom right in Figure 7.20. Despite the low statistics for the two SUSY models they still show a triangle distributions that drops off sharply. The $t\bar{t}$ distribution has a wider peak as well as a slope that falls off less steeply. A fit to a landau function with a $\frac{\chi^2}{ndof}$ of 0.99 for the $t\bar{t}$ distribution is shown in Figure 7.20.

For true visible taus the peak is, as expected, shifted towards lower mass values due to the escaping neutrino 7.21. This also means that the upper endpoint is no longer clearly visible. It is however possible to determine the relation between the position of the peak and the endpoint theoretically, and therefor allowing the endpoint to be determined from measuring the position of the peak [46]. In addition the statistics are further reduced due to more taus being removed by the transverse momentum cut imposed, again due to the un-reconstructed neutrino from the tau.

Moving to reconstructed taus with the same quality criteria as imposed in the previous chapter the distributions in Figure 7.22 are obtained. A further reduction in

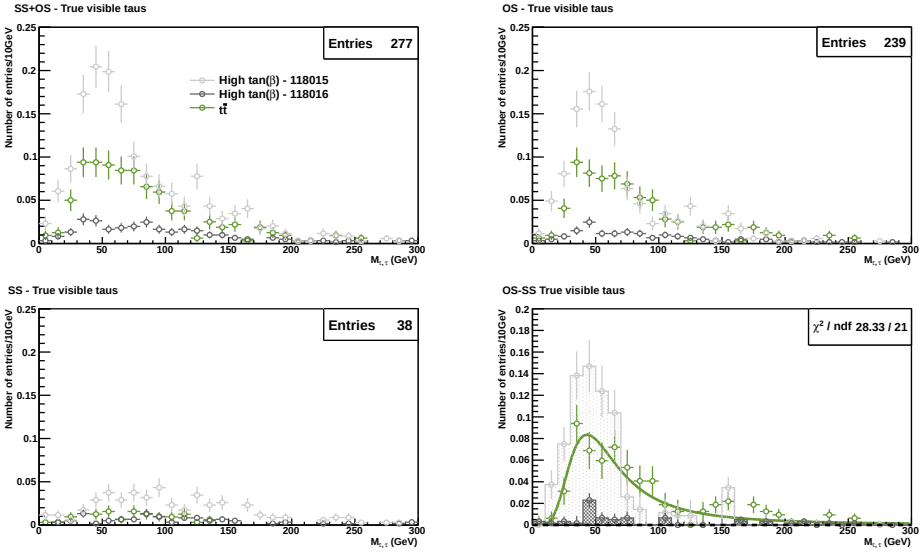

Figure 7.21: Invariant mass of true visible taus - In high tan(β) models and $t\bar{t}$. Top left: Combined distribution of opposite (OS) and same sign (SS) tau pairs. Top right: OS. Bottom left:SS. Bottom right: OS-SS. Green curve is a landau fitted to the $t\bar{t}$ distribution.

statistics is observed due to the effects of tau reconstruction, identification and quality criteria imposed in the previous section. This means that the invariant mass peak of model 118016 is completely lost. This is probably due to the fact that the softest tau has too low transverse momenta to be reconstructed for most events, consequently leading to fewer events with two reconstructed taus. The distribution for this model is consistent with zero, implying that the observed opposite sign events are mostly background events as well. The 118015 model still shows a peak, but it is however less pronounced than what is seen for the truth visible taus in addition to being lost in the background $t\bar{t}$ distribution.

Applying the elliptic cut on missing energy and the scalar sum of transverse energy of jets as found in Table 7.9 the distributions in Figure 7.23 is obtained. This cut removes large portions of the $t\bar{t}$ background, while most of the 118015 model is kept both number of events and shape of the distribution. The invariant mass peak of model 118015 is now clearly distinguishable from the $t\bar{t}$ distribution, which is shifted towards higher values and broadened compared to before the cut is made.

Including all backgrounds scaled to 35 pb^{-1} after the additional QCD selection is performed the distributions in 7.24 are obtained. The lack of statistics is now becoming

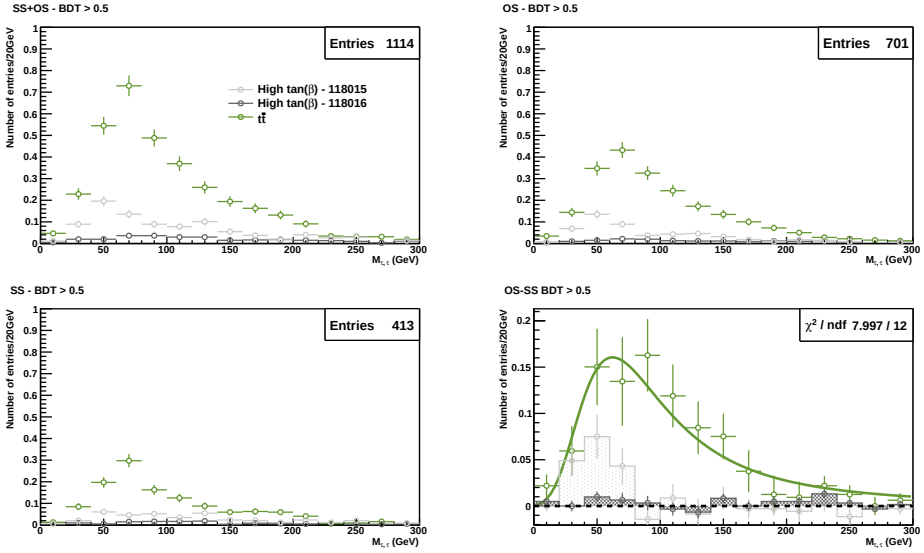

Figure 7.22: Invariant mass of reconstructed taus - High tan(β) models and $t\bar{t}$. Top left: Combined distribution of opposite (OS) and same sign (SS) tau pairs. Top right: OS. Bottom left:SS. Bottom right: OS-SS. Green curve is a landau fitted to the $t\bar{t}$ distribution.

apparent, with both W+jets and QCD yielding large peaks for single events. It is however clear that there will be contamination of the signal peak from both these backgrounds. W+jets will likely prove to be problematic as this background should have more opposite signed tau pairs, and be peaked around the W mass which is in the region of the peak of the SUSY models.

Taking a look at the y-axis in the histograms which are scaled to an integrated luminosity of 35 pb^{-1} tells us that performing an endpoint analysis on the current amount of available data is not viable. But the prospects look good for once larger amounts of data is collected. To improve the method opposite flavour, in addition to same sign, subtraction can be applied as the SUSY models predict only same flavour lepton pairs while background processes also contribute towards different flavour lepton pairs [21]. These distributions only gives the relation between the masses of different SUSY particles. In order to extract the individual masses other invariant mass distributions expressed by different combinations of the individual masses can be made, e.g. between squarks and sleptons. This is however beyond the scope of this thesis which aims to look for a possible SUSY model, rather than determining parameters of the model which require higher precision studies with more statistics.

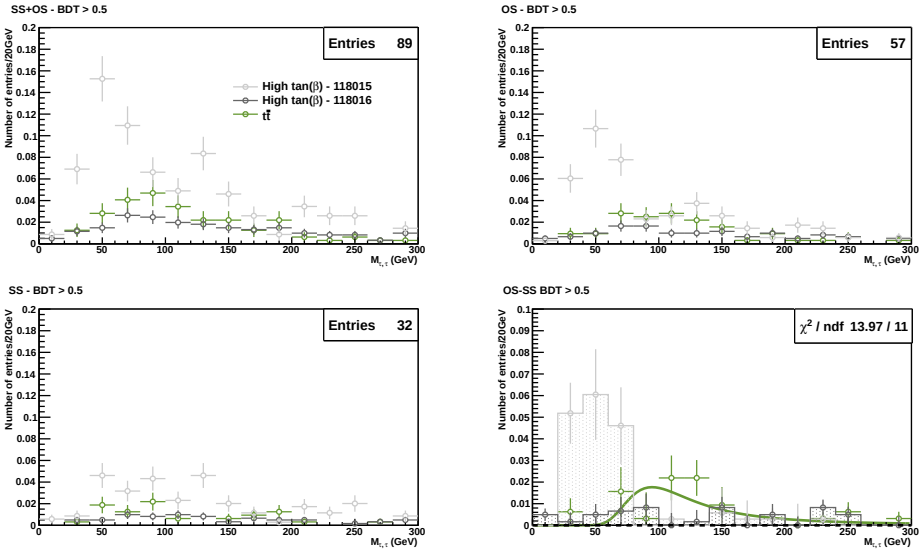

Figure 7.23: Invariant mass of reconstructed taus after elliptic cut - In high tan(β) models and $t\bar{t}$. Top left: Combined distribution of opposite (OS) and same sign (SS) tau pairs. Top right: OS. Bottom left:SS. Bottom right: OS-SS. Green curve is a landau fitted to the $t\bar{t}$ distribution.

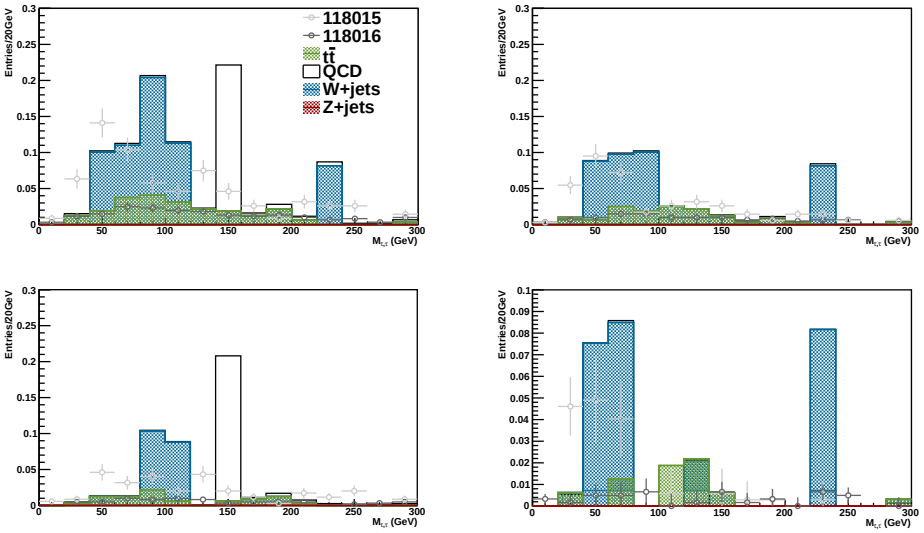

Figure 7.24: Invariant mass of reconstructed taus after elliptic and QCD cut - All backgrounds are included. Top left: Combined distribution of opposite (OS) and same sign (SS) tau pairs. Top right: OS. Bottom left:SS. Bottom right: OS-SS.

8

ATLAS Data

In this chapter ATLAS 2010 data will be analysed and compared to the MC predictions of the previous chapter. Methods to estimate QCD background from data will also be investigated, in order to be ready for data driven estimates once higher statistics are available through 2011 data. 2010 data corresponds to data from periods D-I where proton-proton collisions at 7 TeV centre of mass energy was recorded. In total an integrated luminosity of $37.5 \pm 1.3 \text{pb}^{-1}$ [47] was collected during this period. However, the amount of data available for analysis after a Good Run List (GRL) had been applied was $34.64 \pm 1.2 \text{pb}^{-1}$. The GRL requires that all the ATLAS detectors, magnet system and reconstruction algorithms are fully functioning in order for the data to be deemed suitable for analysis. [1]

8.1 QCD Background Studies

The previous parts of this thesis has relied heavily on the use of MC simulations. Although the uncertainties of these have not been considered, they are still present. Usually the shape of distributions in MC simulations are well modelled, while the scaling of the background is subject to a larger degree of uncertainty. Due to limited statistics only the QCD background will be investigated in this thesis. QCD is particularly important to investigate by a data driven approach. The real number of taus in QCD events are negligible, this means that the main part of the observed background in a

[1] Numbers and distributions have throughout this analysis been scaled to 35 pb^{-1}, due to the uncertainty on the integrated luminosity.

QCD dominated region containing taus is from fake taus. This fake rate is not well modelled in MC simulations. Additionally QCD is notoriously difficult to model due to large uncertainty on the production cross-section and $E_{\mathrm{T}}^{\mathrm{miss}}$ from instrumental effects.

The low statistics, only 20 data events after requiring two taus, makes a traditional ABCD control region approach unviable. Nevertheless, the scaling factor may be determined from data and compared to predictions from MC simulations. Combining this scale factor with some measure of the tau fake rate in QCD allows background estimates to be extrapolated from regions with high to low QCD contributions, i.e. the QCD dominated region with no taus, to the one containing taus. To this end control regions that are similar to the signal region but dominated QCD is defined, from which the scaling and fake tau contribution of QCD is determined.

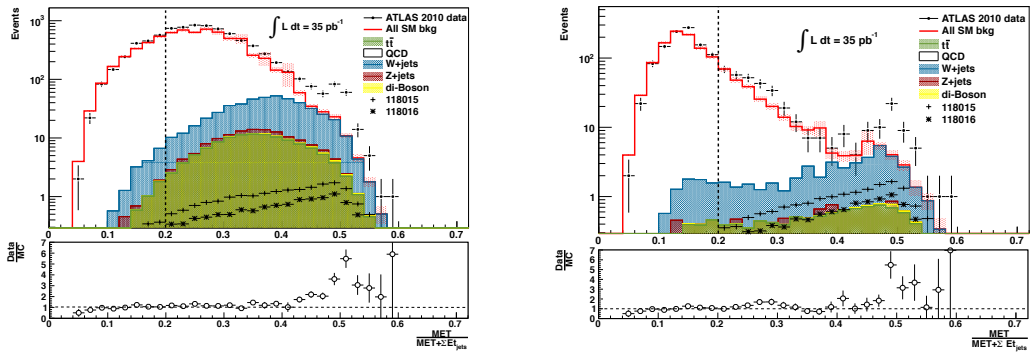

(a) Before elliptic cut

(b) After elliptic cut

Figure 8.1: Condition for QCD region - $\frac{E_{\mathrm{T}}^{\mathrm{miss}}}{\sum_{\mathrm{jets}} E_{\mathrm{T}} + E_{\mathrm{T}}^{\mathrm{miss}}} < 0.2$. No criteria on number of taus applied. Dashed line indicates selection value; separates QCD and signal region.

The signal region is defined to be the region passing all the cuts in Table 7.12, but with no selection on the number of taus. m_{Eff} in signal region for 0-, 1- and 2 taus are shown in Figure 8.4. The QCD control region is required to be dominated by QCD and separate from the signal region, while remaining as close as possible to the signal region in phase space. To this end the QCD selection criteria applied in the previous chapter are inverted to be separate from the signal region and dominated by QCD. All the other selection criteria applied in Table 7.12 are kept, except for the selection on numbers of taus. The QCD region (or *QCD-sidebands*) is consequently defined by

- Pass two tau cut-flow in Table 7.12 (except on variables below) but with no requirement on number of taus.
- $\frac{E_{\mathrm{T}}^{\mathrm{miss}}}{\sum_{\mathrm{jets}} E_{\mathrm{T}}+E_{\mathrm{T}}^{\mathrm{miss}}} < 0.2$.
- $\Delta\Phi(MET, jet1) < 0.5$ or $\Delta\Phi(MET, jet2) < 0.5$.

The region obtained by requiring $\frac{E_{\mathrm{T}}^{\mathrm{miss}}}{\sum_{\mathrm{jets}} E_{\mathrm{T}}+E_{\mathrm{T}}^{\mathrm{miss}}} < 0.2$ is shown in Figure 8.1, indicated by the dashed line, before and after the elliptical cut with no requirement on the number of taus. The data and MC are seen to agree for $\Delta\phi(E_{\mathrm{T}}^{\mathrm{miss}}, (jet))$ in the QCD sidebands (Figure 8.2). The discrepancies that are observed in Figure 8.1 will be discussed in Section 8.3. The QCD-region may further be split into regions with 0, 1 and 2 taus. Figure 8.3 shows m_{Eff} in the the 0-, 1- and 2 tau QCD region.

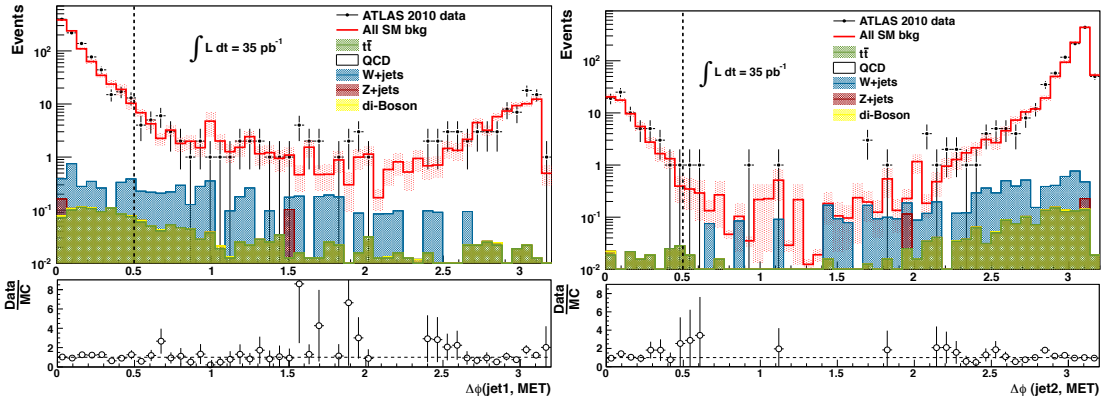

(a) $\Delta\Phi(E_{\mathrm{T}}^{\mathrm{miss}}, jet1)$ **(b)** $\Delta\Phi(E_{\mathrm{T}}^{\mathrm{miss}}, jet2)$

Figure 8.2: QCD-region - $\Delta\Phi(E_{\mathrm{T}}^{\mathrm{miss}}, jet)$.Shows QCD sidebands indicated by dashed lines at $\Delta\phi < 0.5$. Passes cutflow with inverted QCD cut and no number of taus selection.

8.1.1 MC Correction Factors

This section aims to investigate the QCD and fake tau background by a data driven method in analogy with the procedure used by the two tau analysis performed by SUSY with taus working group [48]. By defining control regions with zero and one tau, the QCD MC correction factor, ω_2 , in the two tau signal region may be determined. An overall MC correction factor is taken from the 0-tau sideband where statistics are highest. A fake rate correction factor is found from the 0- and 1-tau regions, assuming

that all the taus in QCD region are fake. The fake rate correction factor is assumed to be multiplicative and independent of the number of taus in an event. Both the fake rate and overall scale factor are assumed to be phase-space independent. This means that overall MC scaling correction in the signal region may be determined from the correction factors found in the QCD region.

Region	Taus	Data	QCD (MC)	Non-QCD (MC)
	0	948±30.8	890±15.0	2.4±0.37
QCD	1	32±5.7	45.9±4.6	0.46±0.15
	2	3±1.7	0.8±0.35	0.18±0.11
	0	335±18.3	222±8.0	31.3±1.46
Signal	1	38±6.2	14±1.6	11±0.87
	2	3±1.7	0.27±0.21	0.73±0.48

Table 8.1: Number of events in the QCD and signal regions - The number of events in the QCD regions is used to calculate the QCD scale factors in Table 8.2.

The overall QCD MC correction factor, ω_i, in the QCD region with i taus may be expressed as

$$\omega_i = \frac{N_{i,\tau}^{data} - N_{i,\tau}^{nonQCD}}{N_{i,\tau}^{QCD}}, \tag{8.1}$$

where i is the number of taus in the sideband, $N_{i,\tau}^{data}$ is the number of data events in the i-tau sideband, while $N_{i,\tau}^{nonQCD}$ and $N_{i,\tau}^{QCD}$ is the number of non-QCD and QCD MC events in this sideband respectively. Due to low statistics and consequently large uncertainties, this value is not obtainable from the two tau region directly. A fake rate correction factor to MC, f, may be obtained from the 1-tau and 0-tau sideband

$$f = \frac{\omega_1}{\omega_0} = \frac{N_{1\tau}^{data} - N_{1\tau}^{nonQCD}}{\omega_0 \cdot N_{1\tau}^{QCD}}. \tag{8.2}$$

This factor represents the difference in fake rate between MC and data. The total QCD MC correction factor in the 2-tau region, ω_2, may consequently be approximated by

$$\omega_2^* = \omega_0 \cdot f^2. \tag{8.3}$$

An useful crosscheck for this value is to compare it to the scaling factor for the two tau QCD sideband, ω_2 , computed directly. Where $\omega_2 = \omega_2^*$ within the accuracy of the experiment would indicate that the assumptions made for f, being independent of

number of taus in the region, are valid. Unfortunately low statistics make this cross check difficult by the large uncertainty on this value as shown in Table 8.2, ω_2 is however found to be consistent with ω_2^* within 2σ. The tau identification criteria could however be loosened to perform this check [48]. This is however beyond the scope of this thesis. Table 8.1 shows the number of data, QCD MC and non-QCD MC in the QCD region used to calculate the correction factors in Table 8.2. Assuming that f and ω_0 are phase

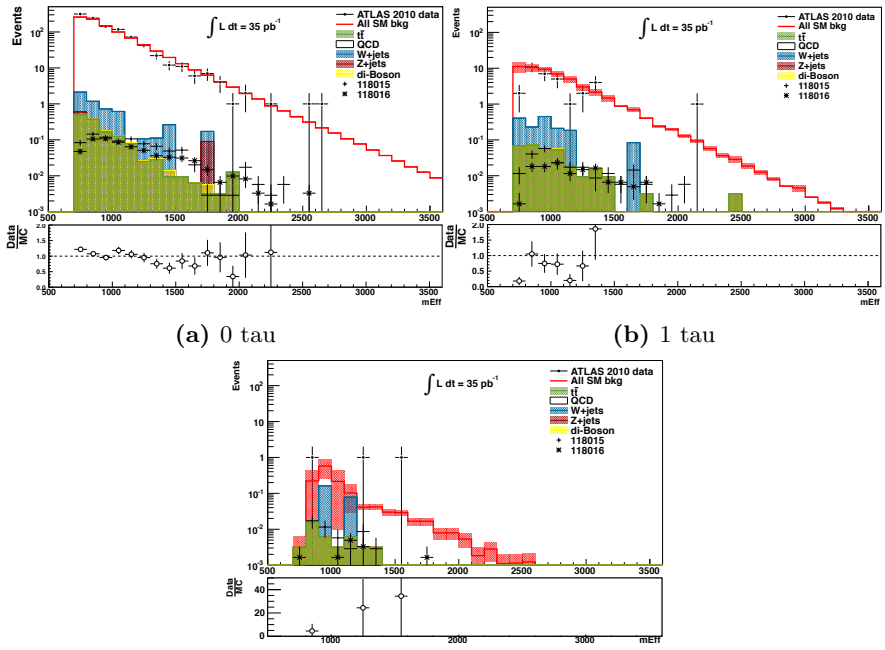

(a) 0 tau **(b)** 1 tau

(c) 2 tau

Figure 8.3: m_{Eff}(GeV) **QCD-region** - for 0-, 1- and 2 taus. Top plot shows the distribution, bottom depicts the ratio of data to MC. Dashed line at $\frac{data}{MC} = 1$. Errors on MC is indicated by red dotted rectangles.

space independent, the correction factor in the signal region may be taken to be the same as in the two tau QCD region. Thus the overall MC correction factor in the signal region is found to be $\omega_2 = 0.45 \pm 0.19$.

By applying this scale factor to the number of QCD MC in the signal region with two taus (from Table 7.13), an estimated number of 0.10±0.10 QCD events are expected in the signal region. This assumption might not be valid as the scaling factor is expected to be phase space dependent. This factor may however not be determined from the signal region, with zero or one tau, as these regions will contain signal as well due to a

large fraction of taus failing reconstruction or our object definition as shown in Figure 8.4 and Table 8.1. A problem of this method is that it relies on number of MC QCD events in the two tau signal region. Due to low statistics this number of events is subject to large uncertainties. The distributions for m_{Eff} in the QCD region for zero, one and

ω_0	f	ω_2^*	ω_2
1.06±0.04	0.65±0.14	0.45±0.19	3.54±2.69

Table 8.2: QCD correction factors - obtained from the QCD region.

two taus are shown in figures 8.3. Due to low statistics this method can not currently be relied upon to provide accurate results. It should rather be regarded as a possible method to estimate QCD scaling once statistics increase and all MC are included.

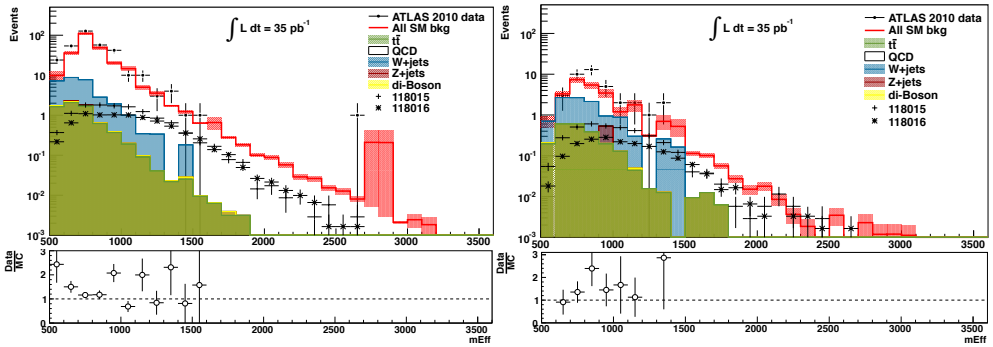

(a) 0 tau

(b) 1 tau

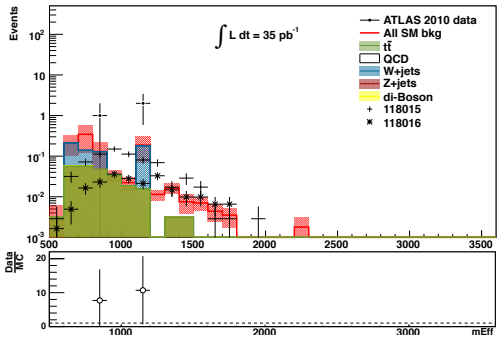

(c) 2 tau

Figure 8.4: $mEff$(GeV) **signal region** - for 0, 1 and 2 taus. Top plot shows the distribution, bottom depicts the ratio of data to MC. Dashed line at $\frac{data}{MC} = 1$. Errors on MC is indicated by red dotted rectangles.

8.1.2 Correction Factor and Fake Rate

This section aims to investigate an alternative procedure to estimate the QCD background in the signal region, the region passing all cuts and containing two taus, directly from the QCD region. This is desirable to avoid the large uncertainties on the number of MC QCD events in the signal region. The overall correction factor on QCD MC is assumed to be the same in the QCD and signal region with zero taus. The fake rate, f_{rate}, is taken to be independent of the number of taus in an event and phase space dependent and is calculated from data and non-QCD MC. The number of QCD events in the signal region may then be estimated by

$$\begin{aligned} N^{2,\text{signal}}_{\text{Est.,QCD}} &= N^{0,\text{signal}}_{\text{QCD}} \cdot \omega_0 \cdot f^2_{\text{rate}} \\ &= N^{0,\text{signal}}_{\text{QCD}} \cdot \omega_0 \cdot \left(\frac{N^1_{\text{data}} - N^1_{\text{non-QCD}}}{N^0_{\text{data}} - N^0_{\text{non-QCD}}} \right)^2 , \end{aligned} \tag{8.4}$$

where $N^{0,\text{signal}}_{\text{QCD}}$ is the number of QCD MC events in the signal region but with zero taus, N_{data} and $N_{\text{non-QCD}}$ is the number of data and non-QCD MC in the QCD region respectively. From the observed numbers shown in Table 8.1 the number of events in the signal region with two taus is estimated to be $N^{2,\text{signal}}_{\text{Est.,QCD}} = 1.1 \pm 0.4$. This method does not rely on the QCD MC in the signal region which has low statistics. Neither does it calculate a fake rate correction factor to be applied to QCD MC, but rather calculates the fake rate directly from data in the QCD region. This should make this method less dependent on the uncertainties in QCD MC than the approach in the previous section. This approach yields an estimated QCD in the signal region 2.4σ from that obtained in the previous section. It should be emphasised that these estimations are more investigations of procedures, rather than producing accurate results with the current statistics. A comparison between MC predictions and data will be made in the next section.

8.2 Comparing Data with MC Simulations

The expected number of events after applying the two tau selection described in Chapter 7 is shown in Table 8.3. The final number for the combined SM background is for QCD MC without any scaling applied. A total of 0.72±0.05 and 0.21±0.02 events are expected for the high $\tan\beta$ points 118015 and 118016 respectively after the the cut

Cut	118015	118016	SM	Data
$E_{\mathrm{T}}^{\mathrm{miss}}$	20.91 ± 0.25	12.55 ± 0.14	7035 ± 156.9	8266 ± 90.9
Two τ	0.9663 ± 0.053	0.3075 ± 0.022	21.13 ± 4.53	20 ± 4.5
Ellipse	0.770 ± 0.048	0.225 ± 0.019	2.31± 0.52	6 ± 2.45
$\frac{E_{\mathrm{T}}^{\mathrm{miss}}}{\sum_{\mathrm{jets}} E_{\mathrm{T}}+E_{\mathrm{T}}^{\mathrm{miss}}}$	0.720 ± 0.046	0.212 ± 0.019	0.99 ± 0.29	3 ± 1.7
$\Delta\phi(jet1, E_{\mathrm{T}}^{\mathrm{miss}})$	0.717±0.046	0.211±0.019	0.953±0.285	2±1.4
$\Delta\phi(jet2, E_{\mathrm{T}}^{\mathrm{miss}})$	0.667±0.044	0.211±0.019	0.88±0.285	0

Table 8.3: Two tau selection SUSY, SM and data - Shows the number of events after each selection criteria normalised to 35pb^{-1}. The errors are statistical.

on $\frac{E_{\mathrm{T}}^{\mathrm{miss}}}{E_{\mathrm{T}}^{\mathrm{miss}}+\sum E_T(\mathrm{jets})}$. Expected number of events from the SM processes considered is 1±0.3 and observed number of data events is 3±1.7 after the cut on $\frac{E_{\mathrm{T}}^{\mathrm{miss}}}{E_{\mathrm{T}}^{\mathrm{miss}}+\sum E_T(\mathrm{jets})}$, which is consistent ($1.2\sigma$) with the SM predictions. Applying the two requirements on $\Delta\phi((jet), E_{\mathrm{T}}^{\mathrm{miss}})$ yields an expected SM background of 0.9±0.3, and no remaining data events. As comparable numbers of events are expected for the point 118015 and SM processes are expected it should be possible to or set limits on the cross section of this SUSY point, or exclude it altogether once more statistics become available. As of today 480.8 pb^{-1}of data has been collected, where about 150 pb^{-1}has been collected the last week alone [49]. This rapid increase in the integrated luminosity will allow for more accurate predictions in the near future.

8.3 Further Considerations

There is an apparent excess in the data at about 0.5-0.6 in figures 8.1 and 8.6. A systematic overestimation of data with respect to MC in the $E_{\mathrm{T}}^{\mathrm{miss}}$ distribution before the elliptical cut Figure 8.5 is also observed. Both these features are however limited to the case of zero taus as can be seen in Figure 8.5b compared to figures 8.5c and 8.5d for $E_{\mathrm{T}}^{\mathrm{miss}}$ and in figures 8.6a, 8.6b and 8.6c. The systematic overestimation of $E_{\mathrm{T}}^{\mathrm{miss}}$ together with this excess being located where electroweak processes dominated over that of QCD indicates that this discrepancy may be due to electroweak process not included this study. It is natural to assume that the difference between data and MC are from W processes that has not been included in the MC simulations. Specifically W bosons decaying into electrons and muons along with jet production has not been

considered. When the leptons are not identified or in a p_{T} and η region other than that defined by the object definition the events pass the electron and muon vetoes. This yields contributions mostly in the zero tau region assuming the rate of electrons and muons faking taus are small. This should explain why the effect is only seen for the distribution with no taus, the position of the discrepancy along with the systematic overestimation of $E_{\mathrm{T}}^{\mathrm{miss}}$ which arises from the neutrinos in the W decay. Due to time limitations a further investigation of this discrepancy will not be made in this analysis.

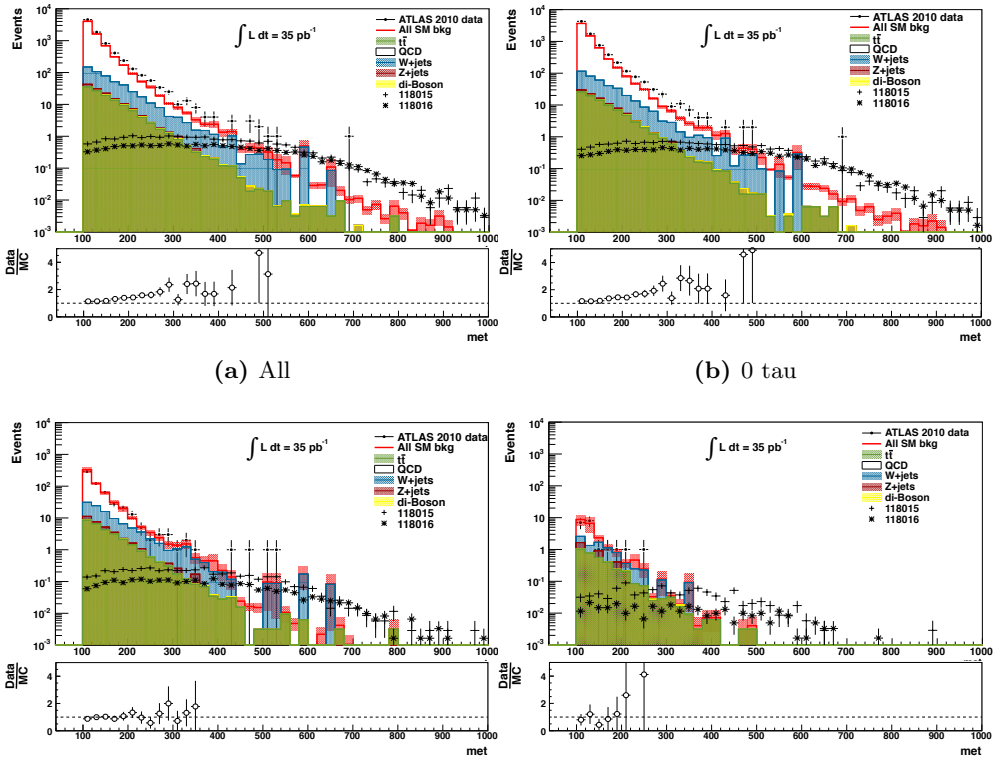

(a) All **(b)** 0 tau

(c) 1 tau **(d)** 2 tau

Figure 8.5: $E_{\mathrm{T}}^{\mathrm{miss}}$ (GeV) after $E_{\mathrm{T}}^{\mathrm{miss}}$ selection criteria - Top plot shows the distribution, bottom depicts the ratio of data to MC. Dashed line at $\frac{data}{MC} = 1$. Errors on MC is indicated by red dotted rectangles.

The excess and overestimation should not present a major source of error in the two tau analysis as it is located in the regions with no taus. The main implication of this discrepancy is for the QCD estimation of the previous section. As the overall scale factor is taken from the signal like region with no taus. Including all the W boson MC

simulations should therefore yield a lower overall scale factor, ω_0, and consequently a lower total scale factor, ω_2 and less estimated QCD in the signal region.

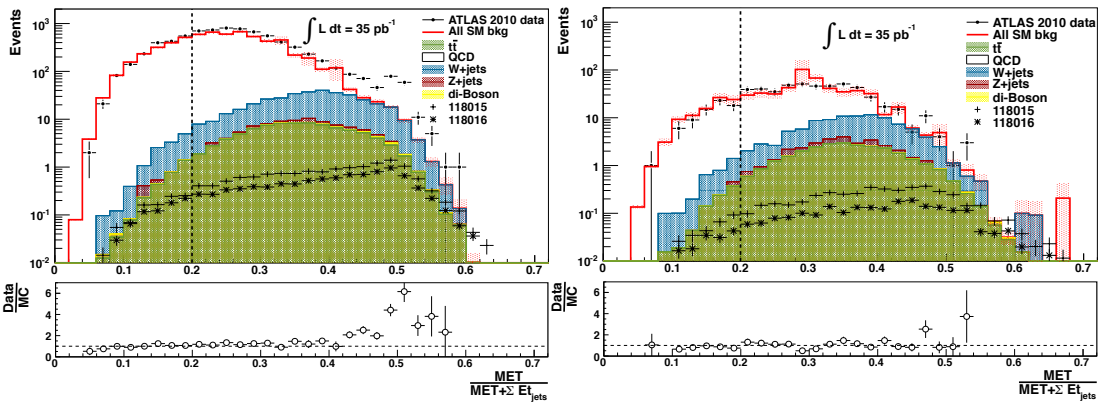

(a) 0 tau

(b) 1 tau

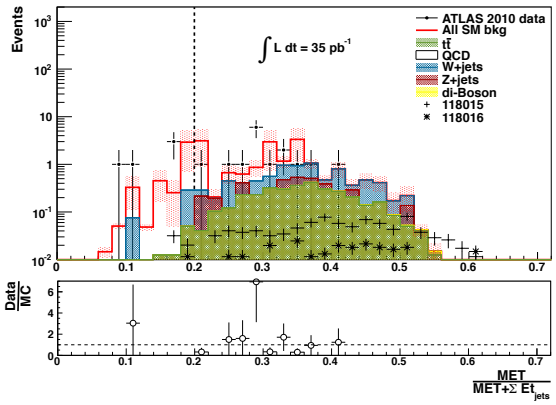

(c) 2 tau

Figure 8.6: $\frac{E_{\mathrm{T}}^{\mathrm{miss}}}{\sum_{\mathrm{jets}} E_{\mathrm{T}}+E_{\mathrm{T}}^{\mathrm{miss}}}$ - for zero, one and two taus after $E_{\mathrm{T}}^{\mathrm{miss}}$ cut. Top plot shows the distribution, bottom depicts the ratio of data to MC. Dashed line at $\frac{data}{MC} = 1$. Errors on MC is indicated by red dotted rectangles.

It should also be mentioned that a requirement on the matching of the muon track in the muon system and inner detector should be applied following the recommendations for release 15 MC simulations and data. As this criteria is not applied in this analysis, more muons are selected than what is recommended. The missing energy is manually corrected for the muons selected before the isolation requirement on the muons is applied. Consequently the missing energy should be slightly higher in some events than if the matching criteria was applied. This effect is however expected to be negligible

as the matching criteria is not very strict and the corrections to the missing energy are small. Events containing isolated muons are vetoed meaning that more events are vetoed without the matching criteria applied. This effect should also contribute equally to data and MC simulations. Jet cleaning was also applied to MC simulations, rather than the recommended 0.97 scale factor. This effect is also assumed to be negligible. A detailed study of systematic effects influencing the analysis is beyond the scope of this thesis. The main systematics uncertainties are

- Jet energy scale (JES) [40]
- Jet energy resolution (JER) [50]
- Luminosity [47]
- MC generator uncertainties [36]
- Tau efficiency and fake rate uncertainty [48]

The Jet energy scale and resolution are detector uncertainties related to the energy and resolution measurement of jets. This is important for this analysis as it relies on measurements of high energy jets. It also affects $E_{\mathrm{T}}^{\mathrm{miss}}$, as most of the $E_{\mathrm{T}}^{\mathrm{miss}}$ in QCD events comes from the mis-measurement of jets and hence fake $E_{\mathrm{T}}^{\mathrm{miss}}$. The JES uncertainty has been estimated to be smaller than 10% for jets with $p_{\mathrm{T}} > 2.8$ and $|\eta| < 2.8$ [40], while JER was found to be well described by MC simulations within 14%. Current uncertainties on the luminosity are estimated to 3% [47]. Uncertainties on MC simulations include uncertainties in PDF and overall scaling. The tau efficiency and fake rate uncertainty is assumed to be 30% and 20% respectively [48]. Uncertainties from trigger efficiencies along with electron and muon identification efficiencies are expected to be small. Under the naive assumption that one can estimate the total systematic using the sum of the errors in quadrature the total systematic would be $\sim$35%. A careful study of the influence of each error the measured quantities would have to be conducted to give a reliable estimate of the total systematic error.

9

Summary and Conclusion

In this thesis the discovery potential for mSUGRA in the co-annihilation region with final states containing two taus at the ATLAS detector has been investigated. The theoretical foundation of the SM was presented along with the problems this theory leaves un-explained in Chapter 2, in particular the problem of not providing a suitable DM candidate. The concept of SUSY and its solution to the unsolved problems of the SM were described in Chapter 3. The mSUGRA model in the co-annihilation region was found to provide a DM candidate in the neutralino. Chapter 4 describes the ATLAS experiment, and how possible new, heavy particles from proton-proton collisions may be detected in the ATLAS detector. As the final state of interest in this study contains tau leptons the reconstruction and identification of taus in ATLAS was investigated and tau identification and selection requirements were found in Chapter 5. The reconstruction efficiency of hadronically decaying taus in the $t\bar{t}$ sample was found to be on average 95% for taus with $p_{\mathrm{T}}>$ 15 GeVand $|\eta| < 2.5$. Applying identification algorithms, cut based ID or BDT ID, and additional requirements on the charge and number of tracks of the tau was found to reduce the reconstruction efficiency but improve the purity of the selected taus. The BDT tau ID was also found to perform better than the cut based ID. In Chapter 6 MC simulations of one of the main backgrounds of SUSY, $t\bar{t}$, were studied. The top quark mass was attempted reconstructed using the collinear approximation. It was however found that this approximation does not hold for most $t\bar{t}$ events, leading to low efficiency and accuracy of the method.

In Chapter 7 a MC study of SUSY was performed. Baseline event preselection and object definitions was found and cross-checked with those of the 0-lepton SUSY

working group at ATLAS. Two tau rich mSUGRA points in the co-annihilation regions satisfying experimental constraints were found from the ATLAS high $\tan\beta$ grid and used in the further analysis. Different ways to separate $t\bar{t}$ from SUSY events were investigated. This included selection criteria on single variables, and two dimensional selections by performing elliptical cuts,'radius' cuts and using two dimensional linear Fisher discriminant analysis. It was found that the conceptually simple elliptic cut performed almost as well as the Fisher discriminant analysis, so the elliptic cut was chosen for further analysis. The even simpler radius cut performed worse than the other two methods. An elliptical cut was applied to other relevant SM backgrounds and the selected SUSY points. An additional cut was found and applied to reduce contribution from QCD background. End-point distributions for $M_{\tau\tau}$ in the SUSY and SM samples was investigated to determine the prospect of finding the relations between the sparticle masses of the two SUSY points.

In Chapter 8 MC predictions for the two mSUGRA points in addition to SM processes were compared with data from the ATLAS experiment corresponding to an integrated luminosity of 35 pb^{-1}. Results were found to be consistent with SM predictions. Z+jets and di-bosons was found to not contribute significantly to the SM background, with 0 and 0.005±0.003 expected events respectively at 35 pb^{-1}. The dominant background processes were W+jets, $t\bar{t}$ and QCD. The two selected mSUGRA models were found to yield less signal events than the SU4 low mass benchmark point. A total of 1±0.3 SM events, and 0.7±0.05 and 0.2±0.02 events are expected for the two mSUGRA models in 2010 data after the cut on $\frac{E_{\mathrm{T}}^{\mathrm{miss}}}{E_{\mathrm{T}}^{\mathrm{miss}}+\sum_{\mathrm{jets}} E_T}$. Applying two further QCD reducing cuts left no data events. Despite the modest numbers the rate of expected signal to SM bodes well for investigations on this channel once more data become available in 2011 and onwards including studies of end-point distributions. Higher statistics are required in order to set limits on the cross-section or exclude the two selected mSUGRA points. Two methods to determine the QCD background in the signal region from data was also investigated. Higher statistics and inclusion of additional relevant SM backgrounds in MC are needed to obtain reliable results from this method.

Further work includes further optimisation of this analysis, along with a combined analysis for zero, one and two final states and also an investigation of the tau and light lepton channel. The tau object definition should be optimised to the choice of BDT value yielding the highest separation of real taus to QCD jets for one- and three prong

taus separately. The cut values obtained in 7 should also be optimised with respect to all relevant SM backgrounds, and not only $t\bar{t}$. These factors are however not likely to change the results of this analysis drastically. Performing an inclusive analysis for zero, one and two taus in the final state would greatly improve the discovery potential of the analysis. Final states of one tau and one light lepton is also of interest. This will provide a cleaner channel with higher reconstruction efficiency than for the two tau channel, as the reconstruction efficiency is higher for electrons and muons than for taus. Maybe the most important however, is the search for more tau rich SUSY models and points that has not yet been excluded or investigated by experiment to increase the probability of discovering a possible SUSY model realised in nature. This includes searching mSUGRA points for higher $\tan\beta$ in the co-annihilation region and other SUSY models, for example GMSB. Naturally the analysis should also be performed for larger amounts of data as these become available from the ATLAS experiment. As of writing 2011 data is becoming available, and currently corresponds to about 200 pb^{-1} of integrated luminosity. This also entails a change from release 15 to 16 reprocessed MC with the changes that imply for the analysis. The amount of recorded data is expected to grow rapidly as the luminosity of the LHC is continuously increasing.

Appendix A

Single Tau Analysis

This section is the skeleton of a 1-tau analysis. The same object definitions as in Chapter 7 are used. Figure A.1 shows the number of remaining events and the significance after each cut for SU4, the two high $\tan\beta$ points and $t\bar{t}$. The cuts are as previously defined, and with a BDT > 0.7 required for taus. The selected models has a low

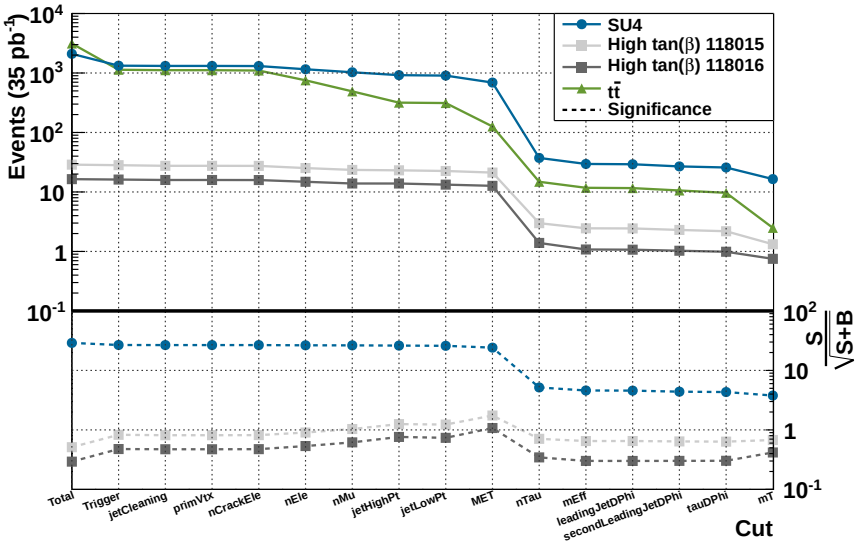

Figure A.1: Significance and remaining events - Remaining events and $\frac{S}{\sqrt{S+B}}$ after each cut scaled to 35pb^{-1} luminosity. Background here is $t\bar{t}$ only.

cross section compared to SU4, and fewer total events are therefor expected. However, a larger percentage of the events in the newer models pass the trigger, jet and missing

energy cut. Also, as expected, the selected models are tau rich and a larger percentage of the events pass the tau cut. The fact that there is a larger percentage of events with a reconstructed tau in model 118015 compared to 118016 is not surprising, taking into account the fact that the soft tau in 118016 often is not reconstructable due to its low momentum. This is clear from $\Delta M(\chi_1^0, \tilde{\tau})$ in table 7.5. About 5 % of the total number of the events of the selected models are left after the baseline cuts, while the corresponding number for SU4 $\sim$ 1%. It is clear that the significance is improving slightly for each of the cuts up until the cut requiring at least one tau. This cut is not made to improve the significance, but is rather enforced by fact that the tau channel is the one being investigated in this analysis. A slight decrease in the significance is also observed for the cuts following the tau cut. This is because only $t\bar{t}$ is considered background in this plot, while these cuts are optimised to remove QCD and W background.

	$t\bar{t}$		**118016**		**118015**	
Cut	**events**	**%**	**events**	**%**	**events**	**%**
Total	3 129 ± 3.1	-	16.42 ± 0.16	-	28.79 ± 0.29	-
Trigger	1 134 ± 1.9	36.2	16.17 ± 0.16	98.5	28.19 ± 0.29	97.9
Jet cleaning	1 114 ± 1.9	98.3	15.90 ± 0.16	98.3	27.51 ± 0.28	97.6
Prim. Vertex	1 114 ± 1.9	100.0	15.90 ± 0.16	100	27.51 ± 0.28	100.0
No Crack e	1 100 ± 1.9	98.7	15.85 ± 0.16	99.7	27.43 ± 0.28	99.7
No e	753.6 ± 1.5	68.5	14.84 ± 0.16	93.6	25.22 ± 0.27	91.9
No e	491.0 ± 1.2	65.1	13.88 ± 0.15	93.5	23.47 ± 0.26	93.1
High p_{T} jet	310.8 ± 0.99	63.3	13.65 ± 0.15	98.4	23.00 ± 0.26	98.0
Low p_{T} jet	304.6 ± 0.98	97.8	13.15 ± 0.15	96.3	22.23 ± 0.25	96.7
$E_{\mathrm{T}}^{\mathrm{miss}}$	122.5 ± 0.62	40.3	12.55 ± 0.14	95.5	20.91 ± 0.25	94.0
One τ	28.86 ± 0.30	23.6	2.303 ± 0.06	18.3	4.779 ± 0.12	22.9
m_{Eff}	23,13 ± 0.27	80.2	1.847 ± 0.06	80.2	3.960 ± 0.11	82.9
$\Delta\phi(\mathrm{jet}_1, E_{\mathrm{T}}^{\mathrm{miss}})$	22.83 ± 0.27	98.7	1.837 ± 0.05	99.5	3.949 ± 0.11	99.7
$\Delta\phi(\mathrm{jet}_2, E_{\mathrm{T}}^{\mathrm{miss}})$	20.49 ± 0.25	89.8	1.748 ± 0.05	95.2	3.709 ± 0.10	93.9
$\Delta\phi(\tau, E_{\mathrm{T}}^{\mathrm{miss}})$	19.34 ± 0.25	94.4	1.684 ± 0.05	96.3	3.568 ± 0.10	96.2
m_T	8.062 ± 0.16	41.7	1.293 ± 0.05	76.8	2.334 ± 0.08	65.4

Table A.1: Cutflow on high $\tan(\beta)$ **models** - Shows the number of events after each cut normalised to 35pb^{-1}, and the percentage of events remaining after a cut with respect to the previous cut.

Loosening the tau BDT to 0.5 to complement the two tau analysis in Chapter 7 gives the cutflow shown in Table A.1. Table A.3 gives $\frac{S}{\sqrt{S+B}}$ optimised cuts on single variables after the 1-tau cutflow in TableA.1. The same variables as for the two tau analysis prove have the best separating powers, namely - $E_{\mathrm{T}}^{\mathrm{miss}}$, H_T, $H_{\mathrm{T,miss}}$ and m_{Eff} as defined in Chapter 7. As before variables can be combined to perform selections in the space spanned by these two variables. Some of the elliptical cuts resulting in the highest sensitivity is shown in Table A.2.

			118015		**118016**	
Variables	**Cut [GeV]**	**Bkg rej. [%]**	**Left [%]**	$\frac{S}{\sqrt{S+B}}$	**Left [%]**	$\frac{S}{\sqrt{S+B}}$
MET, $\sum \mid E_T(jets) \mid$	324, 557	95	84	1.26	87	0.90
MET, M$_T$jets	271, 493	93	85	1.23	90	0.87
HT, HTmiss	568, 320	92	87	1.23	91	0.87
MET, HT	350, 568	93	86	1.26	90	0.89
HTmiss, $\sum \mid E_T(jets) \mid$	320, 493	93	84	1.23	88	0.86

Table A.2: 2D elltiptic cut values for one tau analysis - Optimized for maximal $\frac{S}{\sqrt{S+B}}$

			118015		118016	
Variable	**Cut [GeV]**	**Bkg rej. [%]**	**left [%]**	$\frac{S}{\sqrt{S+B}}$	**left [%]**	$\frac{S}{\sqrt{S+B}}$
HT_{Miss}	293	93	77	1.17	82	0.83
HT	464	92	79	1.16	85	0.82
$\mathrm{P}(\mathrm{jet}_1)$	302	52	89	0.85	90	0.52
$\mathrm{P}(\mathrm{jet}_2)$	138	42	87	0.78	86	0.46
$\Delta R(\mathrm{jet}_1, \mathrm{jet}_2)$	3.2	26	90	0.74	90	0.44
$\Delta\phi(\mathrm{jet}_2, \mathrm{MET})$	1.2	33	89	0.76	87	0.44
$\Delta\phi(\mathrm{jet}_1, \mathrm{jet}_2)$	2.6	35	87	0.75	87	0.45
$E_T(\mathrm{jet}_1)$	245	88	78	1.09	81	0.74
$E_T(\mathrm{jet}_2)$	142	88	63	0.94	62	0.60
$\Sigma\lvert E_T(\mathrm{jets})\rvert$	409	93	73	1.14	75	0.79
$\Sigma\lvert E_T(\mathrm{jets, tau})\rvert$	464	92	79	1.16	85	0.82
$\Sigma\vec{E}_T(\mathrm{jets})$	360	86	79	1.07	81	0.72
$\Sigma\vec{E}_T(\mathrm{jets, tau})$	448	86	78	1.06	82	0.72
mEff	705	91	88	1.24	92	0.87
$m_T(jet_1, MET)$	504	92	80	1.17	82	0.81
$m_T(jet_2, MET)$	322	93	71	1.11	68	0.73
$m_T(jets, tau)$	415	71	73	0.84	75	0.53
$m_T(\tau_1, MET)$	209	57	70	0.72	78	0.47
MET	296	93	78	1.19	84	0.86

Table A.3: 1D cut values for one tau analysis - Optimized for maximal $\frac{S}{\sqrt{S+B}}$ of SUSY models combined.

References

[1] F. Abe et al. **Observation of top quark production in anti-p p collisions**. *Phys. Rev. Lett.*, **74**:2626–2631, 1995. 1

[2] Abdus Salam. **Weak and Electromagnetic Interactions**. *in: Elementary Particle Theory, W. Svartholm,ed., Almquist and Wiksell, Stockholm*, 1968. Originally printed in *Svartholm: Elementary Particle Theory, Proceedings Of The Nobel Symposium Held 1968 At Lerum, Sweden*, Stockholm 1968, 367-377. 3

[3] Steven Weinberg. **A Model of Leptons**. *Phys. Rev. Lett.*, **19**:1264–1266, 1967. 3

[4] S. L. Glashow. **Partial Symmetries of Weak Interactions**. *Nucl. Phys.*, **22**:579–588, 1961. 3

[5] R J N Phillips V D Bargern. *Collider Physics*. Addison-Wesley Publishing Company, Inc, 1997. 3

[6] G Shaw F Mandl. *Quantum Field Theory, Second Edition*. Wiley, 2010. 3, 6

[7] K. Nakamura et al. (Particle Data Group). **2010 Review of Particle Physics**. *J. Phys. G 37, 075021 (2010)*, 2010. 5, 33, 54

[8] Fukuda et al. **Evidence for Oscillation of Atmospheric Neutrinos**. **81**(8):1562–1567, Aug 1998. 6

[9] Makoto Kobayashi and Toshihide Maskawa. **CP Violation in the Renormalizable Theory of Weak Interaction**. *Prog. Theor. Phys.*, **49**:652–657, 1973. 11

[10] Nicola Cabibbo. **Unitary Symmetry and Leptonic Decays**. *Phys. Rev. Lett.*, **10**(12):531–533, Jun 1963. 11

[11] C. S. Lim T. Morii and S. N. Mukherjee. *The Physics of the Standard Model and Beyond*. World Scientific, Geneva, 2004. 13, 15, 17

[12] Gianfranco Bertone, Dan Hooper, and Joseph Silk. **Particle dark matter: Evidence, candidates and constraints**. *Phys. Rept.*, **405**:279–390, 2005. 13

[13] L Bergstroem and A Goobar. *Cosmology and particle astrophysics*. Wiley, 1999. 13

[14] L. V. E. Koopmans and T. Treu. **The Structure and Dynamics of Luminous and Dark Matter in the Early-Type Lens Galaxy of 0047-281 at z=0.485**. *Astrophys. J.*, **583**:606–615, 2003. 13

[15] F. Zwicky. **Remarks on the Redshift from Nebulae**. *Phys. Rev.*, **48**(10):802–806, Nov 1935. 13

[16] R. G. Carlberg, H. K. C. Yee, S. L. Morris, H. Lin, E. Ellingson, D. Patton, M. Sawicki, and C. W. Shepherd. **The M- Dependence of the Apparent Cluster** . *The Astrophysical Journal*, **516**(2):552, 1999. 13

[17] Max Tegmark et al. **Cosmological parameters from SDSS and WMAP**. *Phys. Rev.*, **D69**:103501, 2004. 13

[18] Julio F. Navarro, Carlos S. Frenk, and Simon D. M. White. **The Structure of Cold Dark Matter Halos**. *Astrophys. J.*, **462**:563–575, 1996. 13

[19] David E. Morrissey, Tilman Plehn, and Tim M. P. Tait. **Physics searches at the LHC**. *arXiv:0912.3259 [hep-ph]*, 2009. 13, 14, 77

[20] M. B. Gavela, P. Hernandez, J. Orloff, and O. Pene. **Standard Model CP-violation and Baryon asymmetry**. *Mod. Phys. Lett.*, **A9**:795–810, 1994. 13

[21] Stephen P. Martin. **A Supersymmetry Primer**. 1997. 15, 18, 19, 20, 100, 103

[22] D. I. Kazakov. **Beyond the standard model (in search of supersymmetry)**. 2000. 15

[23] Jonathan L. Feng. **Supersymmetry and cosmology**. 2003. 16, 19

[24] *ATLAS detector and physics performance: Technical Design Report, 2*. Technical Design Report ATLAS. CERN, Geneva, 1999. Electronic version not available. 17, 18, 19, 50

[25] ATLAS Collaboration. *ATLAS computing: Technical Design Report*. Technical Design Report ATLAS. CERN, Geneva, 2005. revised version submitted on 2005-06-20 16:33:46. 17, 29, 30, 31

[26] ATLAS Collaboration. *ATLAS detector and physics performance: Technical Design Report, 1*. Technical Design Report ATLAS 14, CERN/LHCC 99-14. CERN, Geneva, 1999. Electronic version not available. 21, 24

[27] Vittorio Frigo. **Atlas detector.. Detecteur Atlas.** AC Collection. Legacy of AC. Pictures from 1992 to 2002., Mar 1997. 22

[28] G Aad et al. *Expected performance of the ATLAS experiment: detector, trigger and physics*. CERN, Geneva, 2009. 24, 25, 26, 38, 71

[29] Joao Pequenao. **Event Cross Section in a computer generated image of the ATLAS detector.** Mar 2008. 27

[30] EN Dawe, DC O'Neil, and S Protopopescu. **Using Boosted Decision Trees for Hadronic Tau Identification: On behalf of the Tau Performance Group**. Technical Report ATL-COM-PHYS-2010-603, CERN, Geneva, Aug 2010. This is work in progress. 34, 35, 45

[31] The ATLAS collaboration. **Tau Reconstruction and Identication Performance in ATLAS**. Technical Report ATLAS-CONF-2010-086, CERN, Geneva, Oct 2010. 39

[32] R. K. Ellis, I. Hinchliffe, M. Soldate, and J. J. Van Der Bij. **Higgs decay to [pi]+[pi]-: A possible signature of intermediate mass Higgs bosons at high energy hadron colliders**. *Nuclear Physics B*, **297**(2):221 – 243, 1988. 55

[33] A. Elagin, P. Murat, A. Pranko, and A. Safonov. **A New Mass Reconstruction Technique for Resonances Decaying to di-tau**. 2010. 55, 56, 57

[34] M. Janus. Private communication within the ATLAS TauWG, February 2011. 69

[35] **Data-Quality Requirements and Event Cleaning for Jets and Missing Transverse Energy Reconstruction with the ATLAS Detector in Proton-Proton Collisions at a Center-of-Mass Energy of sqrts=7 TeV**. Technical Report ATLAS-CONF-2010-038, CERN, Geneva, Jul 2010. 70

[36] ATLAS Collaboration. **Search for squarks and gluinos using final states with jets and missing transverse momentum with the ATLAS detector in sqrt(s) = 7 TeV proton-proton collisions: Version 1.0**. Technical Report ATL-COM-PHYS-2010-1046, CERN, Geneva, Dec 2010. Support note of the jets+MET SUSY paper. 70, 115

[37] `https://twiki.cern.ch/twiki/bin/view/AtlasProtected/ElectronReconstruction`, 2011. Internal TWIKI. 71

[38] **Electron and photon reconstruction and identification in ATLAS: expected performance at high energy and results at 900 GeV**. Technical Report ATLAS-CONF-2010-005, CERN, Geneva, Jun 2010. 71

[39] **A measurement of the ATLAS muon reconstruction and trigger efficiency using J/psi decays**. Technical Report ATLAS-CONF-2011-021, CERN, Geneva, Mar 2011. 72

[40] **Jet energy scale and its systematic uncertainty for jets produced in proton-proton collisions at sqrt(s) = 7 TeV and measured with the ATLAS detector**. Technical Report ATLAS-CONF-2010-056, CERN, Geneva, Jul 2010. 72, 115

[41] Matteo Cacciari, Gavin P. Salam, and Gregory Soyez. **The anti- k t jet clustering algorithm**. *Journal of High Energy Physics*, **2008**(04):063, 2008. 72

[42] S. Schael et al. **Search for neutral MSSM Higgs bosons at LEP**. *Eur. Phys. J.*, **C47**:547–587, 2006. 77

[43] `https://twiki.cern.ch/twiki/bin/view/AtlasProtected/SusyObjectDefinitionsr15`. Internal TWIKI, 2011. 82

[44] G. Cowen. *Statistical Data Analysis*. Oxford University Press, Great Clarendon Street, Oxford OX2 6DP, 1998. 86, 87

[45] R. A. Fisher. **The Use of Multiple Measurements in Taxonomic Problems**. *Annals of Eugenics*, **7**(7):179–188, 1936. 86

[46] Michael Graesser and Jessie Shelton. **Probing supersymmetry with third-generation cascade decays**. *Journal of High Energy Physics*, **2009**(06):039, 2009. 101

[47] **Updated Luminosity Determination in pp Collisions at root(s)=7 TeV using the ATLAS Detector**. Technical Report ATLAS-CONF-2011-011, CERN, Geneva, Mar 2011. 105, 115

[48] G. Akimenko et al. **Search for supersymmetry with jets, missing transverse momentum and taus at sqrt(s) = 7 TeV (supporting INT note)**. Unplublished, April 2011. 107, 109, 115

[49] `https://twiki.cern.ch/twiki/bin/view/AtlasPublic/LuminosityPublicResults`, May 2011. 112

[50] **Jet energy resolution and selection efficiency relative to track jets from in-situ techniques with the ATLAS Detector Using Proton-Proton Collisions at a Center of Mass Energy** *sqrts* **= 7 TeV**. Technical Report ATLAS-CONF-2010-054, CERN, Geneva, Jul 2010. 115